UNIVERSITÀ DEGLI STUDI
DI MODENA E REGGIO EMILIA

Dipartimento di Ingegneria "Enzo Ferrari"

Dottorato di ricerca in Ingegneria Industriale e del Territorio "Enzo Ferrari"

Ciclo XXXII

Fatigue characterization of AlSi7Mg, Ti6Al4V and X3NiCoMoTi alloys produced by Laser Powder Bed Fusion

Candidato: Silvio Defanti

Relatore (Tutor): Prof. Elena Bassoli

Correlatore (Co-Tutor): Dr. Antonella Sola

Coordinatore del Corso di Dottorato: Prof. Alberto Muscio

Abstract

In the last years, Laser Powder Bed Fusion (L-PBF) has become the main technology to produce metal parts by Additive Manufacturing (AM). This manufacturing technique comprises the advantages of AM and the high performance offered by metal alloys in order to produce mechanical components ready for the final application.

Occasionally, due to the layer-wise process, some defects can be produced inside the parts, leading to a critical situation where mechanical properties are at first well above the requirements for static loads, but rapidly decay under fatigue conditions. This concern leads the researchers to investigate the actual mechanical properties of parts, as compared to those of traditionally manufactured components, and to optimize the whole process in order to limit defects and increase the reliability of the process.

While extensive static tests have confirmed the high mechanical properties of the main metal alloys produced by AM, the fatigue behavior of additive metal parts still needs to be deeply investigated.

In this study, the effects of numerous parameters on the fatigue and tensile properties of 3 metal alloys were analyzed, in view of 3 final applications, listed as follows.

- Automotive field: Aluminum alloy AlSi7Mg was studied for the final production of a topologically optimized frame part of a sports car.
  In particular, the interest was focused on the effect of:
    - Heat treatment: no heat treatment vs. T6 treatment vs. the heating cycle required for painting the body-in-white frame;
    - Surface finish: as-built vs. polished;
    - Orientation on the building platform.
- Medical field: Titanium alloy Ti6Al4V was investigated for the production of femoral stems with improved osseointegration.
  The study on this material was focused on the effect of:
    - Powder contamination;
    - Different parameters/powder sets;
    - Surface finish: as-built vs. polished;
    - Orientation on the building platform.
- Mold manufacturing field: the Maraging steel alloy X3NiCoMoTi was studied for the application in a mold insert with internal cooling channels.
  The main concern related to this application led to the study of the effect of:
    - Holes in the material, acting as stress concentrators;
    - Surface finish of the holes;
    - Different parameters/powder sets.

This work aims at providing better understanding of the critical variables of the manufacturing process and the post-processing operations.

This study was accomplished within the European Project DREAM (Driving Up Reliability of Additive Manufacturing)

Keywords: Additive Manufacturing, Fatigue, AlSi7Mg, Ti6Al4V, X3NiCoMoTi

Contents

Acknowledgments

This work has been accomplished within the European project DREAM (Driving up Reliability and Efficiency of Additive Manufacturing), Call H2020-FOF-2016, http://www.dream-euproject.eu/.

The project includes the following partners:

Participant n°	Participant organization name	Short Name (Type)	Country
1 (Coordinator)	Consorzio Interuniversitario Nazionale per la Scienza e Tecnologia dei Materiali	INSTM (UNI)	Italy
2	EOS Electro-Optical Systems Gmbh	EOS (LE)	Germany
3	Transilvania University of Brasov	UTBv (UNI)	Romania
4	BeWarrant S.L.	BEWG (SME)	Belgium
5	Mind Four D S.R.L.	MIND4D (SME)	Romania
6	Poly-Shape S.A.S.	POLYS (SME)	France
7	Adler Ortho France S.A.R.L.	ADLERFR (SME)	France
8	R.B. S.R.L.	RB (SME)	Italy
9	Ferrari S.p.A.	FERRARI (LE)	Italy

1. Introduction

1.1 Additive Manufacturing fundamentals and applications

Additive manufacturing (AM) was born for rapid prototyping purposes in the 80s [1]. It was used in industries as a process to rapidly create the representation of a component before its final release. Prototyping operations are useful to check the coupling between different parts of an assembly or to test the ergonomics of a part providing feedback during its development.

According to the degree of representation of the prototype, as compared to the final object, there can be 3 main types of prototypes [2]:

- Visual prototype: reproduces the size and the appearance, but not the functionality of a part.
- Functional prototype: captures both the function and the appearance of the intended design, though it may be created with a different technique and even on a different scale from the final design.
- Technological prototype: a functional prototype is built with the same manufacturing technology and the same material of the final part.

The first AM machines were able to produce only visual prototypes due to the low mechanical properties of the materials used. Thanks to the improvement of machines hardware and to the development of new techniques, a significant increase in the quality and performance of the parts occurred, allowing the users to produce functional prototypes, with mechanical characteristics comparable to those of the final part. Finally, with the progressive enhancement of the available materials and the introduction of new metal alloys, the technology switched officially from a technique for prototype production to a technology suitable to produce final functional parts, hence called “Additive Manufacturing (AM)”, as stated by ASTM F2792 [3].
Basically, AM consists in the production of a part by adding material layer upon layer. The basic workflow (summed up in Figure 1) is nearly the same for every AM technique and every part [4]:

1) The starting point is always a 3D CAD model, the digital representation of the component.
2) The CAD file is converted into an STL, a standard file format for 3D printing where the mathematical functions representing the object are approximated by triangular facets. In this step it is critical to set the appropriate approximation level to avoid tessellation effect on the surfaces of the part.
3) The STL is loaded in the pre-processing software where the part is oriented inside the machine volume and support structures are generated.
4) The assembly of part and supports is then post-processed inside a software that slices the part in layers and generates a toolpath or, more generally, the machine instructions to build the part.
5) The instructions file is loaded in the machine and after preliminary operations, the building job can start.
6) When the building job is complete, the part is removed from the building platform of the machine. At this step, the part could be ready for the final application but often, some post-processing operations are necessary.
7) Post processing: if the part has supports, they must be removed, then, according to the specific AM technique, other processes can be performed such as heat treatments, surface finishing or machining of some surfaces as well.

The same part, if produced with other technologies, would require:

- In case of casting: after acquiring the cad design, it is necessary to design and produce molds (cavities, channels, sprues etc.) and casting patterns and a simulation of the casting process could be necessary as well [5]. These operations can require some weeks, according to the complexity and the dimensions of the part.

- In case of machining: firstly, the stock material is determined, then the generation of toolpaths in CAM software is performed; this operation can be very slow and requires high competence [6]. Then, during the machining, the part could need complex repositioning operations. Even for machining, if the complexity of the part increases, the time to produce the part and the final cost increase [7].

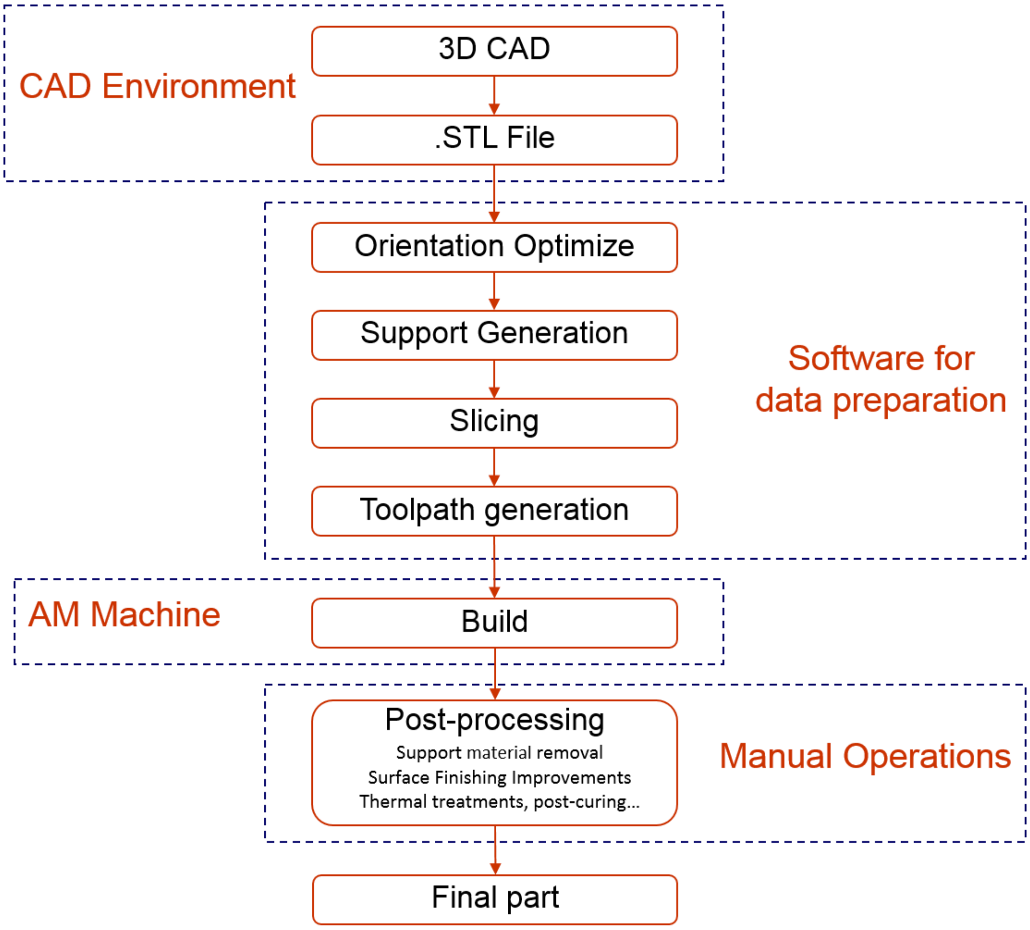

Figure 1: Additive manufacturing workflow

Unlike the described technologies, the process workflow of AM is almost straightforward (Figure 1) and generally, it requires few competences to be accomplished (depending on the AM technology), regardless of the complexity of the part.

In other words, complexity is free and AM allows to produce parts with geometrical features that cannot be produced with other existing technologies.

In fact, when designing a component, designers always have to think of how the part would be produced, introducing manufacturing constraints and consequently limiting the possibilities in term of geometric freedom. AM, on the other hand, allows to produce parts with a very complex shape, internal channels, overhangs and lattice structures. Actually, this possibility must be exploited to limit material usage and place it only where it is really needed.

Topology optimized parts can now be produced without (almost) any manufacturing constraint [8]. These components are designed taking as input the design space of the part, the constraints such as gripping and connection points and the load that the part would withstand during its usage. Then, the software distributes the material only where it is strictly needed (Figure 2 [9]). The resulting part is generally complicated in term of geometry and often it is not feasible with traditional manufacturing technologies. In fact, manufacturing constraints can be added during the optimization process, to take into account the manufacturing technology but by choosing AM, all the potentiality of the topological optimization can be exploited.

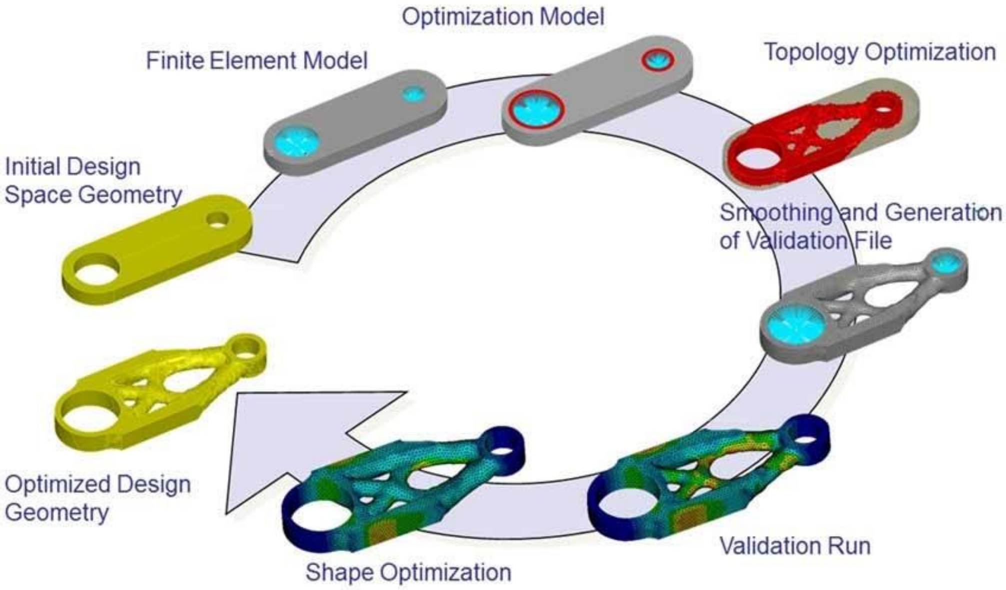

Figure 2: Topological optimization typical workflow. [9]

Further, the geometrical freedom offered by AM can be exploited to build parts that otherwise, with traditional technologies, would be fabricated in many components and then assembled. With AM all the components can be built together. A remarkable example is the LEAP Engine injection nozzle (Figure 3 [10]), originally composed of 20 components welded together and now built by AM in one single part [11].

Figure 3: LEAP Engine injection nozzle built by AM. [10]

However, it must be noted that AM is a manufacturing technique that produces anisotropic parts [12]. In fact, due to the layer-wise building process, the bonding between layers can be weak, hence the mechanical properties measured along the building direction will be poorer than those measured on a plane parallel to the building platform of the machine. This statement is generally true but not for all the AM technologies so it will be discussed further in this work. However, designers should take into account this aspect when verifying the structural strength of a part.

A substantial advantage of AM is the extremely short time-to-market [13]. In fact, in a conventional industrial context, the time interval from the reception of the CAD file to the obtainment of the final part, is typically of some days. Traditional manufacturing processes require careful and detailed analysis of the part geometry to determine the fabrication order of the single features and to define the tools and processes that must be

used and the additional fixtures. The time interval required to produce the part can reach months. With AM, this time can be reduced down to some days.
However, while in conventional manufacturing, after the activities mentioned above, the productivity can be up to millions parts per year, with AM only small batches can be produced, because of the low productivity of additive machines, which is typically around 70 g/h, instead of 100 kg/h as often happens with conventional manufacturing technologies [14]. This characteristic restricts the applications in which AM can be competitive to [1,15]:

1) Prototyping: the first and already discussed application. AM is still the major technique used for prototyping. Design and engineering teams can provide multiple design iterations that can be printed, reviewed and adjusted with zero downtime.
2) Tooling: AM enables the fast production of the jigs, fixtures and tooling required for manufacturing other parts. Further, AM technologies are suitable to produce complex casting patterns and also small molds for metal casting.
3) Production of spare parts: this application allows to reduce warehousing and repair times.
4) Customized parts production: since no molds or tools are needed, producing customized parts is relatively easy. Only the CAD file must be modified, with almost no cost increase.
5) Small volume manufacturing: small batches can be produced cost-efficiently, significantly reducing the investment in tooling.
6) Complex parts: as discussed, the best application is producing geometrically complex parts that cannot be produced with other technologies.
7) On-site and on-demand manufacturing: eliminate storage and transportation costs.

The number and type of industries benefitting of AM for all the above reasons and applications are increasing every day. The following section briefly describes the main industrial applications of AM to give a glimpse of the current wide scenery.

Aerospace

As deeply investigated in the book by Froes and Boyer [16], AM is extensively exploited in aerospace industry. The reason is the possibility to build complex and lightweight parts, with lower buy-to-flight ratios in comparison to other subtractive manufacturing techniques. A reduction of one kilogram on an aircraft equates to saving 1300 $ in fuel per year [17].

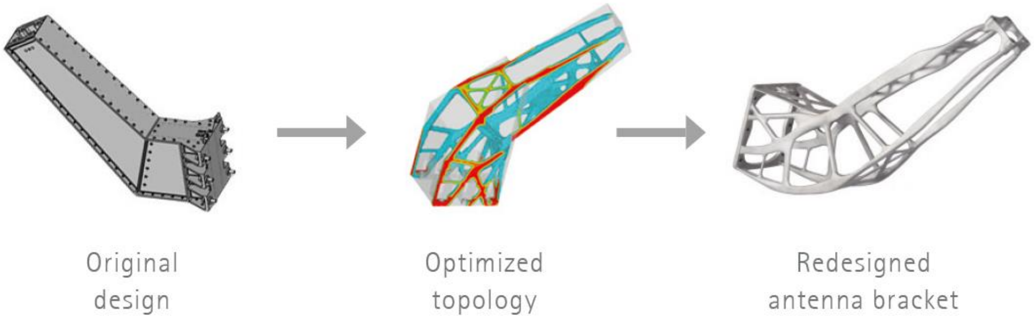

Figure 4: Design optimization of the satellite antenna bracket by RUAG. [19]

Examples of parts effectively applied in real applications are:

- Turbine blades, both for power-generation [18] and aircraft propulsion;
- LEAP engines fuel nozzles, as already discussed above;

- Satellite antenna brackets, as proposed in a case study of RUAG Group with the aim of developing a lightweight and robust antenna for Sentinel satellites (Figure 4) [19];
- Plastic parts such as airflow ducting systems, dashboard interfaces, cabin brackets and others.
- Other singular case studies have been successfully produced such as a cable routing mount for a camera, injection head for rocket engines, engine combustion chambers etc. [16]

New applications are emerging every day.

Automotive

AM is effectively adopted in the automotive industry, especially in the motorsport sector. In fact, unlike passenger cars, vehicles for motorsports usually exploit light-weight alloys (e.g. aluminum and titanium) and have highly complex structures and low production volumes.

Formula 1 race car design teams are benefitting from the design freedom and rapid prototyping/testing capabilities of AM to speed up fabrication cycles to gain competitiveness. In these cases, cost is a secondary consideration while weight reduction and design freedom are the first concern. These sorts of critical application components, made of plastics, metals, or composites are not subject to the same testing and certification constraints as commercial components, thus providing an effective test bed for these components [20].

As for aerospace sector, several case studies have been realized and effectively used as final applications, but only few of them are known because of confidentiality. For example:

- Steering knuckle for a formula SAE car [21] (Figure 5-A) and other race car [22]
- Bugatti Chiron brake calipers [23] (Figure 5-B)
- Tooling: in this case AM provided tools for the stamping process with excellent performance with a significant decrease on time-to-tooling [24]
- Various topologically optimized brackets [25]
- Optimized pistons.

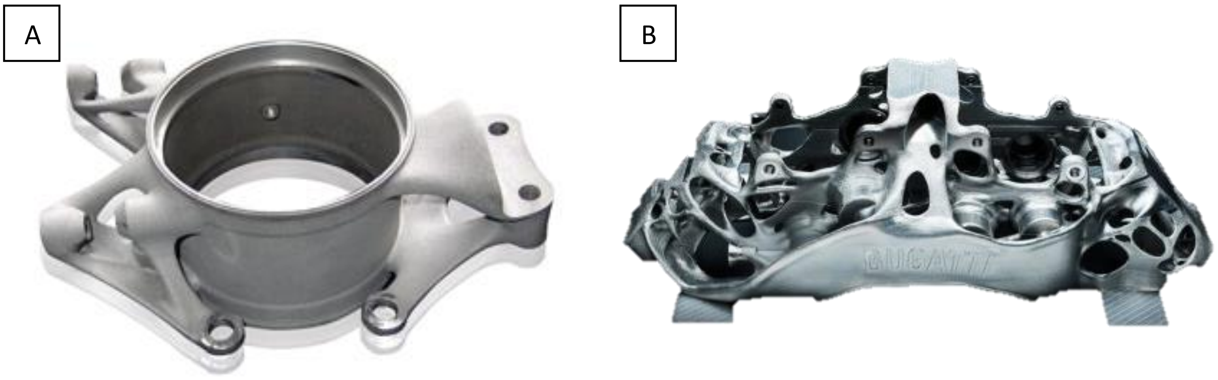

Figure 5: (A) Formula SAE steering knuckle [21] and (B) Bugatti Chiron brake caliper [23].

Bio-Medical

The possibility of creating customized parts directly from 3D scans is the main driving force for the use of AM in medical field. In fact, with Computer Tomography (CT) and Magnetic Resonance Imaging (MRI), the medical data of the patient can be acquired and then the collected images are converted into a CAD model. Subsequently, the simulations and editing operations are performed on the CAD geometry and, at the end, the part can be produced by AM [26]. The entire process is shown in Figure 6 [26].

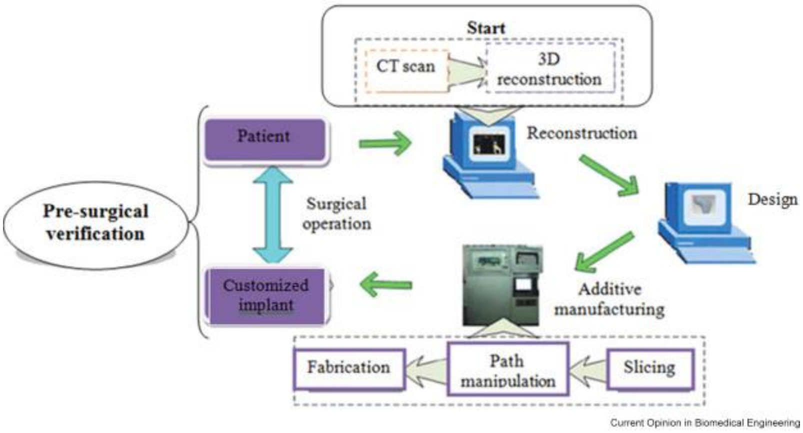

Figure 6: Schematic of the production of customized biomedical parts by AM. [26]

At first, AM models were mainly used for diagnostic purposes and as aid in the planning and performing of surgery. Then, with the enhancement of the CT scan and AM resolution, models have become more precise, allowing for the fabrication of close-fitting prosthetic devices.

Several cases of limbs replacement for amputee people are documented [27] (Example in Figure 7A [28]). These components have both functional and aesthetic purposes and can be integrated with moving devices to replace an entire joint.

Foot orthoses and ankle-foot orthoses have been successfully produced and used by patients [29].

Devices for internal implant are under research and development. Several parts have been produced but more studies should be carried out to assess mechanical performance and integration with the organism [26].

Knee and hip implant (Figure 7B [30]) components with porous structures have been fabricated in monolithic forms. Porous areas exhibit considerable potential because in addition to promoting bone cell ingrowth for implant stabilization, porosity or cellular density variations can allow for stiffness selections to better match the modulus of different bone types [31].

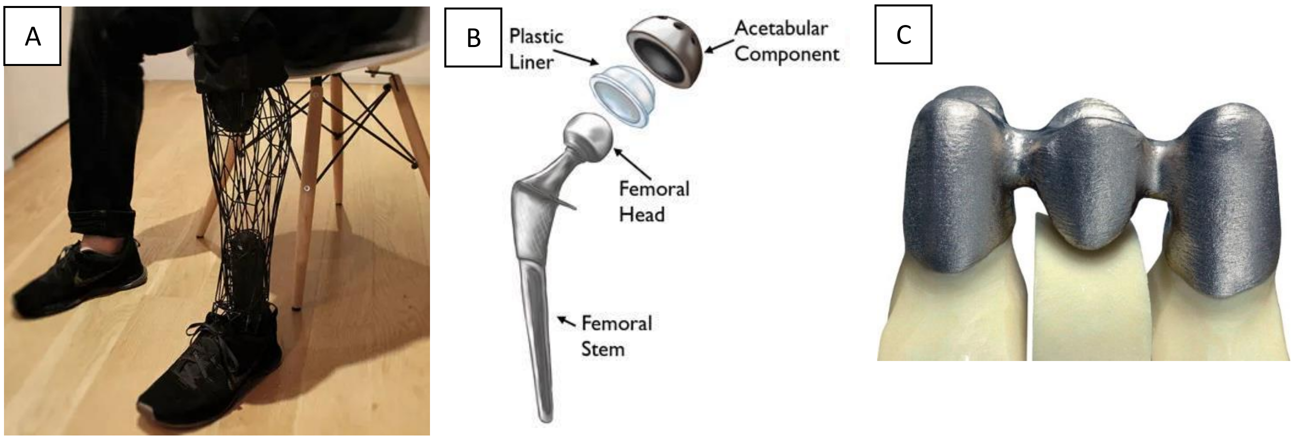

Figure 7: Some AM applications in medical: (A) leg prosthesis [28], (B) femoral stems [30], (C) dental bridge [32].

AM has been successfully applied also in orthodontics: using metal AM machines, it is possible to print crowns and bridges (Figure 7C [32]) from cobalt-chrome and other alloys. In-house production of 3D-printed braces reduces the number of visits required during a lengthy period that often spans 18 to 24 months or more [33].

Finally, AM can be applied for tissue-engineering applications to produce scaffolds or to directly print tissues [34].

Industrial applications: molds and tooling

With AM it is possible to build entire molds for metal casting, including complex casting patterns [35] (Figure 8A).

In the mold manufacturing field, mold inserts can be produced with complex conformal cooling channels (Figure 8B [36]) to speed the molding process and improve part quality. Thanks to AM, inserts can be built directly onto pre-existing parts. The cooling time during the injection molding process can be reduced up to 40%, according to the geometry of the insert. [37]
AM metal processing can be also used to repair or modify existing tools to extend the life or increase the performance of existing parts.

AM can be used in the investment casting process to create an evaporative pattern as a master part as exemplified in Figure 8C [38].

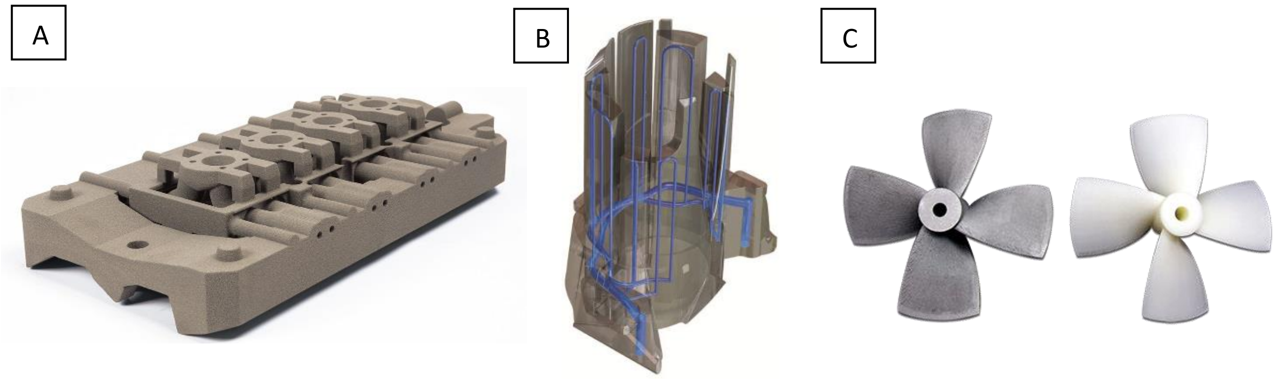

Figure 8: Some AM applications in mold and tooling: (A) casting pattern [35], (B) molt insert with conformal cooling channels [36], (C) evaporative pattern [38].

Several other applications exist, like in art field and for customized objects. These applications have a common point: the objects cannot be produced with other techniques apart from AM or sometimes the geometry has been specifically designed for AM.

Quite often, parts that are already produced effectively with traditional technologies are not feasible by AM because, typically, time and costs would be much greater, unless the geometry is conveniently redesigned [39].

1.2 Additive Manufacturing technologies

Numerous techniques are available nowadays to additively produce a part. Every technique is characterized by the form of the raw material and by the transformation process that it follows to be arranged into layers [40]. As a consequence, some important aspects are shared in the same AM technology class, such as:

- Materials that can be processed;
- Accuracy: generally expressed as the size of the minimum printable detail;
- Productivity: expressed in printed volume per time;
- Maximum printable volume.

Several additive technologies are available, based on different principles. According to the standard ASTM F2792 [3] they are:

- Vat Photopolymerization: AM process in which liquid photopolymer in a vat is selectively cured by light-activated polymerization.
- Material Extrusion: AM process in which material is selectively dispensed through a nozzle or orifice.
- Material Jetting: AM process in which droplets of build material are selectively deposited.
- Binder Jetting: AM process in which a liquid bonding agent is selectively deposited to join powder materials.
- Powder Bed Fusion: AM process in which thermal energy selectively fuses regions of a powder bed
- Directed Energy Deposition: AM process in which focused thermal energy is used to fuse materials by melting as they are being deposited.
- Sheet Lamination: AM process in which sheets of material are bonded to form an object.

Some techniques are specific for a material class, whereas other techniques can be used for different materials. For example, material jetting makes use of a thermoset polymer that goes through micrometric nozzles and is then consolidated by a UV light. This technique is exclusive for thermoset polymers. On the other hand, powder bed fusion techniques can be used with polymeric or metallic powder (the basic principle does not change).

Table 1, which is extracted from the work by Guo and Leu [41], summarizes the main AM technologies, the typical materials used and the main applications.

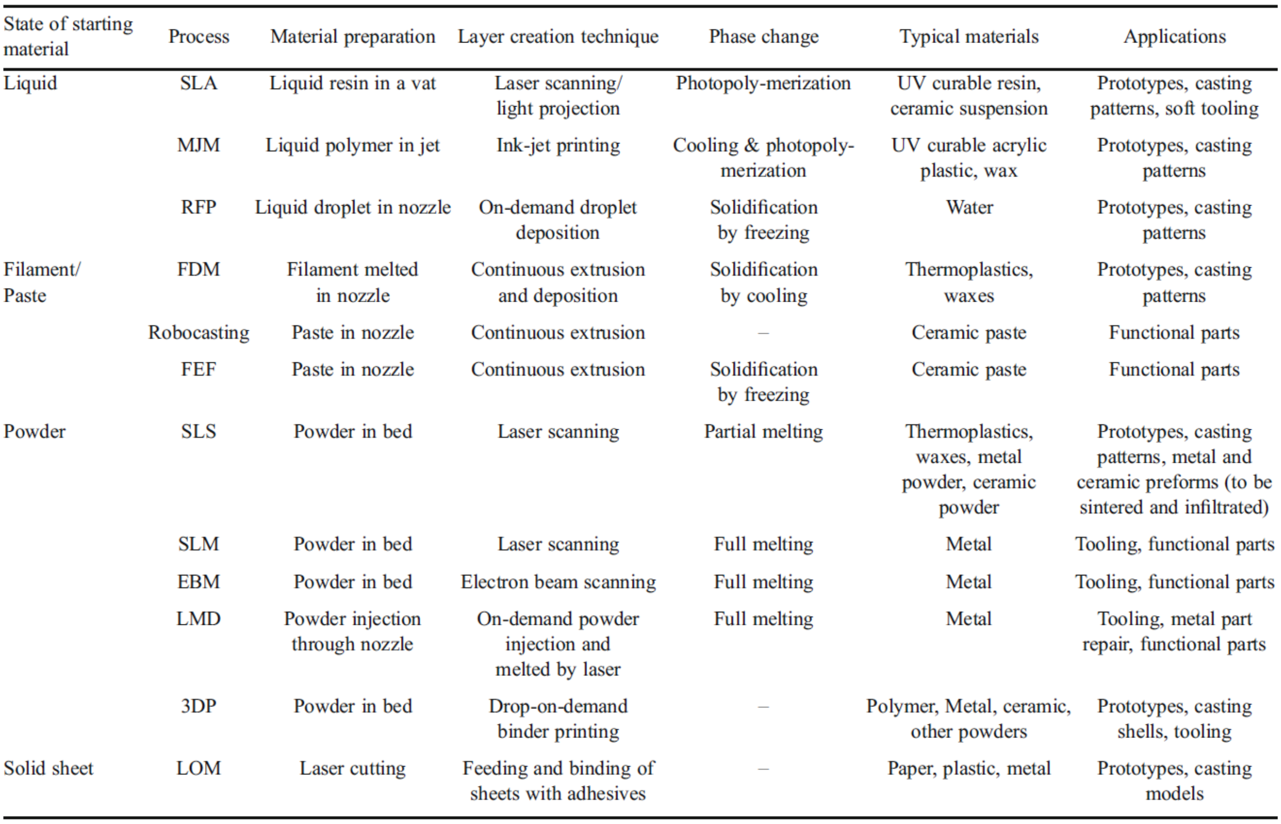

State of starting material	Process	Material preparation	Layer creation technique	Phase change	Typical materials	Applications
Liquid	SLA	Liquid resin in a vat	Laser scanning/ light projection	Photopoly-merization	UV curable resin, ceramic suspension	Prototypes, casting patterns, soft tooling
	MJM	Liquid polymer in jet	Ink-jet printing	Cooling & photopoly-merization	UV curable acrylic plastic, wax	Prototypes, casting patterns
	RFP	Liquid droplet in nozzle	On-demand droplet deposition	Solidification by freezing	Water	Prototypes, casting patterns
Filament/ Paste	FDM	Filament melted in nozzle	Continuous extrusion and deposition	Solidification by cooling	Thermoplastics, waxes	Prototypes, casting patterns
	Robocasting	Paste in nozzle	Continuous extrusion	–	Ceramic paste	Functional parts
	FEF	Paste in nozzle	Continuous extrusion	Solidification by freezing	Ceramic paste	Functional parts
Powder	SLS	Powder in bed	Laser scanning	Partial melting	Thermoplastics, waxes, metal powder, ceramic powder	Prototypes, casting patterns, metal and ceramic preforms (to be sintered and infiltrated)
	SLM	Powder in bed	Laser scanning	Full melting	Metal	Tooling, functional parts
	EBM	Powder in bed	Electron beam scanning	Full melting	Metal	Tooling, functional parts
	LMD	Powder injection through nozzle	On-demand powder injection and melted by laser	Full melting	Metal	Tooling, metal part repair, functional parts
	3DP	Powder in bed	Drop-on-demand binder printing	–	Polymer, Metal, ceramic, other powders	Prototypes, casting shells, tooling
Solid sheet	LOM	Laser cutting	Feeding and binding of sheets with adhesives	–	Paper, plastic, metal	Prototypes, casting models

Table 1: List of the main additive manufacturing techniques classified by the state of the starting material. Typical materials and applications are associated to every technique. [41]

This thesis will be focused exclusively on the powder bed fusion techniques for metals, in particular the one using a laser as the thermal energy source, hence called L-PBF (Laser Powder Bed Fusion).

1.3 The Laser Powder Bed Fusion process

This additive process is the most popular one for the production of metal parts, because of its reliability, its relatively affordable costs and its good productivity [42].

Basically, the process consists in the selective melting of a powder bed by means of a laser beam focused on the powder bed. So, the metal powder actually melts, unlike the process of Selective Laser Sintering (SLS), where the powder is only sintered by creating necks between the particles.
Then, the laser beam fuses a layer following a scan path of overlapping weld beads. After the melting process, another powder layer is spread onto the first one and the laser selectively melts the powder of this new layer. The process goes on until the part is completed.
The building volume is enclosed in a sealed chamber, filled with a continuous flow of inert gas, to avoid metal oxidation during the melting process. A process scheme is shown in Figure 9 [43].

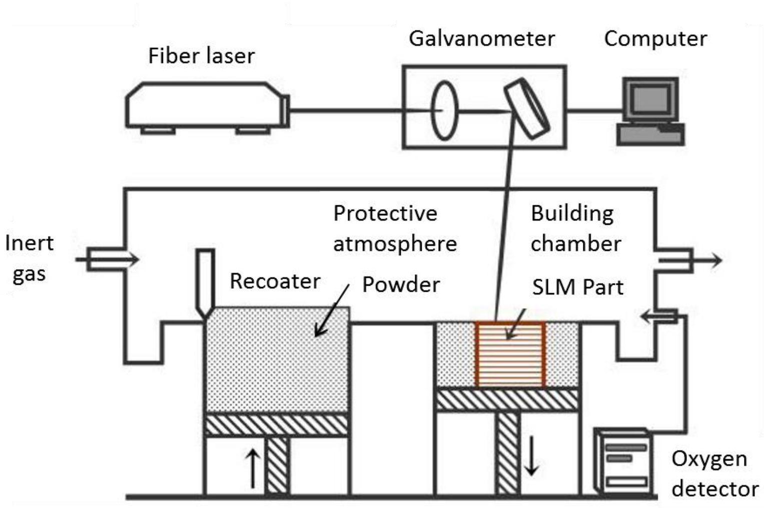

Figure 9: L-PBF basic process scheme. [43]

In a detailed way, the process goes through these steps [44]:

1) Machine setup: a new build plate is mounted on the base of the Z-axis movement system and the parallelism with the base is checked.
2) The building chamber is closed and the inert gas is pumped inside it. The inert gas is essential to protect the metal from oxidation. Then the build plate is heated to a temperature up to 300°C to reduce the cooling rate of the molten metal, thus limiting distortions of the part.
3) The first powder layer is spread, to verify the parallelism between the recoater blade and the build plate and to check the quality of the powder layer. When the oxygen content is lower than 0.2%, the inert gas inlet is closed and the recirculating pump is activated. Now, the chamber is isolated from the environment and the inert gas is continuously recirculated.
4) At this time the process can begin. The build plate is lowered by a quantity equal to the layer thickness and a powder layer is spread. In this initial phase it is important to ensure that the part strongly attaches to the platform, so the first 1-3 layers are consolidated with a higher energy density as compared to the energy density used to consolidate the part.
5) During the building process, several monitoring devices are used such as cameras for imaging and thermal analysis. The control data are continuously analyzed and the building job can be stopped if critical errors are detected. The process goes on until the part is completed.
6) At the end of the building process, the build plate is raised and all the powder is collected on the chamber base. Depending on the machine, there could be inspection gloves and vacuum cleaner

integrated in the machine to recover the powder that was not consolidated during the building process.

7) After the powder removal, the chamber can be opened and the build plate can be removed and extracted from the machine.
8) The part is cut away and supports are removed, then other post-processing operations can be applied.

At present, almost 100% fully dense parts can be fabricated, using several metal alloys [45][46]:

- Aluminum alloys: AlSi10Mg, AlSi7Mg, AlSi9Cu, Scalmalloy
- Titanium alloys: Ti6Al4V, Ti6Al4V ELI, CP Ti, TA15
- Nickel alloys: IN626, IN718, IN939, HX
- Stainless Steels: 316L, 15-5PH, 17-4PH, CX
- Maraging Steel alloys: 1.2709 (X300NiCoMoTi)
- Cobalt alloys: CoCr28Mo6
- Copper alloys: CuSn10, CuNi2SiCr
- Tungsten

As already mentioned, the part is made up of layers of melted metallic powder. Every layer is consolidated by the laser beam that fuses a portion of material under the focused spot. With the movement of the laser beam on the powder bed, selected portions of the layer are consolidated, according to a toolpath previously calculated.

The phenomena occurring during the building process are numerous and reciprocally correlated. Before analyzing the melting process and how multiple “weld lines” can build a part, the two main components are deeply analyzed to better understand their interactions.

The first and main component that will be discussed is the laser source. A brief explanation will be provided, starting from the laser radiation generation, its characteristics and the interaction with the powder particles.

1.4 Laser Source

1.4.1 Physical Principles

(Main references: [47,48])

The word LASER is an acronym for Light Amplification by Stimulated Emission of Radiation. The name just gives an idea of the basic principle of the beam generation.

To understand it better, the radiation-matter interaction modes should be considered firstly.

The radiation-matter interactions are described by the Plank equation (Eq. 1):

$$E_2 - E_1 = h\nu \tag{1}$$

Basically, we can consider a quantum system such as an atom or a molecule that can exists in two different energy levels E_1 and E_2, with $E_2 > E_1$.

When a radiation with a known wavelength hits the system (for simplicity purpose we will consider an atom with one electron), it can interact in 3 different ways (Figure 10 [47]):

1) **Spontaneous absorption**: a photon with a particular frequency satisfying the Plank equation would be absorbed by an electron at the ground state (E_1), that transits to the excited state (E_2).
2) **Spontaneous emission**: the electron in the excited state with the energy E_2 may spontaneously decay to the ground state (E_1) releasing the difference in energy between the two states as a photon.

3) **Stimulated emission**: if the excited-state atom is perturbed by the electric field of a photon with frequency ν, it may release a second photon of the same frequency, in phase with the first photon. The atom will again decay into the ground state. The emitted photon is identical to the stimulating photon with the same frequency, polarization, and direction of propagation.

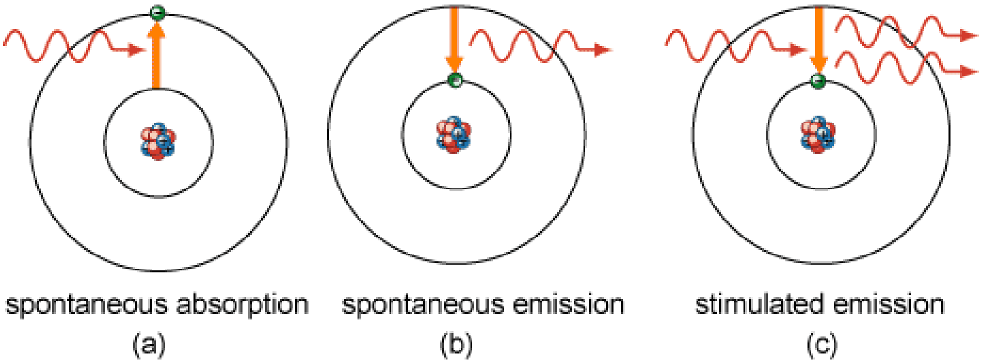

Figure 10: Radiation/matter main interaction modes. [47]

All the three processes occur simultaneously within the laser medium, however, in thermal equilibrium, the stimulated emission is not significant and most of the electrons are in the ground state.

To obtain light emission it is necessary a population inversion, i.e. when the higher energy state has a greater population than the lower energy state. However, this process cannot be achieved by only two states because the electrons will eventually reach equilibrium with the de-exciting processes of spontaneous and stimulated emission.

A three energy levels system ($E_1<E_2<E_3$) is adopted instead. The process goes through some steps:

1) When external energy is provided (**pumping**), the electrons are excited to level 3
2) Excited electrons quickly decay to level 2 with a radiationless transition (R phase)
3) Electrons on level 2 decay by spontaneous emission to level 1 (L phase)

If the life time of the spontaneous emission ($E_2 \rightarrow E_1$) is much longer than that of the radiationless transition ($E_3 \rightarrow E_2$), the population of the E_3 will be essentially zero and a population of excited state atoms will accumulate in level 2. When level 2 hosts over half of the total electrons, a population inversion is achieved. Because half of the electrons must be excited, the pump system needs to be very strong. This makes three-level lasers rather inefficient. Most of the present lasers are 4-level lasers.

Although with a population inversion it is possible to amplify a signal via stimulated emission, the overall single-pass gain is quite small, and most of the excited atoms in the population emit spontaneously and do not contribute to the overall output. To amplify the effect, a resonator is applied in the system.

An optical resonator is a cavity containing the laser medium. It is usually composed by two flat or concave mirrors, one on either end, that reflect photons back and forth so that stimulated emission continues to build up more and more laser light.
One of the two mirrors is made as close to 100% reflective as possible, while the other one is typically made only 95 - 99% reflective so that the rest of the light is transmitted by this mirror and leaks out to make up the actual laser beam outside the laser device.

The resonator type and the gain medium mainly determine the laser output. The output of a laser beam actually consists of a number of closely spaced spectral lines of different frequencies (Figure 11 [49]). The discrete spectral components are termed as laser modes and the coverage range is the line width of the atomic transition responsible for the laser output. For a Gaussian profile, it can be expressed as the FWHM of the wavelength distribution.

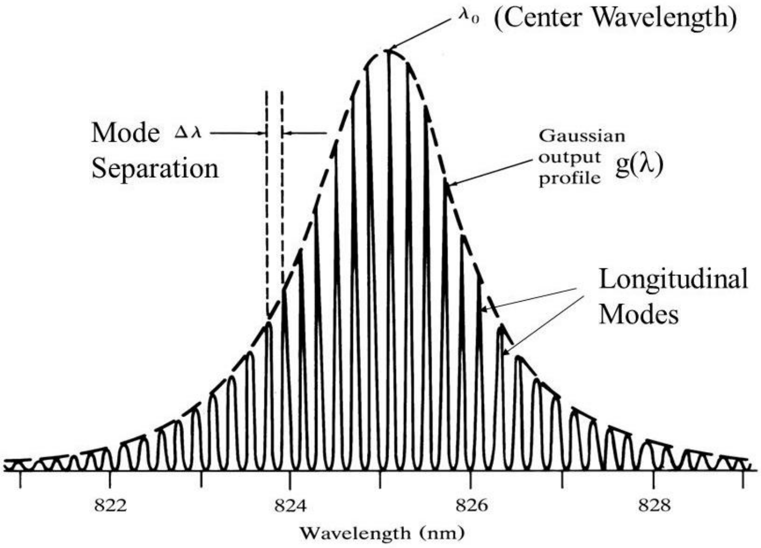

Figure 11: Multimode laser output spectrum. [49]

Laser modes can be axial (or longitudinal) caused by the number of standing waves parallel to the propagation axis inside the cavity. Laser modes can also be transverse (TEM): waves traveling out of the axis that are not able to repeat their own path. These modes can be practically seen in the form of pattern when the laser beam falls on any surface. These modes are assigned by the term TEM_{pq} where p and q are the number of minima in the horizontal and vertical directions (Figure 12-A [50]).

The TEM_{00} is known as uniphase mode and has no minima in the beam spot. It is also called Gaussian beam due to its intensity distribution and it is the typical transverse mode for industrial laser applications (Figure 12-B [51]).

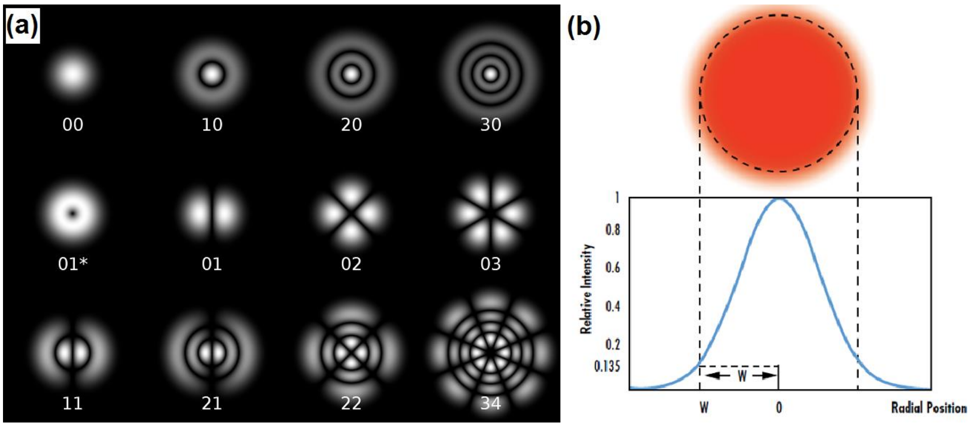

Figure 12: (A) Cylindrical transverse mode patterns [50], (B) Gaussian beam (TEM_{00}) intensity distribution [51].

To sum up, 3 main components are necessary to produce a laser radiation:

1) Gain medium: the lasing element
2) Resonator
3) Pump source

The basic principle of operation is illustrated in Figure 13 [48]:

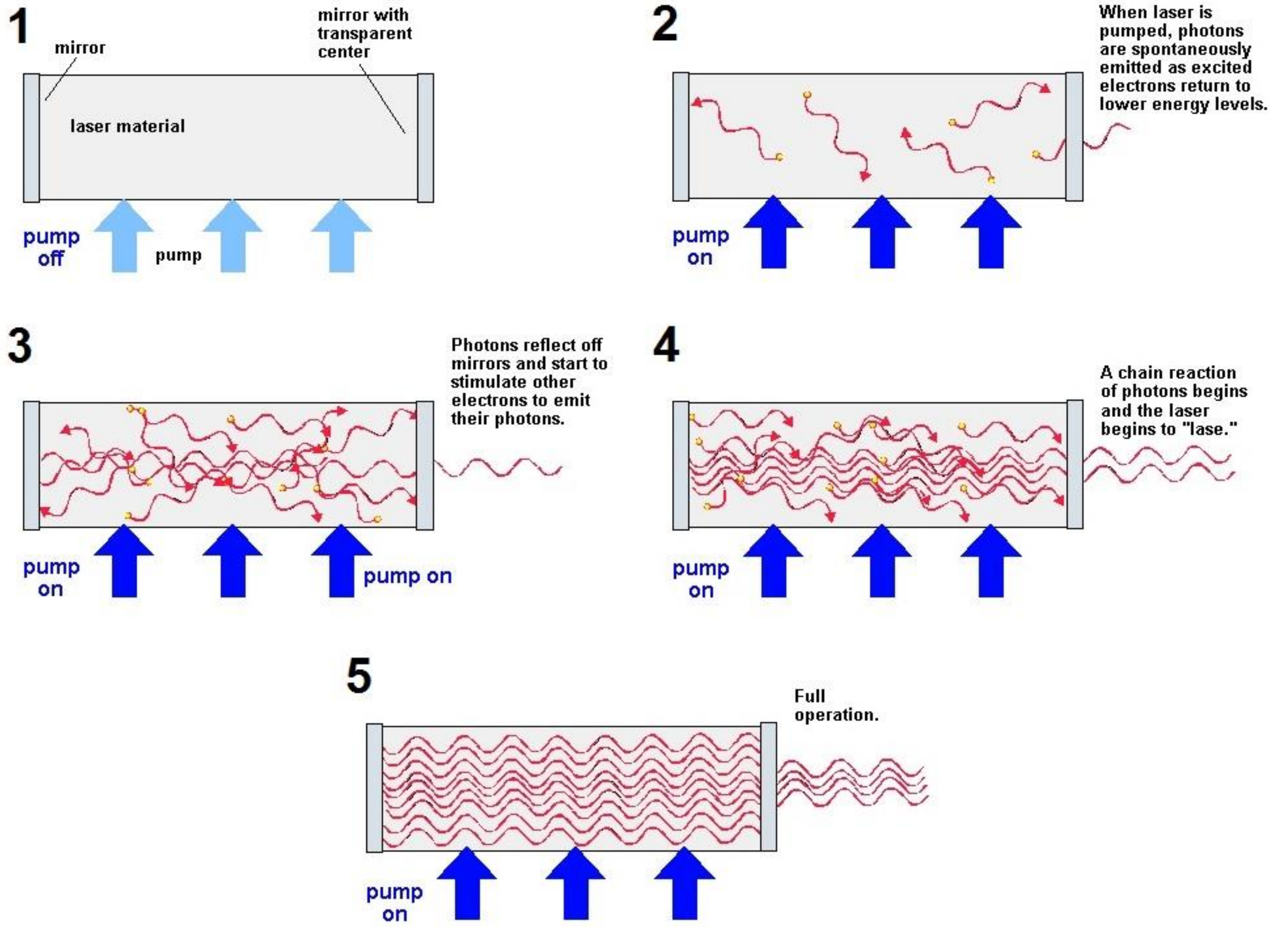

Figure 13: Schematic diagram of laser beam generation phases. [48]

1.4.2 Properties of Laser Radiation [52]

The light produced from lasers has some peculiar characteristics which make it suitable for many scientific and technological applications:

- Monochromaticity: emits light in a narrow wavelength spectrum (as exemplified in Figure 14 [53]). The degree of monochromaticity is characterized by the spread in frequency, Δν.
- Directionality: laser beams are almost parallel and maintain the source diameter for large distances. The deviation in the parallelism is a consequence of the diffraction from the edges of mirrors and windows.
- Coherency: all photons have the same phase and the same polarization. Laser radiation has both spatial and temporal coherence, characterized by the coherence length and the coherence time that are related as in Eq. 2 and 3.

$$t_c = \frac{L_c}{c} \tag{2}$$

$$t_c = \frac{1}{2\pi\Delta\nu} \tag{3}$$

Where:

- t_c = coherence time;
- L_c = coherence length;
- c = speed of light in the beam propagation medium;
- $\Delta\nu$ = line width.

Lasers having narrow line width exhibit higher coherence time and length.

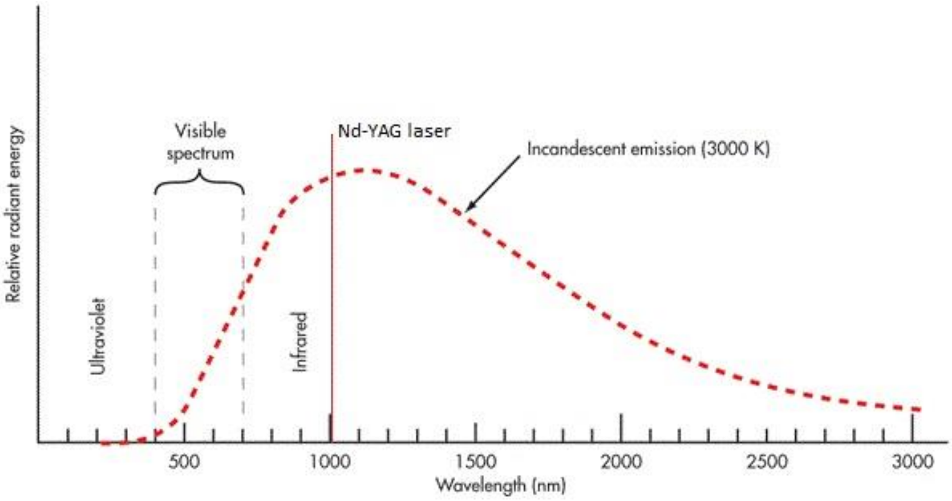

Figure 14: Comparison between the emission spectrum of incandescent light and a Nd-YAG laser. [53]

- Brightness: lasers are more intense and brighter than any other conventional light source. Brightness is defined as power emitted per unit area per solid angle [$W\ m^{-2}\ sr^{-1}$].
  Actually, the more appropriate term would be “radiance” [54].

Operation Modes

Depending on the laser medium and the pump source, the output of a laser can be operated in different ways [55]:

- Continuous wave (CW): the laser is continuously pumped and emits light continuously. The output power of a continuous-wave laser is more or less constant on long time scales but it can exhibit substantial power variations.
- Quasi-continuous wave (quasi-CW): since in continuous-wave operation some lasers exhibit excessive heating, the pump source is switched on only for short time intervals.
- Gain Switching: the pump source is turned on for very short time intervals to obtain pulses of the order of picoseconds (10^{-12}s). The short pumping phase is hold enough to store energy in the gain medium and, at the end of the pumping step, a high energetic spike is emitted.
- Q-switched: technique for obtaining high energetic short pulses (nanoseconds) from a laser by modulating the intracavity losses and thus the Q factor of the resonator.
  Pumping may be continuous or pulsed. This mode allows to produce peaks in the order of 100 MW in several nanoseconds, with an average continuous power of 100W.

- Mode-locked: group of methods allowing to produce pulses of extremely low duration ($10^{-12} \div 10^{-15}$ s).

Lasers can operate with one or more operation modes by means of hardware modifications.

1.4.3 Laser types

Depending on the nature of the active media, lasers are classified into three main categories: gas, solid and liquid. Only the industry relevant lasers will be discussed in this chapter (Main reference: [52]).

Gas lasers

Available in a wide power range ($10^{-3} \div 10^{6}$ Watts) and in a wide wavelengths range (from UV to IR), gas lasers can be operated in pulsed and continuous modes. Based on the nature of the active media, 3 gas laser types are available: atomic, ionic and molecular. Most of the gas lasers are pumped by electrical discharge. Amongst gas lasers, Carbon Dioxide (CO_2) laser (Figure 15) is the most relevant one for industrial usage.
CO_2 laser is the most efficient molecular gas laser that exhibits high power and high efficiency at infrared wavelength. CO_2 lasers typically emit at a wavelength of 10.6 µm, but there are secondary emission lines in the 9 ÷ 11 µm region (particularly at 9.6 µm). In most cases, average powers are between some tens of watts and many kilowatts. The power conversion efficiency can be well above 10%.
In the output range of the CO_2 laser, common optical materials have a high absorbance and therefore they cannot be used for windows and reflecting mirrors. Materials such as Ge, GaAs, ZnS, ZnSe are used also to transport the beam outside the cavity.

CO_2 lasers can be operated in continuous mode and in pulsed mode (200 – 1000 microseconds or 2 – 25 milliseconds), having the same maximum power of the CW mode but a better control.

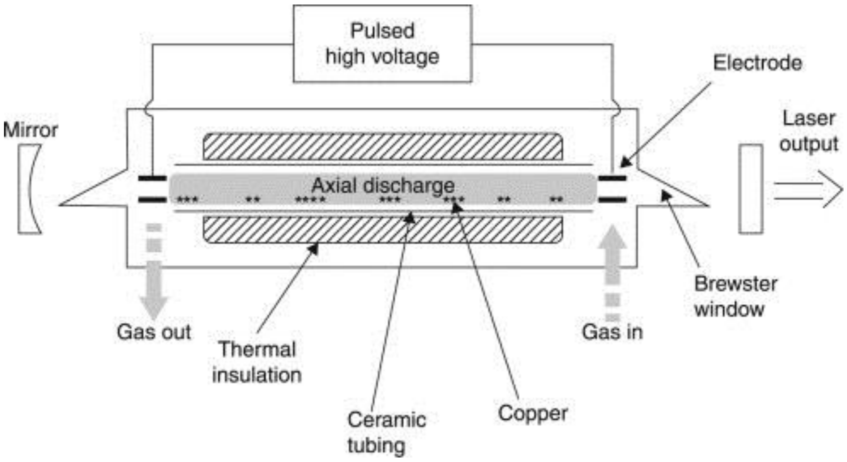

Figure 15: CO2 laser basic schematic. [52]

Solid State Lasers [56]

Solid-state lasers are lasers based on solid-state gain media such as crystals or glasses doped with rare earth or transition metal ions, or semiconductor lasers. These lasers may generate output powers between few milliwatts and many kilowatts.
Many solid-state lasers are pumped with flash lamps or arc lamps. Despite their low cost and their ability to provide very high powers, these pumping sources are inefficient and show strong thermal effects. Laser

diodes are very often used instead as pumping devices for solid-state lasers. Diode-pumped solid-state lasers (DPSS) have many advantages, such as compact setup, long lifetime and good beam quality (Figure 16 [56]).

Solid-state lasers have long radiative upper-state lifetimes (µs ÷ ms) so they are able to store a good amount of energy, thus they are ideal for nanoseconds pulse generation and Q-switching.

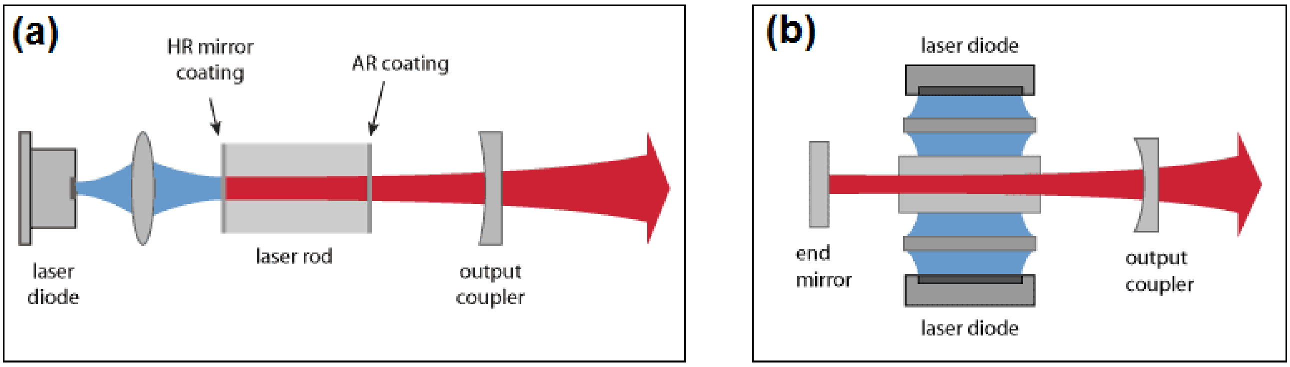

Figure 16: Typical setups of solid-state bulk lasers: (A) end-pumped and (B) side-pumped. [56]

The most important solid-state lasers are Nd:YAG lasers and fiber lasers.

Nd:YAG (neodymium-doped yttrium aluminum garnet; $Nd:Y_3Al_5O_{12}$) lasers are optically pumped using flashtube or laser diodes and emit light with a wavelength of 1064 nm, in the infrared range. These lasers can operate in both pulsed and continuous mode. Pulsed mode is operated in Q-switching mode, which can produce output powers of hundreds of MW in tens of nanoseconds.

Fiber lasers are lasers with optical fibers as gain media, resonator or amplifier. In most cases, the gain medium is a fiber doped with rare earth ions such as erbium (Er^{3+}), neodymium (Nd^{3+}), ytterbium (Yb^{3+}), thulium (Tm^{3+}), or praseodymium (Pr^{3+}), and one or several fiber-coupled laser diodes are used for pumping. To form the resonator, fiber Bragg gratings are commonly used, made either directly in the doped fiber or in an undoped fiber spliced to the active fiber. Most fiber lasers are pumped with one or several laser diodes coupled into the optical fiber.

In the manufacturing field, fiber lasers offer important advantages: light is already coupled into a flexible fiber, allowing to easily deliver the laser beam. Further, since the resonator is built into the fiber, there are not free-space optics requiring precise alignment so fiber lasers are compact and durable. Also, these lasers can operate at very high powers with high efficiency.
Fiber lasers, with a power ranging from 100 to 1000 Watts, are the most used ones for L-PBF machines.

The next fundamental element that should be analyzed before the actual melting process is the raw material. For this reason, metal powders, including their production and characterization will be presented in the following paragraphs.

1.5 Metal powders: production, characteristics and characterization

Metal powders are widely used in several powder metallurgy technologies such as Metal Injection Molding, Hot Isostatic Pressing (HIP), L-PBF, Electron Beam Melting (EBM) and Directed Energy Deposition [57].
The requirements for the powder characteristics are different according to the technique used.
The metal powder production techniques will be briefly investigated.

1.5.1 Metal powder production

Metal powders for L-PBF are typically produced by atomization, a process during which liquid metal is broken into droplets, which solidify during flight in a cooling chamber under inert gas protection. The atomization is normally accomplished by inflating high pressure gas to break up the liquid stream through a nozzle.
There are several atomization techniques for metal powder production that differ for the melting method or the atomizing technique [58]:

- Gas atomization
- Water atomization
- Plasma atomization
- Rotating disk atomization
- Ultrasonic capillary wave atomization
- Close coupled gas atomization

Gas atomization

In classic gas atomization, the metal is firstly melted inside a crucible. Once the alloy becomes homogeneous after being held in the molten state for a period of time, the melt is forced into a refractory nozzle and exposed to a high velocity gas jet which causes the liquid metal to break up into small droplets. Droplets are generated by the turbulence flow of the gas. The droplets solidify in flight and are then separated and collected in different sections of the atomizer and segregated using gravity or cyclonic separation. Figure 17-A shows a schematic representation of a gas atomizer. Some variants of simple gas atomization exist [59]:

- Free-fall gas atomization (FFGA): the basic process in which the melt goes through the nozzle as a result of gravitational force.
- Close-coupled gas atomization (CCGA): variant in which the melt is disintegrated by the direct impact of high-pressure gas right below the tip of an extended melt guide tube. It is more efficient than the FFGA.
- Electrode induction gas atomization (EIGA): particularly interesting for reactive metal (such as titanium) that reacts with the crucible. Feedstock in form of pre-alloyed bar is rotated and melted by an induction coil. A film of molten metal flows downwards into a gas stream for atomization. The material does not come in contact with either crucible or electrode during process. The powder size range is 0.1 - 500 μm and morphology is similar to FFGA [58].

The gas used must be inert for the atomized alloy so Helium, Nitrogen or Argon are typically used.
Gas atomization processes can produce high purity, spherical powders, in a dimension range suitable for additive manufacturing.

Nonetheless, there are few issues worth noting in gas atomized powders: as a result of the gas circulation in the atomizer chamber, fine particles can collide with the partially molten particles, resulting in satellite particles adherent to bigger particles. This issue can lead to lower flowability.

Moreover, due to the use of high-pressure gas, some of the gas may be trapped in the liquid metal and become gas pores in the powder.

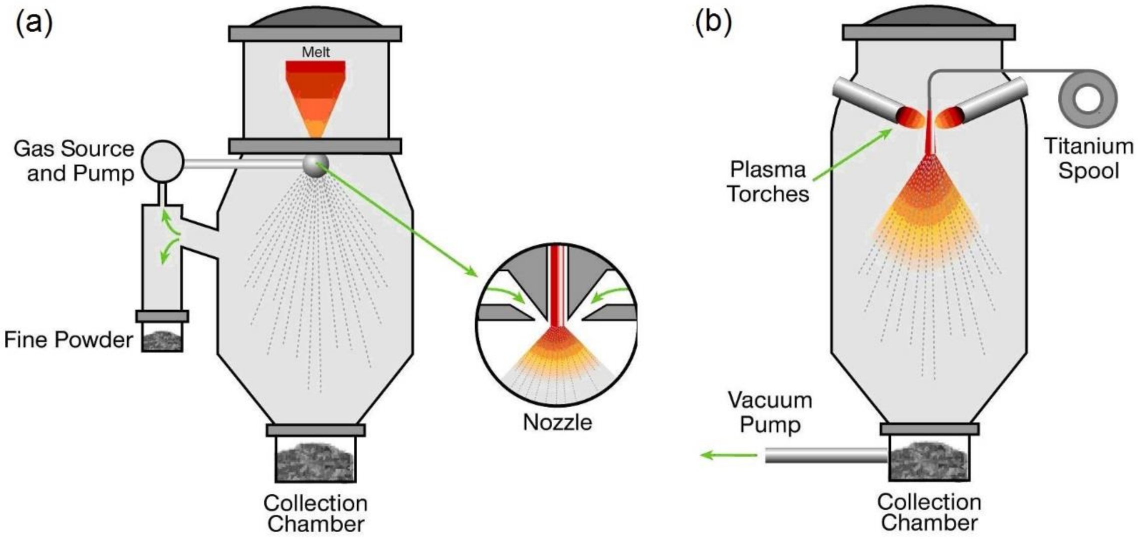

Figure 17: Scheme of (A) gas atomization and (B) plasma atomization. [58]

Plasma atomization

Pre-alloyed wire is fed into a hot zone (about 10.000 K) heated by plasma torches. The plasma simultaneously melts the wire and atomizes the melt into spherical powder. A schematic representation of a plasma atomizer is showed in Figure 17-B. Plasma atomized powder has high purity because the liquid metal does not touch any part of the atomizer that can contaminate the powder before solidification [60].
The efficiency in producing fine powder is significantly higher with respect to gas atomization. Also, the production rate can be improved by pre-heating the metal wire with an induction coil before feeding it in the plasma.
Plasma atomized powder has very good sphericity and fewer satellites particles than the gas atomized powder (Figure 18 [59]) but it still exhibits inner porosity resulting from trapped gas during atomization.

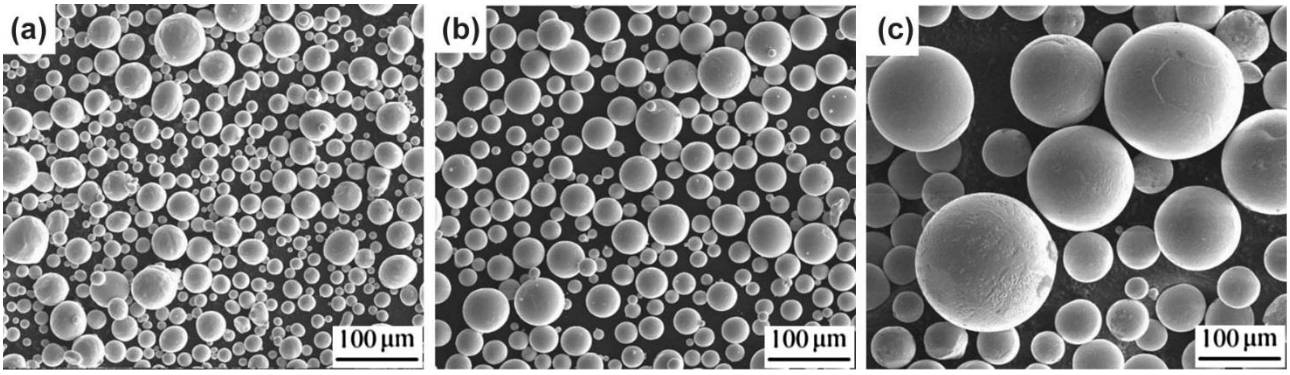

Figure 18: SEM picture of Ti6Al4V powder produced by (A) gas atomization, (B) plasma atomization and (C) plasma rotating electrode process. [59]

Plasma Rotating Electrode Process (PREP)

This technique is an evolution of the Rotating Electrode Process (REP), in which a metal electrode rod is melted by an electric arc from a tungsten tipped cathode (Figure 19). The rod spins at a speed between 3000 and 15.000 rpm so the liquid melt is spun off from the rod due to centrifugal force and forms droplets that solidify during the flight. To avoid tungsten inclusions typical of the REP process, the heat source has been replaced with a transferred arc plasma torch. As protection gas, Helium is preferred because its high thermal conductivity (10 times Argon's) and electric arc characteristics.

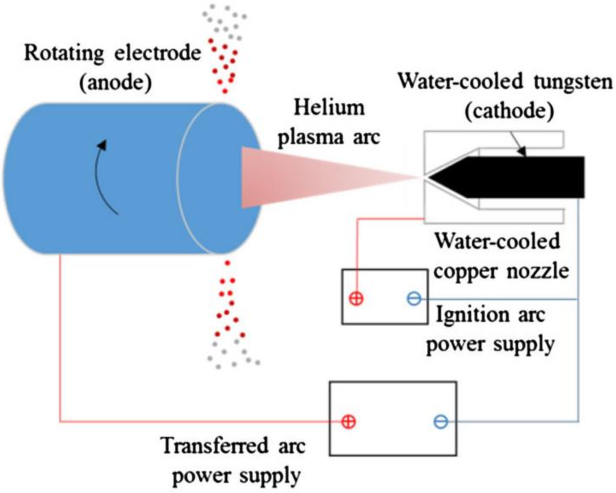

Figure 19: Plasma Rotating Electrode Process scheme. [59]

Compared to other atomizing techniques, PREP has some advantages:

- Liquid metal has no contact with other metals or ceramics before solidification, which leads to high purity powder. For this reason, PREP is generally used for high purity superalloys and titanium powders.
- The process does not induce gas pores inside the particles because high-pressure gas is not involved.
- PREP powder has fewer satellite particles compared with other methods with high pressure gas because the droplets fly radially away from the metal surface.

However, the powder produced with this technique have a size ranging from 50 to 350 μm, too coarse for powder-bed-based additive manufacturing.

Water atomization

Process similar to gas atomization where instead of a gas, a pressurized water jet (up to 200 bar) is used as atomizing medium. It is used mostly for unreactive metals such as steel and it produces irregular or agglomerated particles (Figure 23-A), in a dimension range from submicron to over 100 μm. Powder with this characteristic is unsuitable for additive manufacturing, mainly due to its poor flowability.

Centrifugal Atomization

A compromise between Gas atomization and Plasma atomization, this technique generates powder that is more spherical and has lower entrapped gas porosity than Gas Atomization but not to the quality of Plasma Atomization or PREP. However, centrifugal atomization is cheaper than both PREP and Plasma Atomization. Best suited to larger batch sizes of less reactive low melting temperature alloys, but can also make Nickel superalloys.

Mechanical Comminution

The powder is obtained by crushing, milling or grinding brittle or less ductile metals. If powders are obtained from brittle materials, the particles have angular shapes; for ductile materials, the particles result flaky. In both cases, the powder is not suitable for additive manufacturing.

Plasma Spheroidization

This technique is actually a refinement process that can be applied to a pre-existing powder, produced with cheaper and more productive techniques, to make it suitable for the desired application.

During plasma spheroidization, the metal powder is melted by a plasma torch and forms molten droplets, which solidify to form spherical solid powder before reaching the bottom of the reactor chamber (Figure 20). A unique characteristic of plasma spheroidization is that the particle size does not change during plasma processing. Plasma-spheroidized particles typically have the same nearly the same perfect round shape as the other atomized powders. Surface contamination is also significantly reduced through the vaporization of impurities and oxygen content decreases.

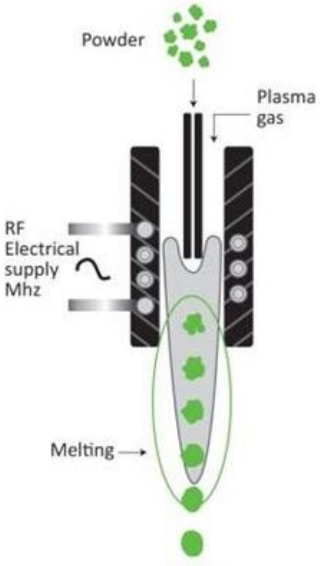

Figure 20: Plasma spheroidization process. [58]

During atomization processes, different powder size batches are obtained and are segregated in different areas of the atomizer. Multiple atomized batches can be blended and homogenized into a final powder lot to obtain the suitable Particle Size Distribution (PSD).

1.5.2 Powder characteristics and characterization

Determining the properties of the powders used in metal-based AM is a necessary condition for industry to produce consistent parts with known and predictable properties.
In fact, powder properties directly influence the behavior of the powder bed during the process and the characteristics of the manufactured parts. It is necessary to be able to test the powder in the aspects that are critical to ensure good quality parts. Hence, the main characteristics of a metallic powder that must be considered to evaluate its capability for additive manufacturing are [61]:

- Chemical composition
- Particle size distribution
- Particle size and morphology
- Density

- Flowability
- Thermal properties
- Electrical properties

All these parameters influence the behavior of the powder during the building process and the quality of the final part, as extensively investigated by Vock et al. [62]. The characterization methods are listed in the ASTM F3049 – 14 standard [63] that is currently used as a reference for all the powder characterization standards. The discussion of every parameter will be focused mainly on the effects on the building process and on the final part rather than the test equipment used to perform the test.

The chemical composition directly influences the chemical composition and the microstructure of the final part. To obtain parts with predictable properties it is necessary (but not sufficient) to have a constant chemical composition of the powder between different batches. The concentration of contaminants must be considered as well, in particular oxygen and hydrogen.
The elemental composition can be measured in an approximated way with a Scanning Electron Microscope (SEM) equipped with an Energy Dispersive Spectroscopy (EDS) system or more precisely by means of Inductively Coupled Plasma Mass Spectrometry (ICP-MS).
The crystalline phases can be explored with XRD (X-ray Diffraction) or with XPS (X-ray photo spectroscopy).

The particle size should be fine enough to allow for the spreading of a powder layer with a minimum thickness of 30μm (see Figure 24 as an example). For the L-PBF application, particle size should be between 10 ÷ 45 μm [59].

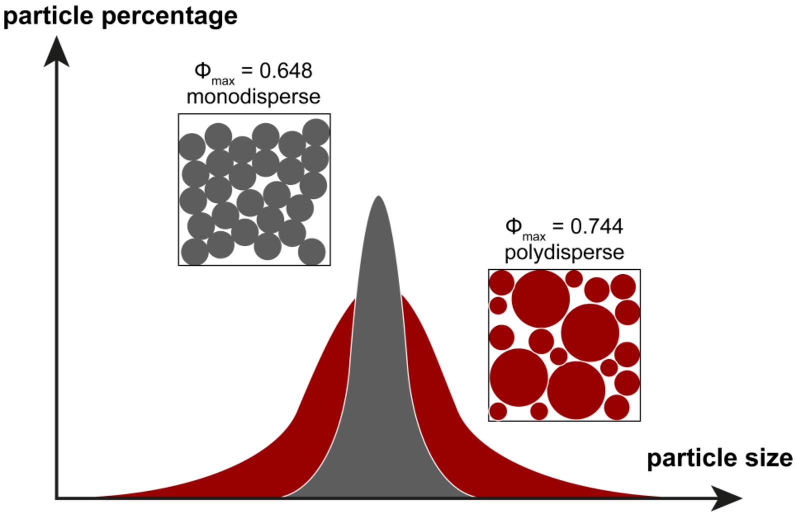

Figure 21: Effect of particle size distribution on the maximum packing density for spherical particles. [64]

Further, the particle size distribution (PSD) should ensure a good packing between the particles. In fact, particles with the same dimension would not efficiently fill the volume, causing a low tap density of the powder bed. A polydisperse powder batch, on the other hand, would fill the volume better, ensuring higher tap density of the powder bed, hence, lower volume alteration after powder melting.
Powders with a large PSD have a better packing ability, so a higher tap density with respect to monodisperse powders (see Figure 21 [64] as example). Generally, the particle size follows a Gaussian distribution. The main parameters of a PSD measure are the cumulative indexes D_{10}, D_{50} and D_{90} so the particle size at the 10, 50 and 90% of the cumulative undersize PSD (Figure 22 [65]).
The PSD can be measured by sieving systems or by laser diffraction methods.

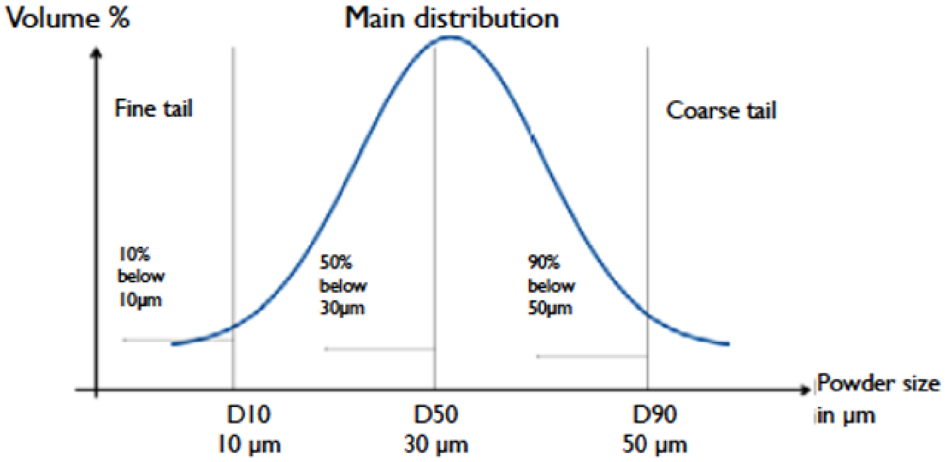

Figure 22: Example of D10, D50 and D90 on a PSD curve for a 10-50 microns powder. [65]

The shape of a particle can be defined by some factors such as the aspect ratio and the circularity. Image analysis software can be used to calculate the shape factors to get experimental numerical data, however, a visual check can be sufficient to evaluate the shape of some particles. The best technique is acquiring images with SEM that gives quasi-3D images at high magnification and resolution (Figure 23 [66]). The particle shape is critical for the flowability of the powder.

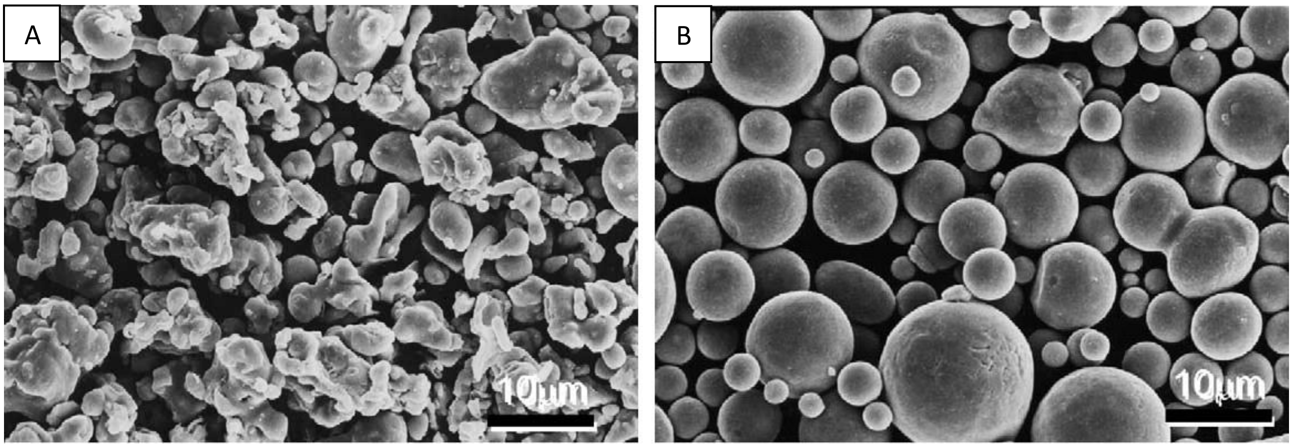

Figure 23: SEM images of (A) water atomized and (B) gas atomized 316L powder. [66]

Powder flowability is the result of the combination of the effects of several other parameters, some intrinsic of the powder and some other related to the environment [62,67]:

- Particle size and PSD;
- Particles shape;
- Satellites;
- Moisture;
- Electrostatic charge.

Generally, powder with good flowability should have a spherical shape and reasonably large particle sizes [59]. The flowability of a powder must be considered because it is related to the powder capability to be homogeneously spread into thin layers on the machine platform (Figure 24 [68]).

Flowability can be measured by means of standardized funnels. The procedure is described in the standards B213 - Hall flowability test [69] and B964 - Carney flowability test [70]. These measurement methods are based on the measure of the time that a determined powder quantity takes to pass through a standardized funnel.

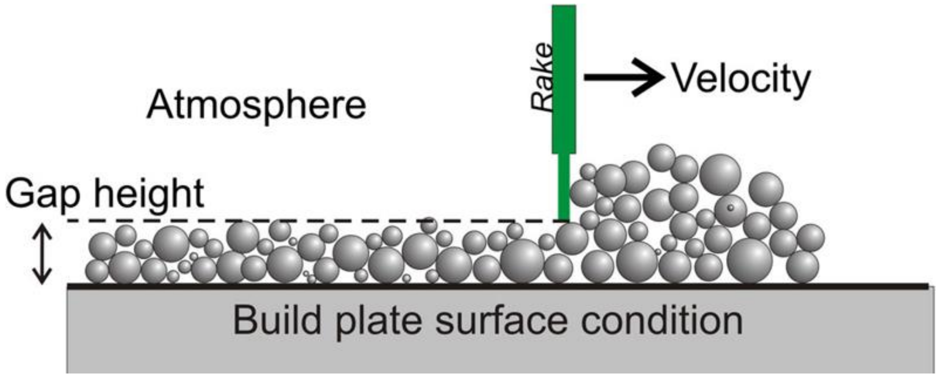

Figure 24: Layer deposition scheme in a powder bed fusion machine. [68]

1.6 Laser beam – powder interaction and melt pool generation

After understanding the basics of the laser beam and metal powder characteristics, the interaction between them can be examined. The phenomenon is really complex and intensive researches are currently focused on its correct simulation. Thus, in this chapter, a basic explanation is provided.

Firstly, when the laser beam irradiates the powder bed, 4 main phenomena occur [71] (Figure 25 [72]):

1) Absorption: part of the radiation is absorbed by the powder particles, generating heat inside the particle, until it melts.
2) Transmission: part of the laser radiation is transmitted through the powder towards the powder layers below.
3) Forward scattering: part of the laser radiation is transmitted in the powder bed through the scattering with powder particles.
4) Backward scattering: part of the laser beam is reflected by the particles and directed outside the powder bed.

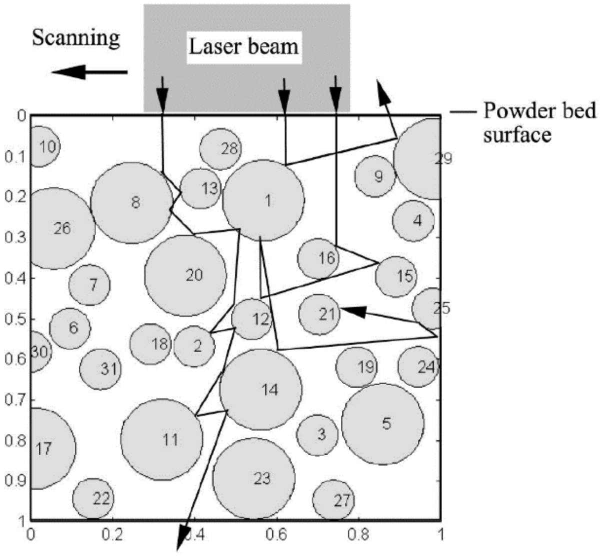

Figure 25: Simulation of the interaction of laser beam over a 1 mm depth and width of metal powder. [72]

When the laser beam irradiates the powder bed, all these phenomena occur. However, their relative importance depends on various factors, such as powder size, powder bed density and material properties.
As a result of such interactions, the actual absorptivity of the powder changes and the laser power intensity decreases as the beam penetrates through the powder bed. The depth at which the absorbed intensity decreases to 1/e (~37%) of the initial absorbed intensity is defined as the Optical Penetration Depth (OPD) [71].
In dense metals, OPD is less than 100 nm. However, at the surface of a powder bed, multiple reflection and absorption effects occur at a macroscopic level. Such phenomenon causes drastic deviation from the distribution of energy beneath the top surface. As a result, the actual optical penetration depth is much higher than that in dense materials.

As a result of the interaction between laser beam and powder bed a portion of powder under the laser spot is melted (Figure 26 [73]). This basic unit is called melt pool [74].

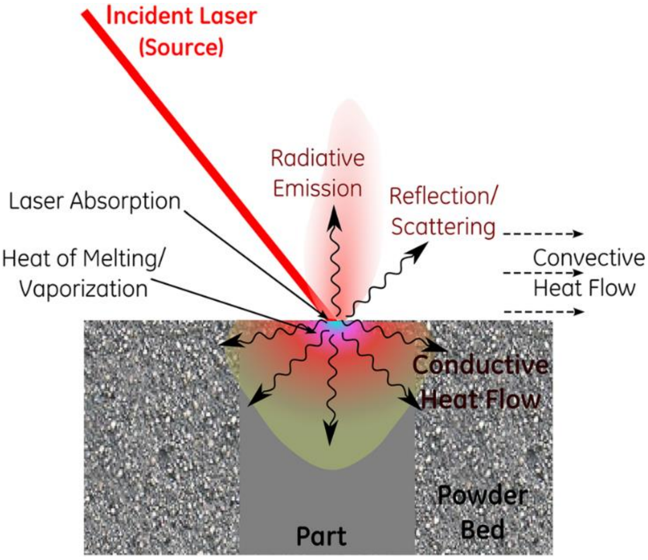

Figure 26: Representation of melt pool generation and of some involved phenomena. [73]

The melt pool can be considered as the smaller detail that can be produced in powder bed fusion. As mentioned before, its dimensions and extension depend on the interaction phenomena between laser and powder and on the laser power and scan speed. Several works, such as [75–78], are focused on the simulation of the melt pool extension and behavior, correlating these features to several parameters, especially the process parameters.

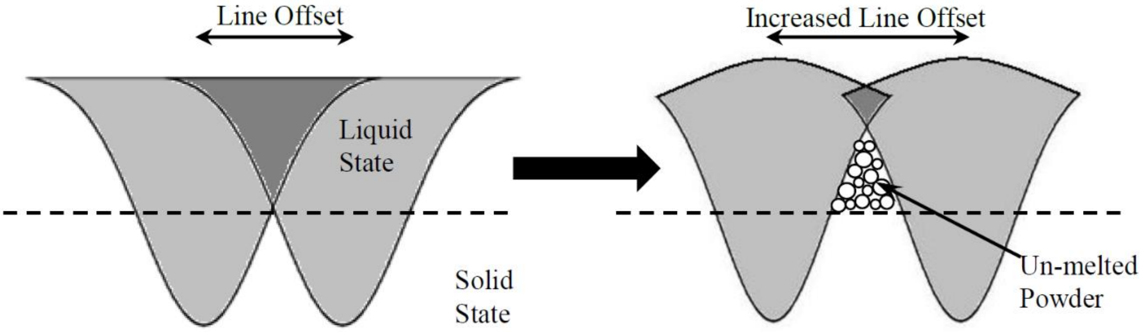

Figure 27: Overlapping between two adjacent scan lines. In the first case full melting is reached, in the second one, some powder remains unfused. [79]

In order to reach the maximum density of the material, the melt pool should penetrate the powder bed and reach the solid layer below. Further, since every layer is consolidated by the laser scanning, two adjacent scan lines should overlap in order to melt all the powder included between them (Figure 27 [79]).

The distance between two scan lines is called “hatch distance” and it is one of the main process parameters of powder bed fusion technologies. The value of the hatch distance should ensure full melting of the powder between two adjacent scan lines avoiding over-heating. A very low hatch distance would cause an excess of heat provided to the powder, causing its evaporation hence producing defects in the part; moreover, the building time would increase significantly. On the other hand, a large hatch distance would cause uncomplete melting, leaving unfused powder particles and pores in the part, typically oriented along the scan lines (Figure 28 [80]).

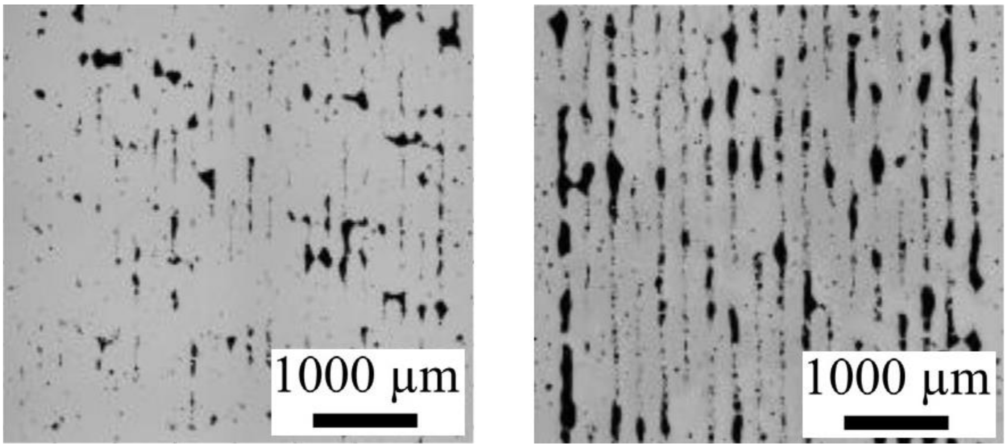

Figure 28: Effect of excessive hatch distance. Porosities along the scan lines can be clearly seen. [80]

Along with the hatch distance, other parameters are critical for the building process because they can alter the energy transferred to the powder bed by the laser beam; these parameters are the laser power and the laser scan speed. The laser power is the energy per unit of time supplied to the powder bed. It is expressed in Watts. On the other hand, the laser scan speed is the speed at which the laser beam is moved on the powder bed. It is generally expressed in mm/s.

The last critical process parameter is the layer thickness. This parameter is common to all the additive manufacturing technologies and its value mainly influences the aspect of lateral surfaces and the accuracy in the representation of the 3D file.

The combination of these parameters is commonly used to define the energy density (Eq. 4).

$$Ed = \frac{P}{h \cdot s \cdot \delta} \tag{4}$$

Where:

- Ed = energy density [J/mm^3]
- P = laser power [W]
- h = hatch distance [mm]
- s = scan speed [mm/s]
- δ = layer thickness [mm]

Generally speaking, the energy density should be high enough to fully melt the powder but not too high, to avoid material evaporation and distortion in the part.

Actually, it is not necessary to define a precise set of parameters optimal for a specific material and machine. A process window can be defined instead, in which different zones are identified according to the porosity content in the part obtained, as a function of scan speed and laser power (layer thickness and hatch distance are constants), as showed by Gong et al. [79] (Figure 29 [79]):

- Zone I: parameters capable of building fully dense parts.
- Zone II: over melting parameters, extra energy causes complex transport phenomenon, with ablation and compression of material and with large internal energies compared to chemical activation energies.
- Zone III: incomplete melting parameters, insufficient energy density causes smaller melt pools and an insufficient overlap between the scan lines, causing lack of fusion defects [81].
- Zone OH: over-heating parameters, laser irradiation produces large quantity of heat unable to be conducted away from the part immediately. Keyholing porosities can appear [81] and the part can deform due to excessive heat and eventually collide with the recoater.

As can be seen, the energy density of each point in the process window can be represented by the slope of a line between the origin and a point on the graph. The higher the slope value, the higher the energy density. However, even if the energy density meets the minimum requirement, porosity could also be included in the specimen. For example, the lower portion of the dashed line in Figure 29 demonstrates that these values of laser power and scanning speed cannot be used to fabricate porosity-free parts.

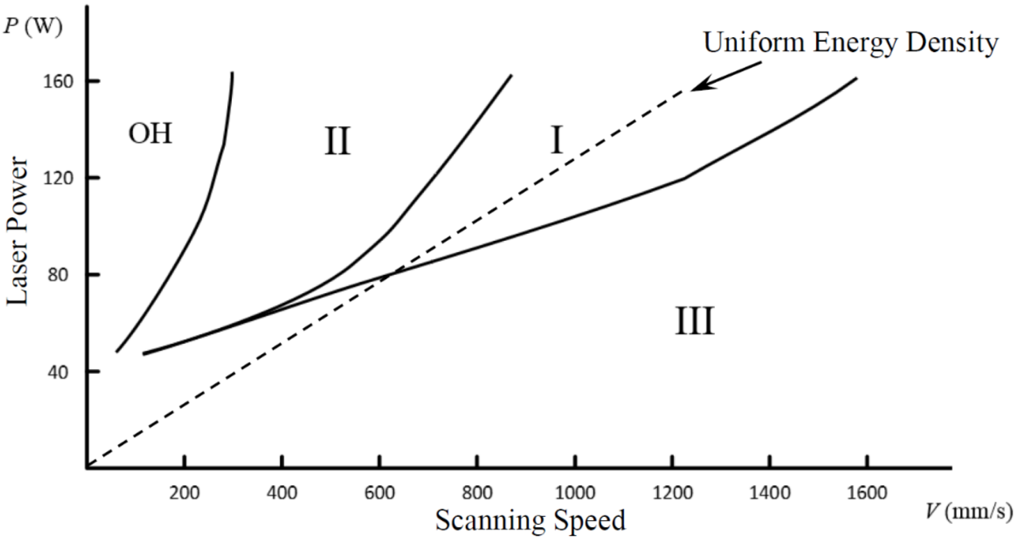

Figure 29: Example of a process window for Ti6Al4V powder. Hatch distance and layer thickness are kept constant. [79]

Hence, using the proper energy density is not sufficient to ensure full melting of the powder. Actually, some limitations exist:

- Insufficient laser power: if the laser power is too low for a certain material, the layer thickness and the hatch distance can be reduced to increase the energy density. However, if the laser beam cannot convey enough energy to the powder bed, no fusion can occur.
- Excessive scan speed: an excessive scan speed can cause balling due to a variant of Plateau-Rayleigh instability theory [82].

As mentioned before, the materials obtained by AM, hence by L-PBF, exhibit anisotropic microstructure and behavior. This is due to the layer-wise process and to the directional consolidation of the scan lines. However, as will be shown later, in L-PBF, if the process is sufficiently optimized to build consistent parts, the difference in the properties measured along various directions will be not significant [12].

In case, some heat treatments can homogenize the microstructure and mitigate possible differences.

Summing up, to achieve high density and the satisfactory mechanical properties, the correct energy density should be chosen and the process parameters should fall within the optimal process window. Otherwise, defects can occur in the part.
The typical defect types that can be found in L-PBF parts will be discussed later. Firstly, a brief explanation of the scan strategies is provided.

1.6.1 Laser scan strategies

The consolidation of a layer is made by laser scan lines arranged in [83]:

- Core area: called "hatch", it can be filled using mainly two different approaches, "stripes" or "chessboard" (Figure 30 [83]). Typically, this area is consolidated using higher power and scan speed, to achieve high consolidation rate, at the expense of the accuracy.
- Contour: the boundary of the layer, it is consolidated using different parameters in order to obtain a better surface quality and best accuracy. It is composed generally by 2 or more borders.

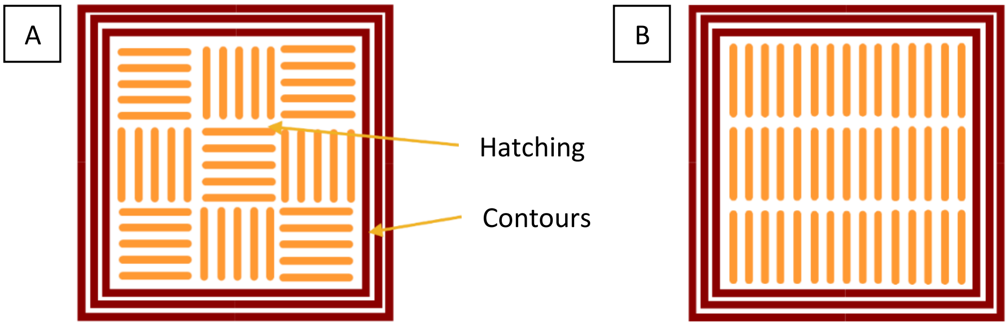

Figure 30: Different layer scanning strategies: (A) chessboard pattern, (B) stripe pattern. [83]

The hatch pattern is then rotated by a certain angle (for example, 67° for SLM Solutions machines) after every each layer to reduce residual stresses [84] (Figure 31 [84]).

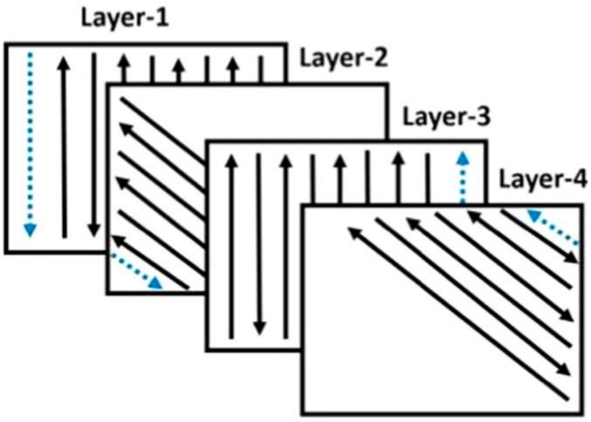

Figure 31: Hatch pattern rotation exemplification. [84]

Then, according to the areas of the layer orientated upward or downward, every layer is generally divided in 3 parts as explained in Figure 32 [83]:

- Core: a layer area that is in contact with consolidated areas of the layers below and above;
- Up-skin: a layer area facing upwards without another layer consolidated on top of it;
- Down-skin: a layer area facing downwards, touching loose powder or a support structure.

Every area is consolidated with specific building strategies according to different criteria: up-skin areas are consolidated with parameters that optimize the physical aspect of the surface, typically surface roughness and brightness. Down-skin areas are critical for the attachment with supports and should be also optimized to reach the lowest surface roughness.

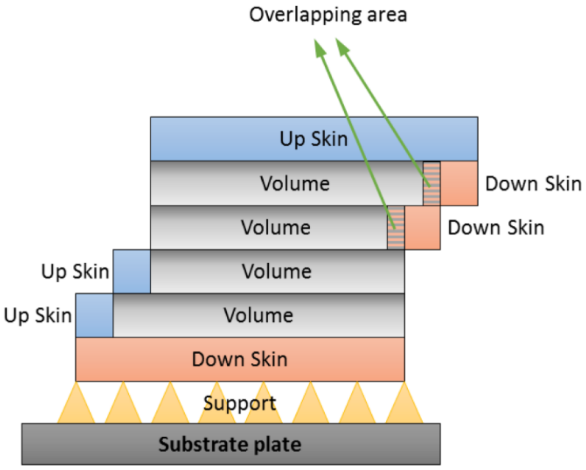

Figure 32: Representation of up-skin and down-skin areas on the layers. [83]

Other important parameters come out besides the 4 basic parameters, such as the distance from the end of a hatch line from the starting point of the next hatch line, the dimension of the overlapping area, the distance from core and contour, the rotation angle of the scan pattern and so on. The quantity of L-PBF parameters of a commercial machine can be up to 400.

1.7 Defects in parts made by L-PBF

Defects in L-PBF parts can be mainly of 3 types [85]:

Porosities

They are usually small, typically less than 100 µm in diameter, with an approximately spherical shape.
They can be generated by some mechanisms:

- If the packing density of the powder bed is low, the gas trapped between the powder particles may dissolve in the molten pool and separate again without the possibility to come out because of the fast solidification.
- Gas trapped inside the powder particles during atomization can remain inside the liquid metal because of the high solubility at high temperature.
- Gas bubbles can be generated when a high laser energy is applied to the molten pool and vaporization of low melting point constituents occurs [79].

These spherical porosities are randomly distributed in the component.

Lack of fusions (LOF)

These defects are caused mainly due to the lack of energy input during the process. Some LOF defects are related to poor bonding between scan tracks (such as the one showed in Figure 28) or between layers. As mentioned before, these phenomena can occur when there is insufficient overlap between the scan tracks or if the melt pool cannot penetrate to the layer below. Therefore, LOF defects are usually distributed between scan tracks and deposited layers.
Other LOF defects can appear randomly in the part and they arise from keyhole instability [80]. These defects are characterized by big irregular pores containing several unfused particles (Figure 33 [85]).

Further, easily oxidized alloy materials, such as Al-Si and other Al-based alloys, can form a layer of oxide film at the surface of the part with residual oxygen. In this case, wettability decreases and molten metal flow is blocked, leading to a poor bonding between layers to form incomplete fusion defects [86,87].

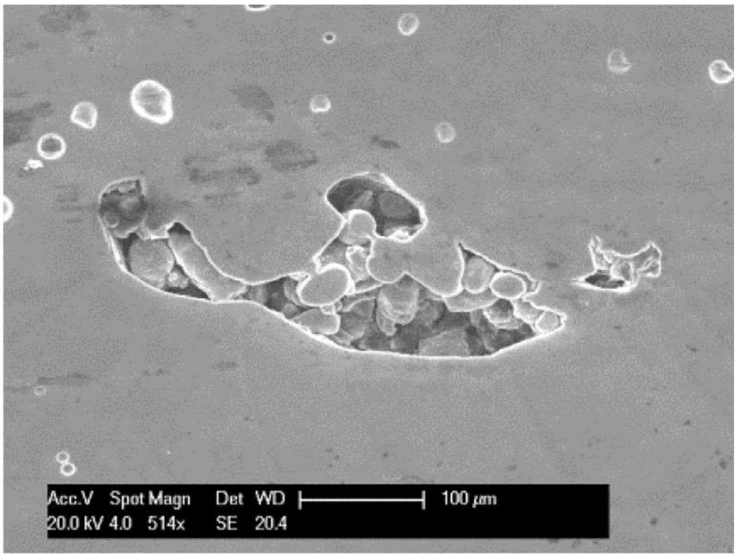

Figure 33: Lack of fusion defects with un-melted powder particles. [85]

Cracks

In L-PBF, metal powders experience rapid melting and rapid solidification. The cooling rate of the molten pool reaches 10^8 K/s [88] which creates a steep temperature gradient and consequently a large residual

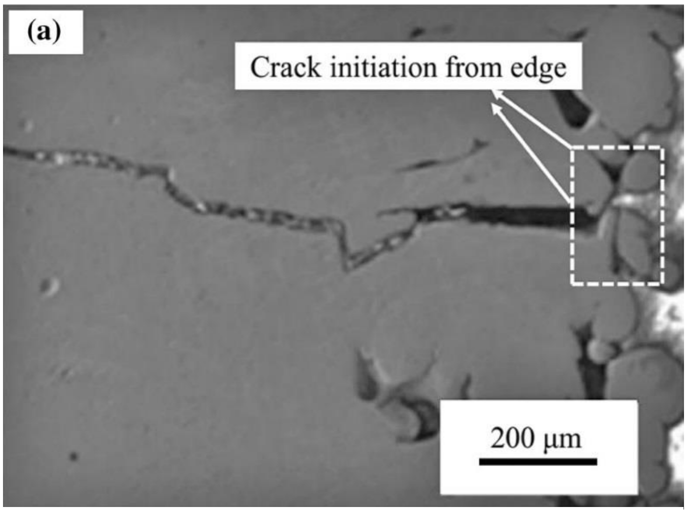

Figure 34: SEM image of crack morphology. [85]

thermal stress in the fabricated part. The combination of high temperature gradient and high residual stress often causes crack initiation and propagation.
Cracks preferentially initiate from the as-built surface that is adhered with the partially melted metal powders (Figure 34 [85]). For this reason, especially for material with a high melting temperature, after the building process, a stress relief heat treatment is recommended.

Summing up, a part produced with L-PBF technology has some peculiar characteristics as compared to parts produced with other technologies:

- Relatively poor surface quality: due to the staircase effect that derives from the layer-wise build-up strategy and the presence of satellite particles that adhere to the surface of the part [89,90]. Part roughness depends on powder characteristics and process parameters but in L-PBF technique the R_a value typically ranges from 6 – 15 μm.
- Fine microstructure: obtained due to high cooling rate of the melt pool
- Residual stresses: consequence of high heating and cooling rates
- Presence of defects: as mentioned before, defects are unavoidable, but it is possible to reduce them and mitigate the ones that are critical for the part integrity.

Hence, post processing operations are always recommended to build reliable parts. On the other hand, some parts can be used without particular post-processing operations. These parts are in the so called “as-built” state [91]. This can happen for example with aluminum alloys, because thanks to the relatively low melting temperature, the residual stresses accumulated in the part can be sometimes negligible.

1.8 Post process operations

After the building process, some operations are strictly necessary to make the part usable: firstly, the part is cut away from the building platform; afterwards, if present, support structures are removed.

However, some other post process operations could be recommended or even mandatory:

- Surface treatments: although it is possible to improve the surface finish through the appropriate choice of metal powder and processing conditions, the surface of the part can be treated to enhance the surface roughness and the mechanical properties. However, conventional tooling-based surface finishing methods and post-processing treatments are generally incompatible with AM parts due to geometric complexity. Thus, contactless processes are preferred [92].
  However, some areas of the part may need strict tolerance, hence machining can be performed with some precautions.
- Heat treatments: the part can be heated to high temperature for a certain period of time in an appropriate atmosphere condition. This is often necessary to reduce internal stresses or to tune the microstructure of the part, especially for age-hardenable materials that can benefit with significant increase in mechanical properties.

The main surface treatments that can be applied on L-PBF parts are:

- Sand blasting: by means of a jet of pressurized ceramic sand, the surface is scratched to remove partially unfused particles and obtain a homogeneous surface finish.
- Shot peening: a pressurized jet of ceramic/polymeric/metal beads (diameter ranging from 0.1 to 1.5 mm) hits the part and deform the surface, closing superficial pores and inducing superficial compressive stresses [93].
- Tumbling: the part is moved inside a barrel with abrasive plastic cones for deburring
- Machining: as mentioned before, machining is adopted only in those areas that needs strict tolerances and dimensional accuracy, such as bearing seats and threaded holes.

Since every alloy needs specific heat treatments, the available heat treatments will be discussed separately for the 3 alloys involved in this study.
However, a common heat treatment performed on L-PBF parts is the stress relief treatment. It aims at reducing the high internal stresses accumulated in the part during the building process, to limit distortion and to enhance the mechanical properties of the part [94]. Stress relief is not intended to produce significant changes in material structures, and is therefore normally restricted to relatively low temperatures in order to avoid phase transformation [95].
The heat treatment is usually performed with the part still attached to the supports and to the building platform, to keep the part in place and avoid further deformation. Otherwise, the detached part would deform to recover the internal stresses and would remain deformed after the heat treatment.

The effects of surface treatments and heat treatments on the mechanical properties of parts made by L-PBF will be discussed later.

1.9 Microstructure and mechanical properties of additively manufactured metal parts

The microstructure and the grains characteristics of a material made by L-PBF are significantly different from the microstructure of a traditionally produced material [96]. In fact, as an example, a cast metal is characterized by large columnar grains that are oriented inward to follow the solidification path toward a central region of equiaxed grains (Figure 35 [97]). The solidification starts from the walls of the mold, where heat exchange is promoted and proceeds towards the center of the cast. Hence, the cooling rate is very slow and the material generally has the time necessary to rearrange itself in stable phases.

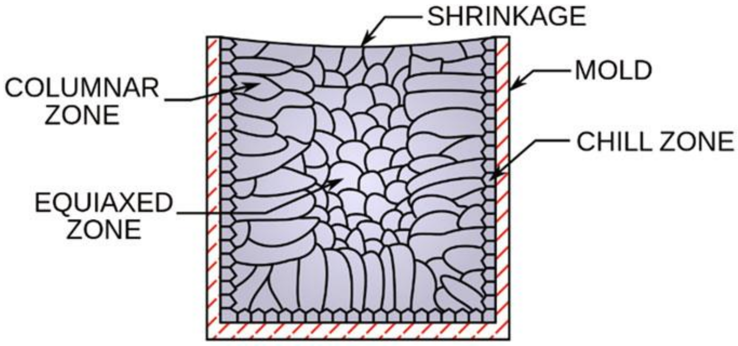

Figure 35: Schematic of the macrostructure of a cast ingot. [97]

Conversely, as-built AM metals are essentially made up of an all-welded microstructure. As a consequence of the building process, the microstructure is generally composed of multiple melt paths arranged on layers [98] (Figure 36 [98]).

Specimen preparation for microstructure observation

Firstly, the specimen must be polished, to clean the surface from scratches and to obtain a perfectly planar surface. Generally, the steps for metallography preparation are almost the same for every material:

- Cutting: a small representative specimen is cut from a bigger part
- Mounting: the specimen is embedded in thermoset resin
- Grinding: a machine is used to keep a circular plate rotating. A sandpaper is applied on the plate

and the specimen is laid on it to remove thin layers of material. This operation is performed on grinding/polishing machines, manually or automatically. By using increasingly fine sandpapers, a smooth and planar surface will be obtained, but not yet ready for observation.

- Polishing: this operation is performed using the same machine used for grinding, but using a polishing cloth with a diamond suspension. This suspension has very fine diamond particles (some micrometers) that remove a very thin layer of material, leaving a perfectly polished and planar surface.
- To improve the surface polishing, it is possible to use vibrating machines with smaller diamond or alumina particles ($\sim 0.05\ \mu$m in diameter).
- Finally, chemical etching is performed to selectively corrode the grain boundaries to highlight the microstructures. Depending on the material, different chemical solutions can be used, for example:
    - AlSi7Mg: Dix-Keller's reagent, a mixture of nitric acid, hydrochloric acid, and hydrofluoric acid.
    - Ti6Al4V: Krolls reagent (3ml HF, 6ml HCl, 5ml HNO_3, 190 ml H_2O).
    - X3NiCoMoTi: Fry's reagent of 1 g $CuCl_2$, 25 ml HNO_3, 50 ml HCl and 150 ml water.

There is a particular case where without chemical etching it is possible to observe the laser scan lines (in XY plane) and the melt pools (planes parallel to Z), because of the irregularities in the boundaries of the scan lines. This is the case of aluminum alloys, as can be seen in Figure 36.
Actually, to see these features using an optical microscope, it is necessary to illuminate the specimen with grazing light source, otherwise nothing could be observed.

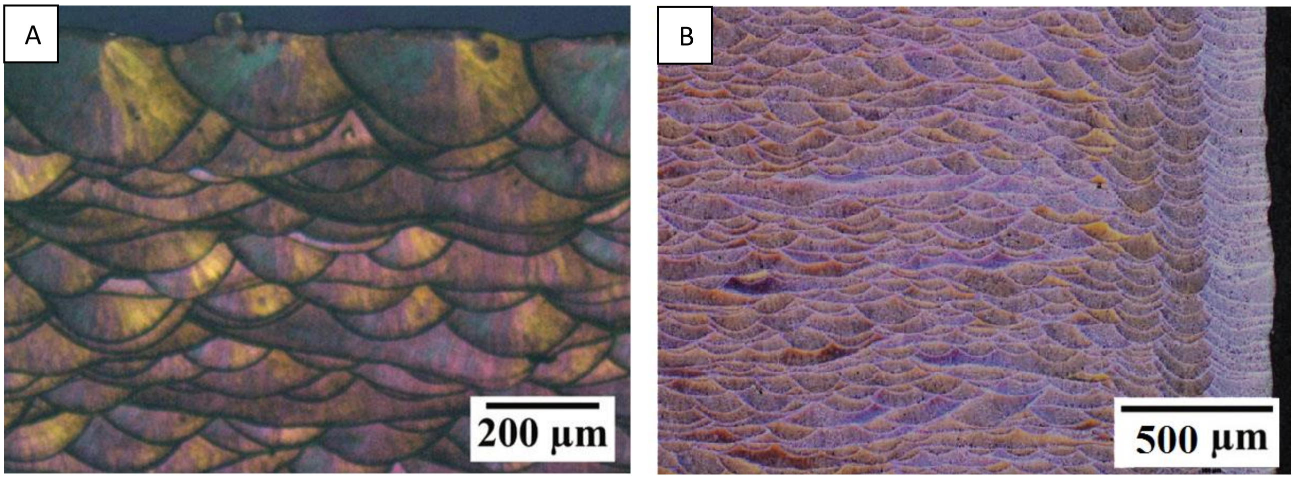

Figure 36: Optical micrograph of sections parallel to the building direction of a sample made by L-PBF in AlSi10Mg: (A) detail of the melt pools, (B) global view showing the difference between core and contour strategies [98].

1.9.1 Aluminum Alloy: AlSi7Mg

AlSi7Mg, also known as A357.0 or A357 or A13570 (with A357.0 being the Aluminum Association -American National Standards Institute (AA-ANSI) designation for this material), it is an aluminum alloy originally formulated for casting. The interest for this alloy comes from the necessity of the industries to use a material for additive manufacturing that they have been using for cast parts, to gain the same performance. Further, this alloy can be age hardened, enabling the production of high-performance light-weight structures.

This alloy is mostly used in the automotive industry due to its good performance/weight ratio and to relatively low cost.

The nominal chemical composition of AlSi7Mg powder can be found in Table 2 [99]:

Element	Si	Mg	Ti	Fe	Mn	Zn	Cu	Al
Weight %	7.00	0.6	0.25	0.19	0.10	0.07	0.05	Balance

Table 2: Nominal chemical composition of AlSi7Mg metal powder.

The microstructure of conventional as-cast A357 alloy (obtained by means of sandcasting, for example) consists of dendritic α-Al matrix, flake/fibrous eutectic Si and Mg_2Si phases in the inter-dendritic region, and Fe-rich intermetallic phases [100] (Figure 37 [100]).

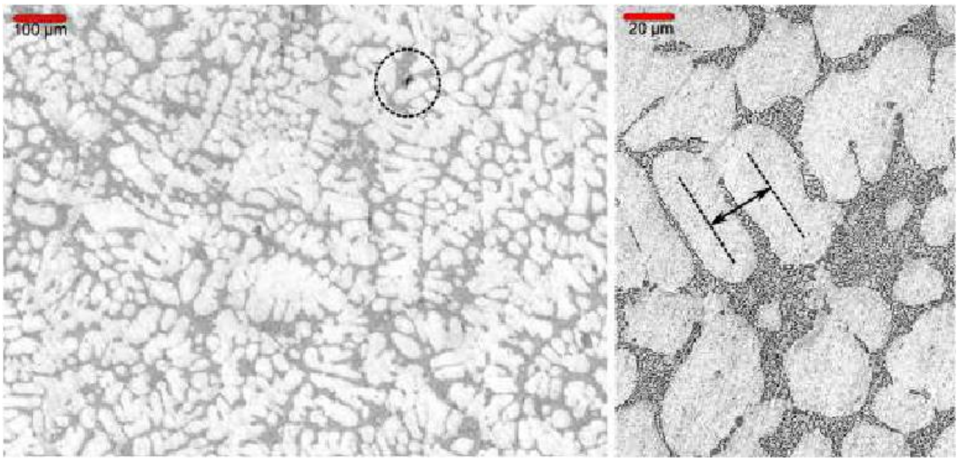

Figure 37: Microstructure of as-cast A357 alloy [100].

The same material, built by powder bed fusion (main reference for this part: [101]), in the as-built condition, shows a cellular microstructure instead of a dendritic one due to the associated fast cooling rates. This structure is composed by α-Al cells, separated by a network of extremely fine and packed circular eutectic Si

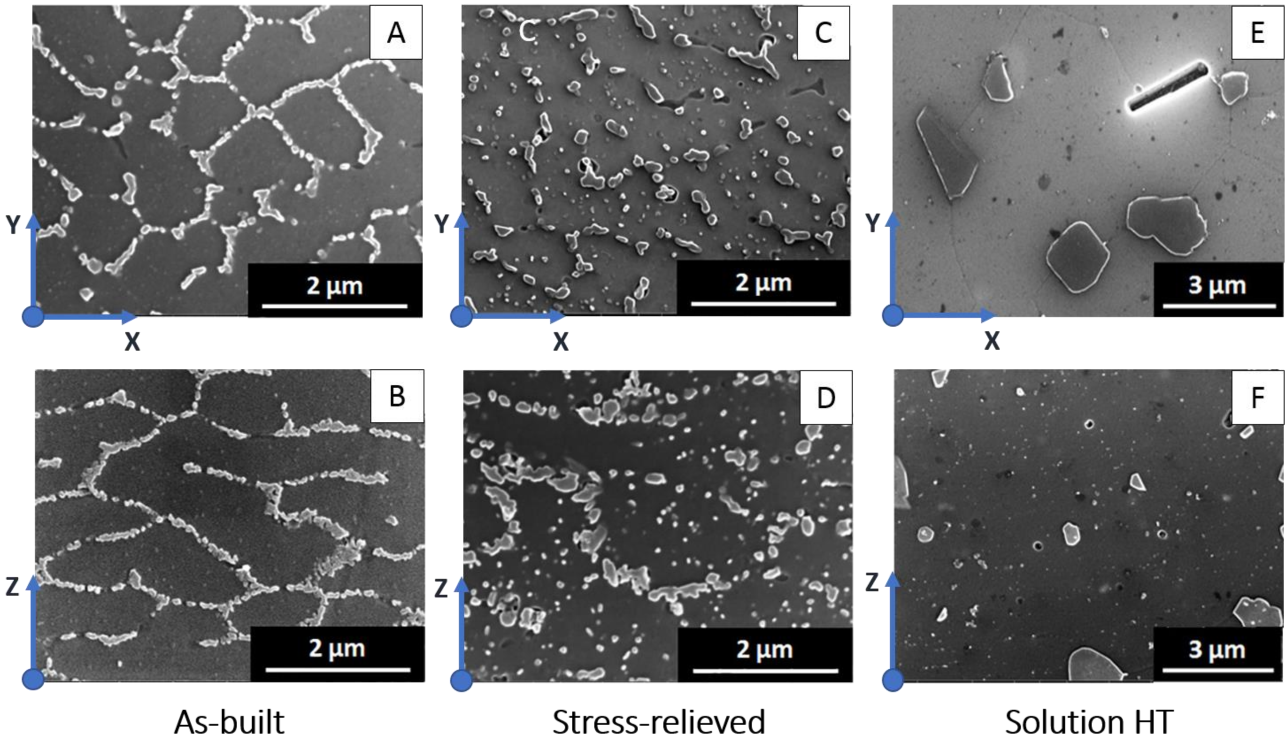

Figure 38: Secondary electrons images of AlSI7Mg in different conditions: (A-B) as-built, (C-D) stress relieved, (E-F) solution heat treated and aged [101].

particles (Figure 38-A and Figure 38-B [101]). The cell width is about 1-2 μm width and the thickness of the network is 100-200 nm. The cells are elongated along the Z axis.

Fibrous eutectic Mg_2Si is not observed clearly because of its limited volume fraction and the Si is not in a flake/fibrous morphology anymore.

Further, a fully columnar grain microstructure appears, with grains growing through most of the melt pool boundaries, reflecting the directional solidification, as can be seen in the Inverse Pole Figure (IPF) on the XZ plane in Figure 39 [101].

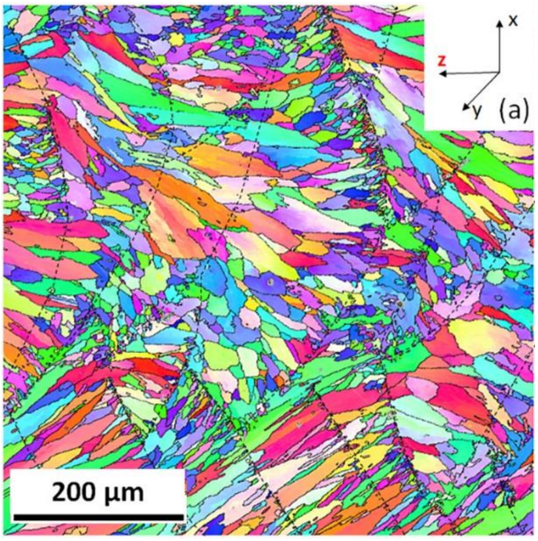

Figure 39: Inverse pole figure of vertical section of as-built specimens. Melt pool boundaries are approximated by dashed lines. [101]

This aluminum alloy can benefit of significant properties improvement thanks to the application of some heat treatments. The effects on the microstructure of some typical heat treatments performed on this alloy will be investigate from here on.

Direct Aging (DA) heat treatment, operated at 180°C for 8 hours, have no effects on the eutectic silicon network, that is still connected but some superfine Si rich particles precipitate within the cells [101].
A Stress Relief (SR) treatment, widely used on parts made by L-PBF, can be performed at 300°C for 2 hours; the eutectic silicon network broke up even though the original network can be traced (Figure 38-C and Figure 38-D [101]).

Another heat treatment can be applied to enhance the properties of some aluminum alloys, such as alloys containing Cu and Mg or Zn and Mg and the Mg Si alloys as well. In fact, it is possible to perform heat treatments in order to cause the precipitation of coherent phases in the metal matrix acting as obstacles to dislocation movement, thus strengthening the alloy. This process is called precipitation hardening and it is generally exploitable in systems in which there is a terminal solid solution that has a decreasing solid solubility as the temperature decreases.

The process is performed following some fundamental steps [102], as outlined in Figure 40 [103]:

1) Solution treatment: the alloy is heated to a temperature above the solvus line into the alpha phase and held for a period of time sufficient to dissolve the theta phase.
2) Quenching to room temperature to create a non-equilibrium supersaturated solid solution
3) Aging: the alloy is heated to a temperature below the solvus temperature to produce finely dispersed

precipitates.

The general evolution of the phases during the process is the following:

$$a_{0\,(SSSS)} \rightarrow \alpha_1 + \text{Guinier-Preston (GP) zones} \rightarrow \alpha_2 + \theta'' \rightarrow \alpha_3 + \theta' \rightarrow \alpha_4 + \theta$$

The solution treatment used for AlSi7Mg alloy is performed following these steps [101]:

1) Stress Relief (SR) at 300°C for 2 hours
2) Solution Heat Treatment (SHT) at 543°C for 1, 3 or 8 hours
3) Quenching in aqueous polyethylene glycol (PEG) polymer solution at room temperature
4) Artificial Aging (AA) at 160°C for 8 hours

The typical decomposition sequence of supersaturated solid solution (SSSS) of the Al-Si-Mg based alloys proceeds in a sequence of the following phases:

$$\text{SSSS} \rightarrow \text{GP zone} \rightarrow \beta'' \text{ phase} \rightarrow \beta' \text{ phase} \rightarrow \beta \text{ phase}$$

where β” is a needle shaped phase, β’ is a metastable phase that precipitates in form of rods with circular cross section and β is stable bulk Mg_2Si cubic precipitates [104,105].

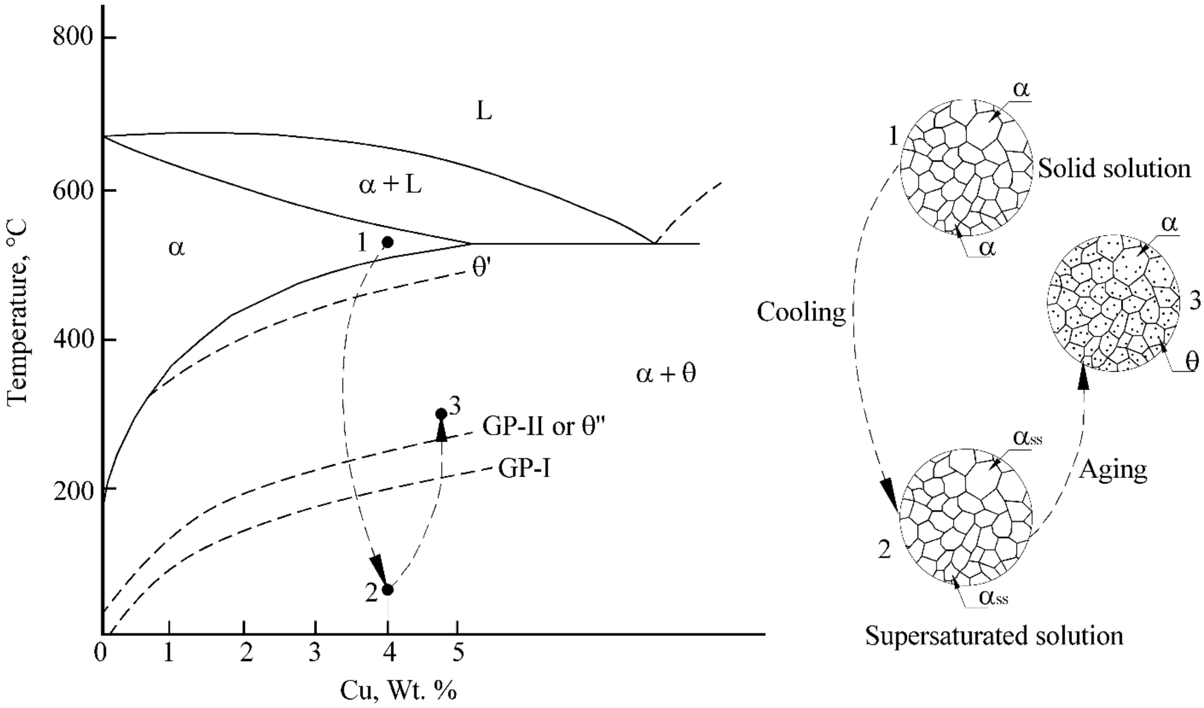

Figure 40: Aluminum-Copper phase diagram showing the solubilization and precipitation process. [103]

Hence, after this treatment, the cellular network totally disappeared (Figure 38-E and Figure 38-F); coarsened Si particles appear with irregular shapes preferentially at grain boundaries. Also, needle shaped iron intermetallic particles start to appear but their volume fraction is very low (Figure 38-E).

By increasing the solution heat treatment holding time, the microstructural features remain unchanged except for a slight coarsening of the Si particles. The same features are shown in the two directions, indicating an increasing microstructural isotropy.

The microstructure is still dominated by columnar grains and there is almost no columnar grain coarsening even after SHT.

The static mechanical properties of this alloy can be found in the literature and are listed in Table 3.

Mechanical Performance	**Yield Strength [MPa]**		**Tensile Strength [MPa]**		**Total Extension at Fracture [%]**	
Direction	XY	Z	XY	Z	XY	Z
As-built [106]	260		300		8	
As-built [107]	184 (17)	192 (17)	284 (19)	305 (15)	6.5 (0.8)	3.5 (0.7)
As-built [101]	235	195	375	355	7.5	4.5
As-built [99]	211 (18)		375 (17)		8 (2)	
As-built, mach. [108]	257 (3)		398 (13)		7.6 (1.8)	
Stress Relieved [101]	130	130	220	230	14	9
Aged T5 [106]	310		410		5	
T5, mach. [108]	309 (3)		411 (10)		4.8 (0.8)	
T6, mach. [108]	256 (4)		306 (5)		4.7 (0.1)	
Solution treated + aged T6 [106]	260		305		5	
Solution treated + aged 3 hours T6 [101]	290	280	340	320	4.8	3.2

Table 3: Tensile properties of AlSi7Mg samples made by L-PBF. In the first column the heat treatment is specified and, if performed, the surface treatment applied is indicated (e.g. mach. = machined). The tensile data are divided by building direction, "XY" for samples built parallel to the building platform and "Z" for samples built along the building direction. When present, the standard deviation is indicated.

Concerning fatigue performance, literature data is scarce, a part from some studies [91,107,109] in which as-built (not heat treated) and surface treated samples have been tested using the staircase method, resulting into an average fatigue strength of 60 MPa for as-built samples and 90 MPa for sand blasted samples (over a $2\cdot10^6$ cycles run-out).

The issue that comes out when comparing fatigue tests data is correlated to the test variables. In fact, fatigue tests can be performed with different load cycles (e.g. origin, inverted, asymmetrical) and different frequency. These variables make difficult to compare the results [110].

1.9.2 Titanium Alloy: Ti6Al4V

Ti6Al4V is an (α + β) titanium alloy that contains both an α stabilizer element (Al) and a β stabilizer element (V). α and β are titanium allotropic phases. The α phase is stable below 882°C and has an hexagonal close-packed crystal structure while β phase is stable above 882°C and exhibits a body-centered cubic crystal structure [111]. α + β alloys can give a martensite transformation, hence producing high mechanical properties.

Ti6Al4V exhibits a high strength-to-density ratio, high fracture toughness, excellent corrosion resistance and superior biocompatibility. It is recognized as the most popular titanium alloy and occupies almost a half of the market share of titanium products used in the world today [112].

The interest for this alloy in additive manufacturing derives from the difficulties in the production of parts with traditional techniques due to its poor thermal conductivity and its reactivity with oxygen. Additive manufacturing allows to build complex parts in Ti6Al4V reducing material waste, manufacturing cost and lead times.

Due to its unique properties combination but the high cost, there are 3 main application fields in which it is used:

- Medical applications: due to its biocompatibility, Ti6Al4V is widely used for biomedical applications, to build femoral stems, skull implants and other bone prostheses [96].
- Aerospace: in this field it is critical to keep a very high strength/density ratio so this alloy is well exploited
- Automotive: in motorsport field and for luxury road cars, this material is used for its high performance/weight ratio.

Like AlSi7Mg, also Ti6Al4V can be solution treated to enhance its mechanical properties.
The nominal chemical composition of Ti6Al4V powder can be found in Table 4 [113].

Element	Al	V	O	N	C	Fe	Ti
Weight %	5.50 ÷ 6.75	3.50 ÷ 4.50	< 0.20	< 0.05	< 0.08	< 0.30	Balance

Table 4: Nominal chemical composition of Ti6Al4V metal powder.

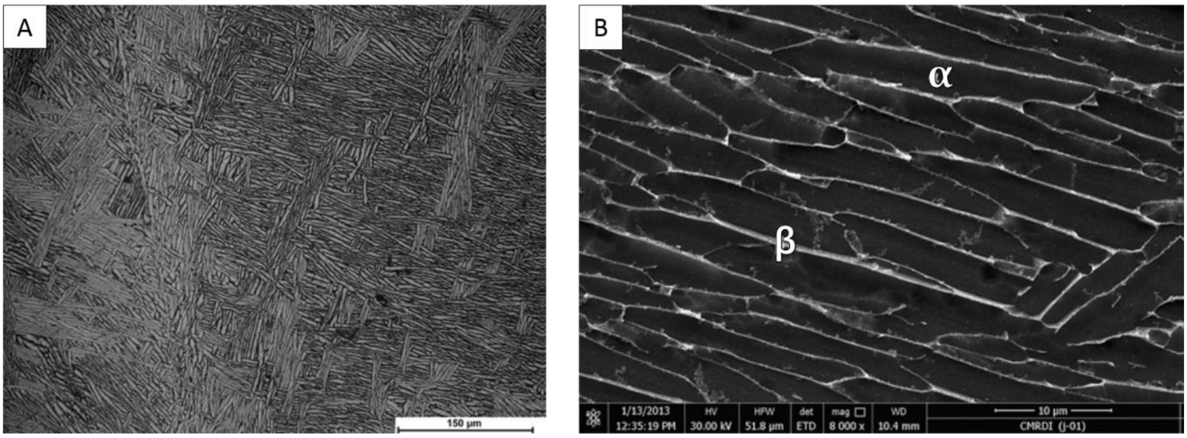

Figure 41: Microstructure of as-cast Ti6Al4V. [114]

The typical as-cast Ti6Al4V microstructure consists of Widmanstatten structures, composed of α phase formed along prior β grain boundaries and colonies of lath-type α and β lamellar structure inside the prior β grains [114] (Figure 41 [114]).
This microstructure is obtained by slowly cooling the material from the β phase. As displayed in Figure 42 [115], α lamellae (plates or laths) begin to grow from the β grain boundaries; their size decreases by increasing the cooling rate; if the cooling rate is too high, the atoms cannot diffuse and the transformation from β to α is martensitic [116].

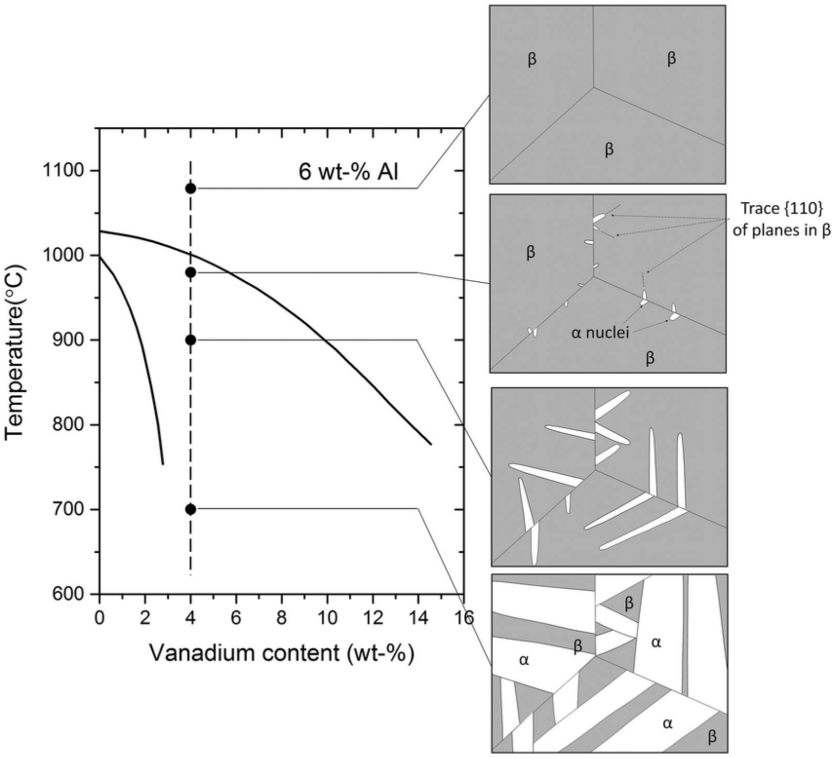

Figure 42: Phase transformations during cooling of Ti6Al4V from above β-transus. [115]

This alloy allows to make a solution + ageing heat treatment to enable the formation of Ti_3Al particles in the α phase. The ageing must be performed at T<550°C that is the solution temperature of the Ti_3Al. These particles increase the Yield stress, at the expense of the elongation at fracture [116].

The microstructure of L-PBF Ti6Al4V parts in the as-built condition consists of α' fine martensitic laths along with α+β-matrix and prior β grain boundaries [117] (Figure 43 [117,118]).

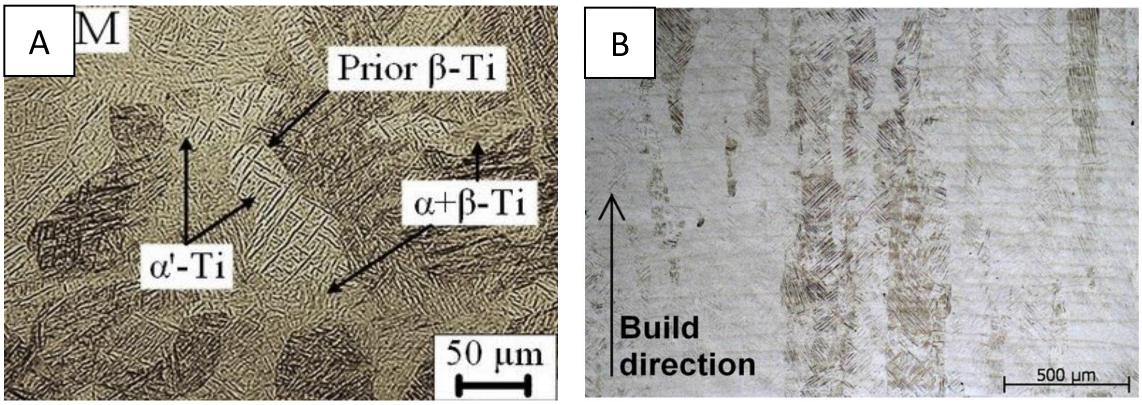

Figure 43: Microstructure of as-built Ti6Al4V made by L-PBF. (A) XY section [117], (B) Z direction [118].

In fact, upon fast cooling from above the β transus temperature, β will be decomposed by a non-equilibrium martensitic reaction instead of α + β transformation. The formation of α' martensite phase is produced by the rapid cooling through diffusionless transformation while α + β transformation is a diffusional process that needs more time to take place [112]. The same is shown by the cooling diagram in Figure 44 [119].

In the Z direction, columnar grains oriented in the building direction can be seen. These are identified as prior β grains which grow epitaxially during the process, up to several millimeters in length [118].

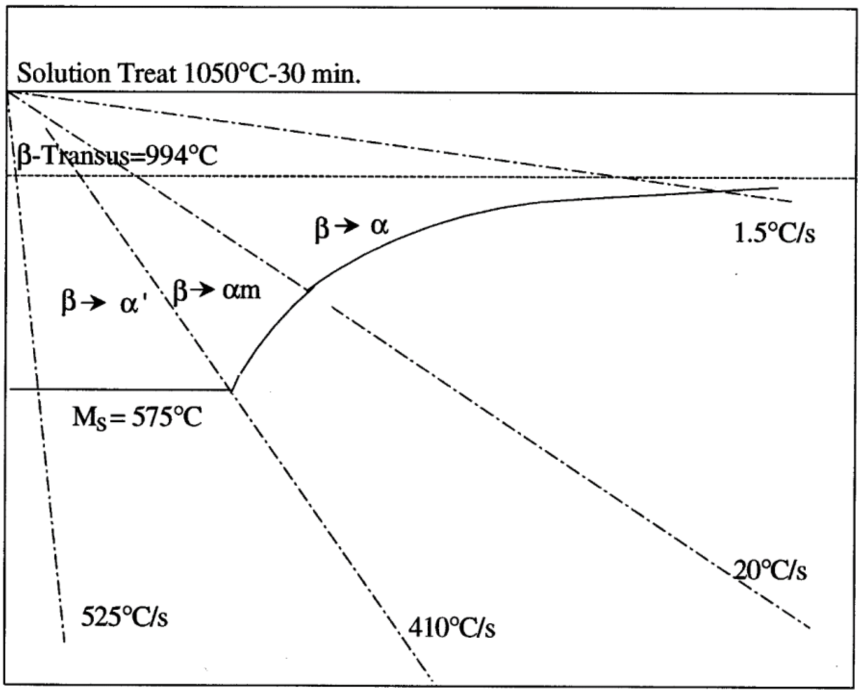

Figure 44: Schematic continuous cooling diagram for Ti6Al4V solution treated at 1050°C for 30 minutes. [119]

By heat treating the part, it is possible to modulate the microstructure and hence the properties of the material.

Vrancken et al. [118] conducted some heat treatments at different temperatures below and above the β-transus temperature (994°C). The part was cooled inside the furnace, so with a low cooling rate, in order to favor diffusion processes to enable the microstructure reconfiguration:

- After 2 h at 780 °C (below β transus), the fine martensitic structure transformed to a mixture of α and β, in which the α phase is present as fine needles (Figure 45-A).
- At 850 °C, the β-fraction at high temperature is larger, reducing the equilibrium α-fraction content. α plates are significantly coarser as the temperature increases (Figure 45-B).
- When heating above the β transus of 995 °C, a fully homogeneous, 100% β phase microstructure exists at high temperature. During furnace cooling, a lamellar α + β mixture is formed (Figure 45-C).

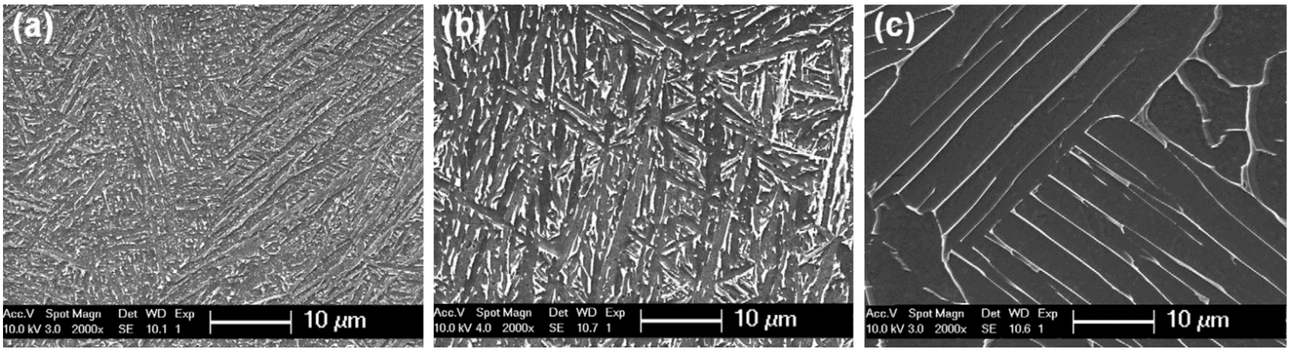

Figure 45: Microstructure of Ti6Al4V produced by SLM after heat treating at different temperatures for 2 h, followed by FC. (a) 780°C and (b) 843°C below the β transus, (c) 1015°C above the β transus. Lighter zones are β phase, the dark phase is the α phase. [118]

The influences of residence time and cooling rate are limited if the treatment is performed at temperatures below β transus because both α and β phases will tend to coarsen but will hinder each other, limiting grain growth. Also, the α fraction is fairly large so the influence of the cooling rate is very limited.

By increasing the treatment temperature above β transus, the microstructure consists of a single phase so grain growth can take place unhindered and fast, considering the high temperatures. Also, the cooling rate becomes important in the determination of the final dimension of the α phase and morphology.

At high cooling rates, the large undercooling leads to the formation of many nuclei resulting in smaller α colony size and a finer spacing between individual α plates.

Furnace cooling results in lamellar α + β and air cooling results in an α-Widmanstätten microstructure or basket weave structure. The cooling rate during water quenching is higher than 410 °C/s, leading to the transformation of all β phase in α' martensite. [119]

Concerning the solution heat treatment with ageing, this treatment is not used because the properties of the material decrease [120].

Tensile mechanical properties of Ti6Al4V alloy built by L-PBF are listed in Table 5. Lot of literature data can be found on this material, under various surface and heat treatment conditions.

Mechanical Performance	**Yield Strength [MPa]**		**Tensile Strength [MPa]**		**Total Extension at Fracture [%]**	
Direction	XY	Z	XY	Z	XY	Z
As-built, not mach. [121]	972	1096	1034	1130	5.5	1.2
As-built, mach. [122]	1195 ± 19	1143 ± 30	1269 ± 9	1219 ± 20	5 ± 0.5	4.89 ± 0.6
As-built, mach. [123]	1273 ± 53	1150 ± 67	1421 ± 120	1246 ± 134	3.2 ± 0.5	1.4 ± 0.5
As-built, mach. [124]	973–1100	967 ± 10	1137–1248	1117 ± 3	7.1–12.3	8.9 ± 0.4
As-built, mach. [125]	1137 ± 20	962 ± 47	1206 ± 8	1166 ± 25	7.6 ± 2	1.7 ± 0.3
Stress relieved, mach. [124]	952–981	937 ± 9	1049–1086	1052 ± 11	6.5–13.1	9.6 ± 0.9
Annealed (High T, superslv), mach. [125]	913 ± 7	836 ± 64	1019 ± 11	951 ± 55	8.9 ± 1	7.9 ± 2
Annealed (high T, substrans), mach. [125]	944 ± 8	925 ± 14	1036 ± 30	1040 ± 4	8.5 ± 1	7.5 ± 2
Annealed (Low T) [125]	965 ± 16	900 ± 101	1046 ± 6	1000 ± 53	9.5 ± 1	1.9 ± 0.8
HIPed, not mach. [121]	862		931		24	

Table 5: Literature tensile properties of Ti6Al4V, distinguished by different heat treatments, surface finish and building direction

Since, this alloy, unlike AlSi7Mg, is widely used in metal additive manufacturing, more fatigue data are available in the literature, summed up in Table 6.

Condition	R	Fatigue strength [MPa]	
		XY	Z
As-built, machined [122]	0.1	550	
Stress relieved, as-built [126]	0.1		210
Stress relieved, machined [126]	0.1		500
HIPed, as-built [127]	-1	200	
HIPed, as-built [128]	-1	223	
HIPed, as-built [129]	0.1	300	
HIPed, machined [127]	-1	350	
HIPed, machined [128]	-1	513	
HIPed, machined [130]	0.1	620	620
HIPed, machined [129]	0.1	775	
HIPed, blasted [129]	0.1	525	

Table 6: Literature fatigue data of Ti6Al4V subjected to different fatigue cycles and heat treatments and with different surface finishing.

1.9.3 Maraging steel alloy: X3NiCoMoTi

Maraging steels are a special class of high-strength steels having a low carbon content. Thus, martensite possesses a body center cubic structure so it results less stressed and more ductile than the martensite formed in steels with high C content [131]. These steels can be hardened by the precipitation of intermetallic compounds at temperatures of about 480°C.

Maraging steels are well known for combining good material properties like high strength, high toughness, good weldability and dimensional stability during aging heat treatment.

Maraging steels are used mainly for two application areas: the aircraft and aerospace industry in which superior mechanical properties and weldability are required, and secondly in tooling and molds applications which need superior machinability and wear resistance [132].

The nominal chemical composition expressed in weight % of the X3NiCoMoTi can be found in Table 7 [133].

Element	Ni	Co	Mo	Ti	Al	Cr, Cu	C	Mn, Si	Fe
Weight %	17.00 ÷ 19.00	8.50 ÷ 9.50	4.50 ÷ 5.20	0.60 ÷ 0.80	0.05 ÷ 0.15	< 0.5	< 0.03	< 0.10	Balance

Table 7: Nominal chemical composition of X3NiCoMoTi metal powder.

The as-built microstructure of L-PBF maraging steel is composed by a very fine cellular structure with an intercellular spacing of hundreds of nanometers. This fine microstructure results from the extremely high cooling rate of the molten pool, which prevents the formation of secondary dendrite arms during the solidification [134] (Figure 46 [134]).

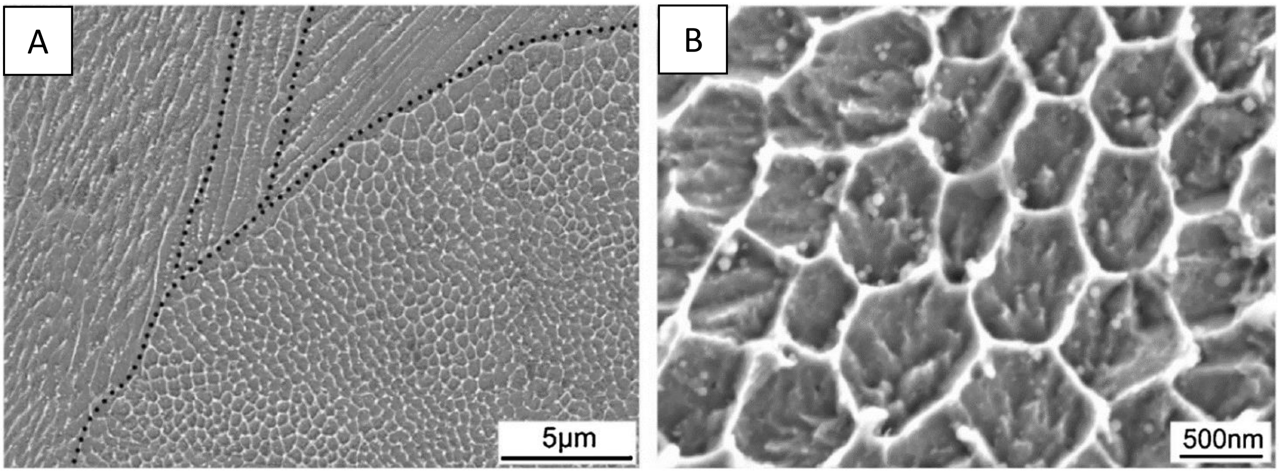

Figure 46: SEM images of as-built 18Ni-300 steel. [134]

Despite the high cooling rate, a small fraction of retained austenite persists (Figure 47 [134]). The retained austenite arises from the micro-segregation of solute elements (particularly Ni) at cellular boundaries during solidification. The enrichment in Ni stabilizes the retained austenite [134].

Ageing radically influences the microstructure of the part, depending on the temperature. Yin et al. [134] studied the influence of the ageing temperature on the microstructure and mechanical properties of 18Ni-300 steel. They found that the best ageing temperature is 490°C kept for at least 3 hours.

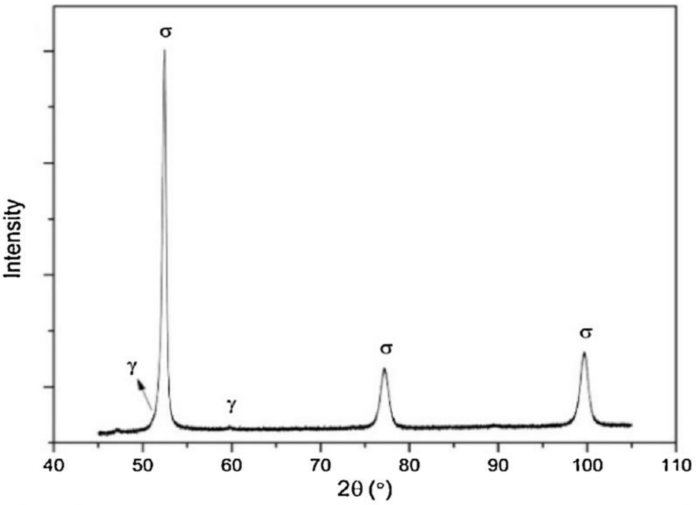

Figure 47: XRD spectrum of as-built 18Ni-300 steel. A 1.6% of austenite can still be detected (γ phase). [134]

By means of this treatment, Ni-rich intermetallic phases (e.g. Ni_3Ti, Ni_3Mo, Ni_3Al) precipitate at the grain boundaries making the cells discontinuous. The austenite content increases to 3.1%.

By increasing the ageing temperature to 590°C, the over-ageing phenomenon occurs (Figure 48 [134]): the microstructure exhibits very thick boundaries due to the prominent reversion of martensite to austenite and in fact the austenite volume fraction increases to 65.8%. In addition, over-aging causes the decomposition of $Ni_3(Mo, Ti)$ and precipitation of Fe_2Mo phase.

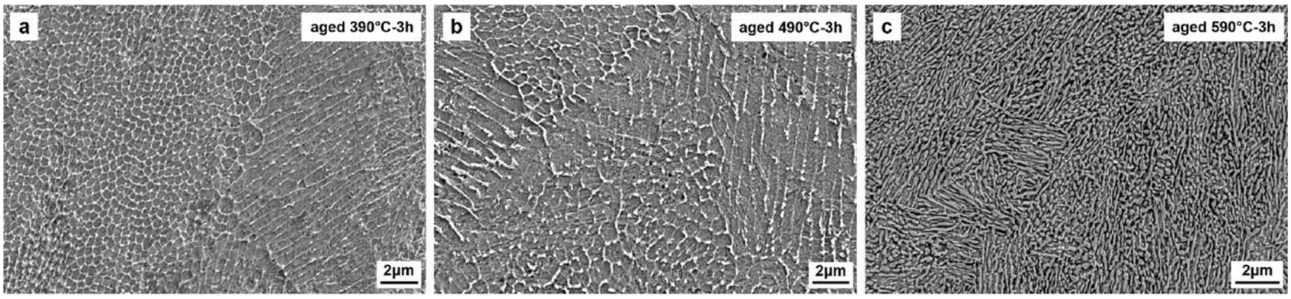

Figure 48: SEM images of aged 18Ni-300 cross-sections at different ageing temperatures. [134]

Bai et al. [135] also studied the effect of the solution treatment performed at 840°C for 1 hour. As seen for the AlSi7Mg, the laser paths and the cellular structure disappear after heating. The retained austenite is converted into martensite with lath shape. A distribution of white particles appears (Figure 49 [135]).

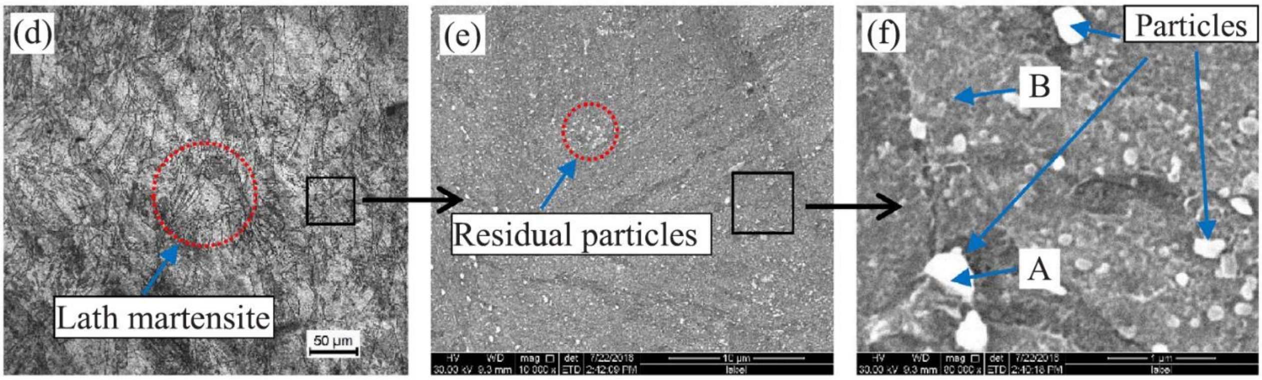

Figure 49: Microstructure of solution treated maraging steel produced by L-PBF. [135]

The microstructural changes are reflected in the mechanical properties. As shown in Figure 50 [134], the as-built samples exhibit good elongation at fracture and relatively low ultimate tensile strength. On the other hand, aging treatment substantially increases the tensile strength at the expense of the elongation at fracture.

Table 8 summarizes some literature tensile data regarding X3NiCoMoTi alloy in different heat treatment conditions.

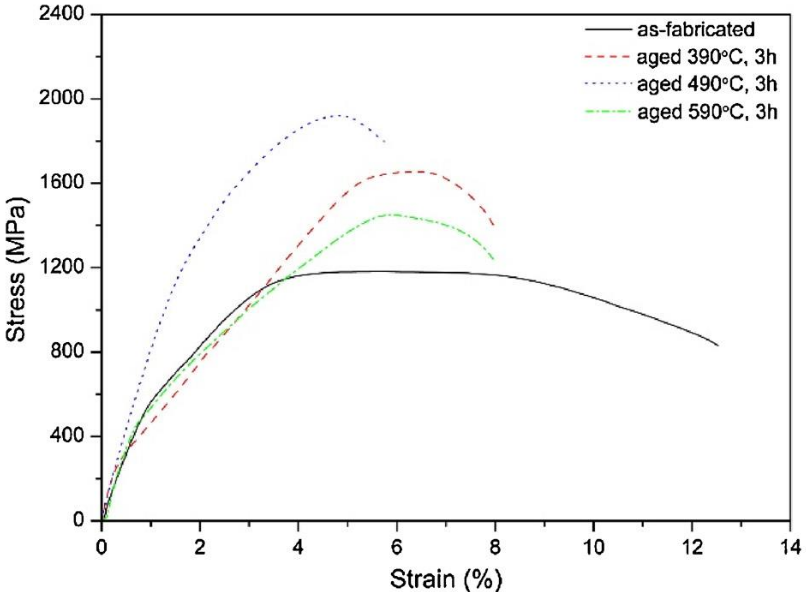

Figure 50: Stress-strain curves of 18Ni-300 at different ageing temperatures. [134]

Mechanical Performance	Yield Strength [MPa]		Tensile Strength [MPa]		Total Extension at Fracture [%]	
Direction	XY	Z	XY	Z	XY	Z
As-built [136]	915 ± 7	920 ± 24	1165 ± 7	1085 ± 19	12.4 ± 0.1	11.3 ± 0.3
Aged [136]	1967 ± 11	1867 ± 22	2014 ± 9	1942 ± 31	3.3 ± 0.1	2.8 ± 0.1
Solution [136]	962 ± 6	923 ± 16	1025 ± 5	983 ± 13	14.4 ± 0.4	13.7 ± 0.7
Solution + Aged [136]	1882 ± 14	1818 ± 27	1943 ± 8	1898 ± 33	5.6 ± 0.1	4.8 ± 0.2
As-built [137]	915 ± 13		1188 ± 10		6.1 ± 1.3	
Aged 460°C, 8h [137]	1957 ± 43		2017 ± 58		1.5 ± 0.2	
Aged 490°C, 4h [137]	1793 ± 97		1815 ±95		1.2 ± 0.1	
Aged 540°C, 1h [137]	1870 ± 54		1957 ± 54		2.1 ± 0.3	
Aged 540°C, 8h [137]	1546 ± 103		1656 ± 88		1.8 ± 0.1	
Aged 600°C, 10min [137]	1557 ± 140		1659 ± 119		1.6 ± 0.1	

Table 8: Literature tensile properties of X3NiCoMoTi maraging steel, distinguished by different heat treatments and building direction

Concerning fatigue strength, few data are available in literature (Table 9). These data are related only to machined and polished samples, tested with a stress ratio of -1.

Condition	R	Fatigue strength [MPa]	
		XY	Z
As-built, polished [138]	-1	200	300
Aged 490°C, 6h and polished [139]	-1	358	440
Aged and polished [138]	-1	210	300
Aged 490°C, 6h, polished [140]	-1 (rot. bend)	600	600

Table 9: Literature fatigue data of X3NiCoMoTi.

1.9.4 Effect of surface finishing on tensile properties and fatigue life

The surface finishing of a part can be generally described by its topological characteristics, roughness and waviness, and by the superficial stresses that can be induced by the manufacturing process itself or by a post process operation.

The aims of surface finishing processes are multiple, such as giving a specific visual aspect, protecting from the environment or enhancing the mechanical properties. When considering metal additive manufacturing, surface finishing processes aim at improving the mechanical properties and making the surface homogenous and smoother. The most used surface finishing processes for the treatment of additively produced metal parts are:

- Sand blasting
- Shot peening
- Tumbling
- Mechanical polishing
- Electro polishing
- Machining

It must be noted that a surface finishing process for additive manufactured parts should be able to reach every area of the part, generally characterized by a complex geometry. This would exclude the machining process; however, it is considered for materials testing, in fact most of the tests on additive manufactured materials are performed on machined samples, to exclude superficial effects of roughness, residual stress and contour build strategy.

Considering tensile properties, the effect of the surface finishing is generally weak. Everhart et al. [141] compared as-built and machined samples made with Ti6Al4V powder by EBM and made with 17-4 precipitation hardening powder by L-PBF. They found that machined parts show higher ductility and higher tensile strength as compared to as-built samples. However, this effect is less significant for L-PBF parts as compared to EBM parts because of the lower surface roughness of L-PBF parts. In fact, after machining, L-PBF parts show no increase in tensile strength but a 20% increase in elongation at fracture. Similar results have been found in a study [142] where Ti6Al4V specimens in as-built, machined and ISF (Isotropic Super Finishing) conditions were tested statically. The authors found almost no differences in yield and ultimate tensile strength. However, the elongation at fracture drops from 17% to 12% for as-built and ISF specimens, as compared to machined ones.

Concerning the effect of surface finishing on fatigue life, it is well known that the surface roughness significantly affects the fatigue life of a component made by traditional technologies [143]. However, the effect on additively manufactured parts should be further investigated.

Mower et al. [121] deeply studied the effects of mechanical and electro polishing processes and the effect of the orientation on the fatigue life exhibited by different materials made by L-PBF, comparing the results with conventional manufactured materials. The study shows that the fatigue life of as-built parts is highly affected by stress-concentrating defects, such as superficial or sub-superficial voids and lack of fusions that act as crack initiators (Figure 51 [121]). Neither mechanical nor electrochemical polishing was effective at enhancing fatigue behavior, due to abundant defects that remained ever present during polishing.

Conversely, Vayssette et al. [128] revealed that the fatigue resistance of machined Ti6Al4V results twice the fatigue resistance of the as-built specimens (Figure 52 [128]). The same result has been found by Nezhadfar et al. [144] for machined 17-4 PH samples and by Denti et. al [145] for Ti6Al4V alloy, where the machined samples and the tumbled and shot peened ones showed an increase in the infinite life maximum stress of about 150% against the as-built reference. Despite the machining process, the crack initiation points are always superficial or sub-superficial. Adding a polishing operation after machining increases even further the fatigue resistance as shown by Wycisk et al. [146] who observed that fatigue limit of Ti6Al4V enhanced from 210 MPa to 510 MPa.

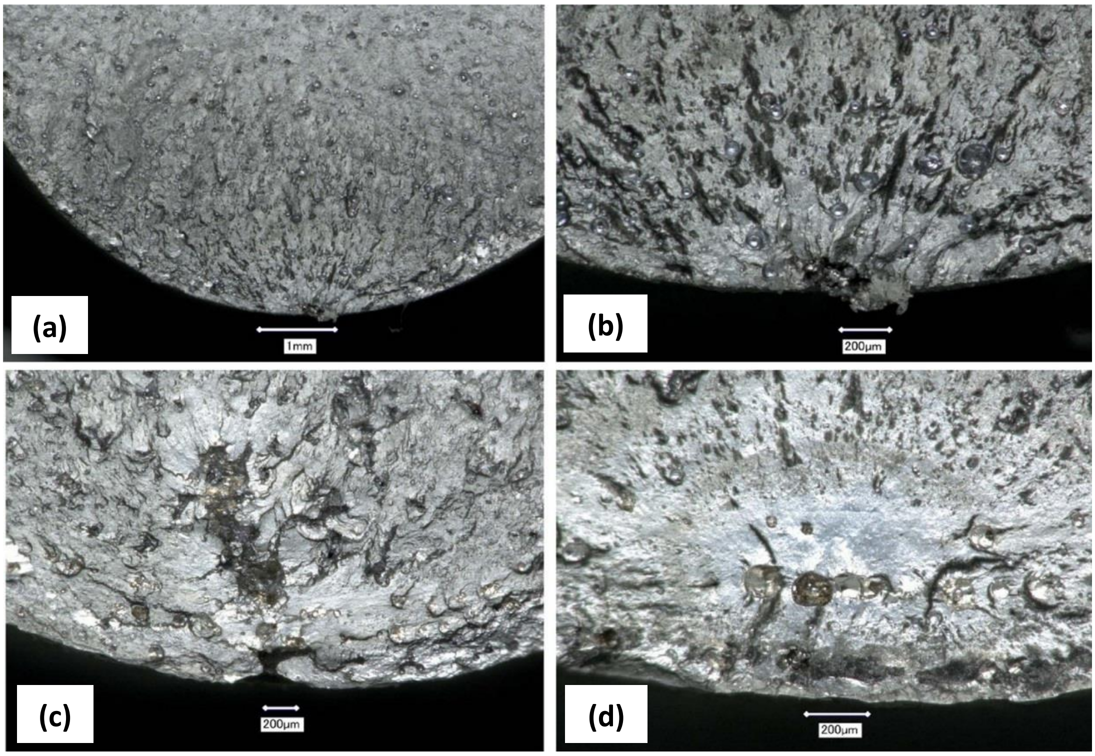

Figure 51: Fracture surfaces of horizontally built fatigue specimens: (a-b) as-built, (c-d) polished. [121]

Shot peening also increases the fatigue life by closing superficial porosities and by inducing compressive stress on the surface of the part. Numerous studies found an increase in fatigue strength between 40% and 80% [92,147–149].

To conclude, although a surface finishing processes can achieve a substantial roughness improvement and therefore also a superior fatigue behavior, there is no direct correlation between a specific roughness value and fatigue life, especially, if the surface finishing process affects intrinsic material properties [129].

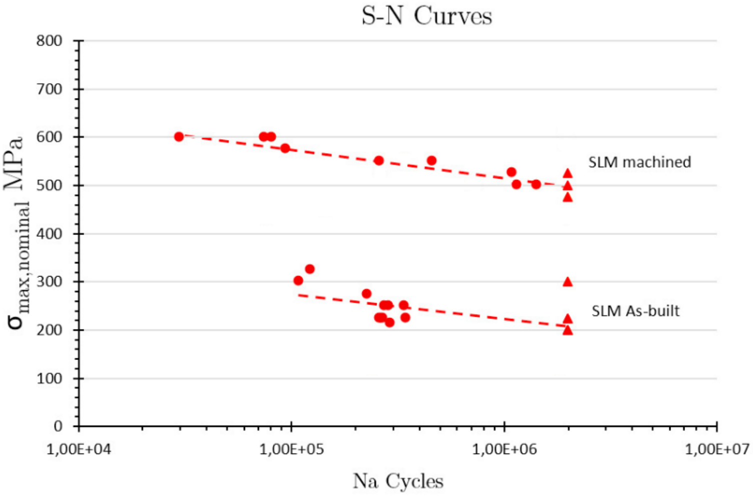

Figure 52: S-N curves of machined and as-built Ti6Al4V samples. Fatigue test performed with R = -1, f = 115 Hz, runout=2·10^6. [128]

1.9.5 Effect of heat treatments on tensile and fatigue properties

Heat treatments are a fundamental step of the manufacturing history of a metal component. Depending on the metal, a heat treatment can dramatically change the microstructure of the material, hence its mechanical properties. If the temperature and duration of the heat treatment are set conveniently, it is possible to reduce internal stresses or to allow precipitation of strengthening phases or to create a uniform microstructure [20].

Some basic heat treatments that can be applied to additive manufactured parts are:

- Stress relief
- Annealing
- Solutioning
- Precipitation hardening
- Hot Isostatic Pressing (HIP)

The effect of heat treatments should be investigated separately for every single material, since every material reacts differently, as discussed in chapters 1.9.1, 1.9.2 and 1.9.3.
However, some heat treatments are common to several materials and produce similar effects. In fact, considering the as-built condition, due to the L-PBF process, the material is consolidated in a non-equilibrium phase, with fine grains and martensite-like structures. This microstructure generally shows high yield and tensile strength but low elongation at fracture [120,150,151].
To reduce internal stresses and avoid distortions in the part, a stress relief heat treatment is often performed. As discussed in chapter 1.8, at a temperature below the re-crystallization temperature the treatment can reduce the internal stresses, without significant properties change. The internal stress mitigation can be accomplished also by heating the building platform. Generally, commercial L-PBF machines allow to heat the building plate at a temperature up to 250°C. Thus, the part is kept heated during the building process, decreasing the cooling rate so the internal stresses in the part.

Further, an annealing heat treatment can be performed at a temperature above the re-cristallization temperature to homogenize the microstructure and to promote grain growth and stress relief [150]. The effect on the mechanical properties are a decrease in the tensile strength but an increase of the ductility (Figure 53 [150]).

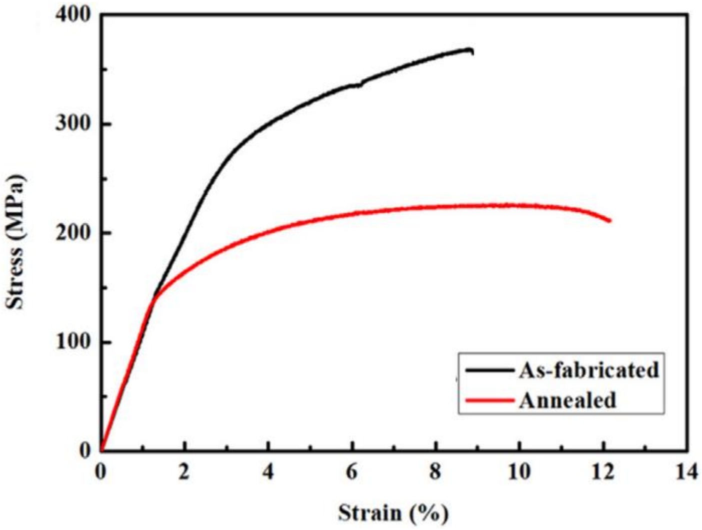

Figure 53: Stress-strain curves of as-built and annealed AlSi7Mg specimens. [150]

After precipitation hardening (solution treatment + quenching + ageing), the new properties of the material will depend on its behavior. As discussed in chapter 1.9.3, maraging steel will have an increase in yield stress and in tensile strength with a big decrease in ductility [132]. AlSi7Mg on the contrary will have a decrease in yield stress and tensile strength but the elongation at fracture will raise significatively.

HIP, thanks to the combined action of high temperature and high pressure, brings the material to the cast condition, producing a higher elongation and lower yield stress and tensile strength, compared to the as-built condition [152]. However, this process is very expensive and it is typically avoided in the industrial practice.

The effect of the building orientation is almost lost after a heat treatment performed at a temperature above the re-crystallization temperature because it tends to homogenize the microstructure [153].

2. Materials and Methods

As anticipated, in this work 3 materials were tested, for 3 final applications, as detailed in the following paragraphs.

2.1 Materials and applications

2.1.1 AlSi7Mg (A357.0) lightweight sports car component

PBF processes are an increasingly frequent choice to produce components in Si-Mg aluminum alloys that were traditionally obtained by casting. Typical examples are brackets, carters and stands.

Quality standards for luxury cars require the adoption of expensive productive solutions, mainly low-pressure permanent mold casting, with the use of cores. While they are outstanding in terms of mechanical and dimensional quality of parts, as well in terms of absence of defects, such processes suffer from high investment costs, long time-to-market and very low flexibility. All these characteristics negatively affect a production system that is characterized by very small batches, as for sports cars, where variable costs are much easier to be attributed than fixed ones.

While in the racing division metal PBF has already been adopted as a manufacturing solution, pushed by the extreme need of cutting down the time for part availability, the same cannot be said for the road-car division. The main limit is the scarce maturity, mostly in terms of reliability and predictability, of a technology that only recently included aluminum alloys among the options.

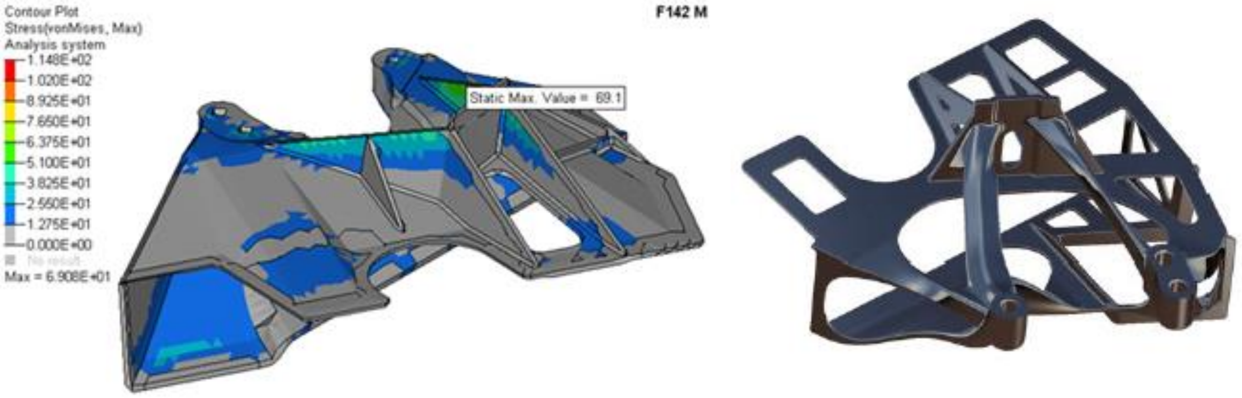

Figure 54: Engine subframe chosen as case study. In the original version (left) and the component optimized for AM (right).

In this work, the benchmark selected with the car manufacturer to evaluate the advantages of L-PBF in the automotive field is an engine subframe mount, showed in Figure 54.

The mount is redesigned by the concurrent application of topological optimization and design for AM to exploit the advantages of AM by reducing the weight and production cost and time.

Like many other automotive components, also the mount needs to withstand fatigue cycles.

AlSi7Mg was chosen because of the similarity with the alloy used by the manufacturer to produce the original part.

According to the final application and the needs of the manufacturer, the following variables were considered in the test plan:

- Heat treatment: while the effect of standard heat treatments on tensile properties has already been investigated [101,106,108,150,154], studies on the effect on the fatigue strength are ongoing. In particular, the effect of T6 heat treatment and of the ATV heat treatment (used for paint curing) has been investigated.

- Orientation: as for every part made by L-PBF, the effect of building orientation (combined with heat treatment as well), must be known.
- Surface finish: the final part has as-built surface condition. Hence, fatigue strength and tensile properties were evaluated on as-built samples. Further, machined + polished samples where tested, to test the real performance of the material with no surface finish influences.

Samples were built on an EOS M400, single laser machine by EOS Finland Oy (specifications can be found in Table 10 [155]). T6 heat treatment includes the following steps:

1) Solution annealing: 30 minutes at 540°C.
2) Quenching in room temperature water.
3) Ageing at 165°C for 6 hours
4) Air cooling.

2.1.2 Ti6Al4V medium size femoral stem for hip replacement

In the field of prosthetic components, especially for hip and knee reconstructive surgery, PBF processes are already in use for the production of Titanium alloy parts.

The advantage that this technology can offer is mainly the customization of the prosthesis and the possibility of generating a trabecular pattern that promotes osteointegration.

Femoral stems can be classified as short, medium or long depending on the dimensions (Figure 55).

Medium stems are preferable to the other two sizes, since they avoid both the risk of expulsion from the bone during the use, typical of short ones, and the centering difficulties of long ones [156].

However, while short stems are successfully produced by PBF, medium and long ones are still under investigation, because higher stress levels raise concerns over their long-term reliability. The requirements are defined by the standards ISO 7206-4 and ISO 7206-6 [157,158].

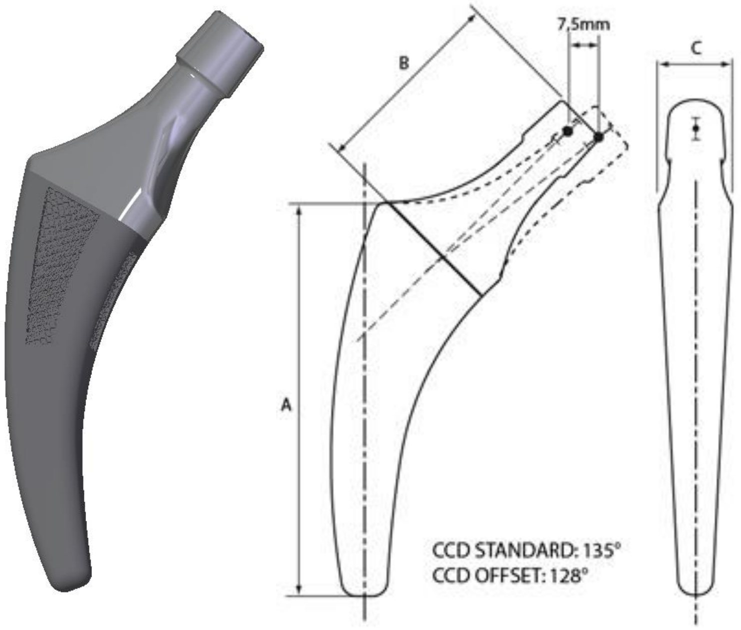

Size	A	B	C	C'
1	85	38	14	13
2	88	48,5	15	14
3	93	40	16	15
4	98	41	17	15,5
5	104	42	18	16
6	110	43	19	17
7	116	44	20	18
8	122	45	21	19
9	128	46	22	20
10	134	47	23	21
11	140	48	24	22

Figure 55: Development version of the femoral stem and measures of different size stems.

This study aims at investigating the fatigue performance of Ti6Al4V parts built by L-PBF in different conditions, in particular, the effect of a new “process package” is evaluated. This new process package aims at increasing fatigue performance of Ti6Al4V to allow the production of medium and long size stems.
A process package is a set of many process variables that are supplied by the machine producer (EOS, in this work) to the customer. These variables include:

- Raw material: powder characteristics, composition, flow properties etc.
- Machine hardware improvements, such as gas flow optimization.
- Process parameters: power, speed, hatch distance and more secondary parameters.
- Specific heat treatment.

A process package is guaranteed by the machine producer and thus is meant to be fixed and not adjustable by the customer. Thus, these details are not shared by EOS as trade secret, so the entire “process package” is taken as a black box. The “standard” and the “optimized” process package mechanical performance are investigated in this work.
Other variables have been considered, according to the final application:

- Surface finish: since some areas of the femoral stem are in the as-built state, samples in this condition were tested. Further, machined and polished samples were tested to measure the real performance of the material with no surface finish influences.
- Orientation: the tensile and fatigue properties along the two main building directions were evaluated to take into account the anisotropy of the part during the designing step.

Further, the effect of contamination in the powder was considered, due to the moderate probability to have contaminants in the machine after the material change. To this aim, a controlled contamination of 0.5% wt. of Maraging steel was added to a standard Ti6Al4V powder to investigate its effect on tensile and fatigue performance of the finished parts.

Samples were built on an EOS M290 machine by EOS Finland Oy (details can be found in Table 10 [159]) then annealed at 800°C for 2 hours in Argon atmosphere.

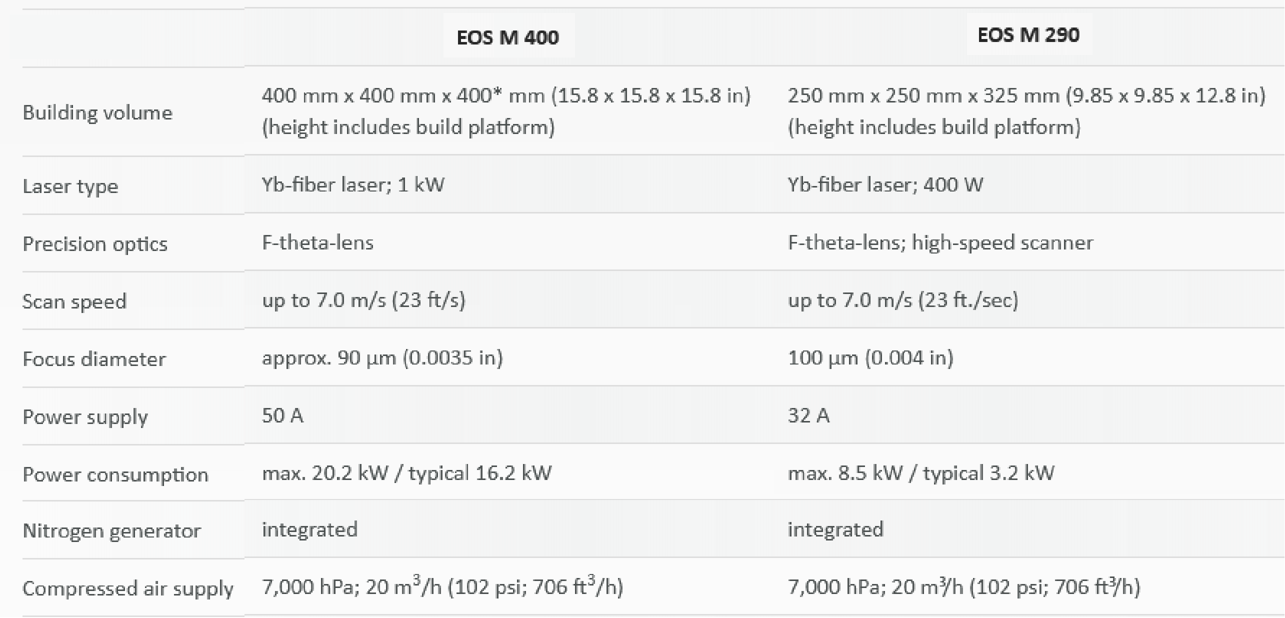

	EOS M 400	**EOS M 290**
Building volume	400 mm x 400 mm x 400* mm (15.8 x 15.8 x 15.8 in) (height includes build platform)	250 mm x 250 mm x 325 mm (9.85 x 9.85 x 12.8 in) (height includes build platform)
Laser type	Yb-fiber laser; 1 kW	Yb-fiber laser; 400 W
Precision optics	F-theta-lens	F-theta-lens; high-speed scanner
Scan speed	up to 7.0 m/s (23 ft/s)	up to 7.0 m/s (23 ft./sec)
Focus diameter	approx. 90 µm (0.0035 in)	100 µm (0.004 in)
Power supply	50 A	32 A
Power consumption	max. 20.2 kW / typical 16.2 kW	max. 8.5 kW / typical 3.2 kW
Nitrogen generator	integrated	integrated
Compressed air supply	7,000 hPa; 20 m^3/h (102 psi; 706 ft^3/h)	7,000 hPa; 20 m^3/h (102 psi; 706 ft^3/h)

Table 10: EOS M400 and M290 Specifications. [155,159]

2.1.3 Maraging steel mold insert with conformal cooling channels

The recent introduction of tool steel formulations among the range of materials for PBF systems opened the strategic application field of mold inserts produced by AM.

The main benefit that AM can bring in mold industry is connected to the geometric freedom allowed. In fact, internal and conformed cooling channels can now be produced almost without any constraint, enabling to reduce cooling time up to 50% during the injection molding process.

Generally, to produce a mold, the company involved in the present study starts from the CAD modelling of the molded part, then a fixed procedure is followed:

- CAE modelling of the injection molding process is performed;
- The areas where the cooling process is slower are selected and the mold is designed with cooling channels that run just below the active surface;
- Fluid dynamics (CFD) modelling of the channels is executed to optimize heat exchange;
- Finite Element modelling of the mold is performed with hollow channels, under the molding pressure;
- The mold is produced, combining traditional subtractive processes and additive laser-based ones.

The combination of subtractive and additive technologies allows the minimization of costs, since every simple bulky part of the mold is machined, whereas small complex inserts with conformal channels are produced by PBF with little material usage and low cost.

The benchmark selected to evaluate the advantages of L-PBF in the mold-making field is a mold insert for a polypropylene tap, shown in Figure 56. The part is produced in X3NiCoMoTi maraging steel by traditional machining for most of its volume, then the complex extremity is added by L-PBF. The company faced early mold failures during the normal usage of the mold.

Laboratory trials of the company, identified the causes for early mold failure in the contamination of the steel powder and in the instability during laser melting. However, only the latter aspect will be investigated in this work. Two process packages were used to produce samples and to evaluate tensile and fatigue performance. As for the Ti6Al4V, the details of the process packages are not shared by EOS so they are taken as black box.

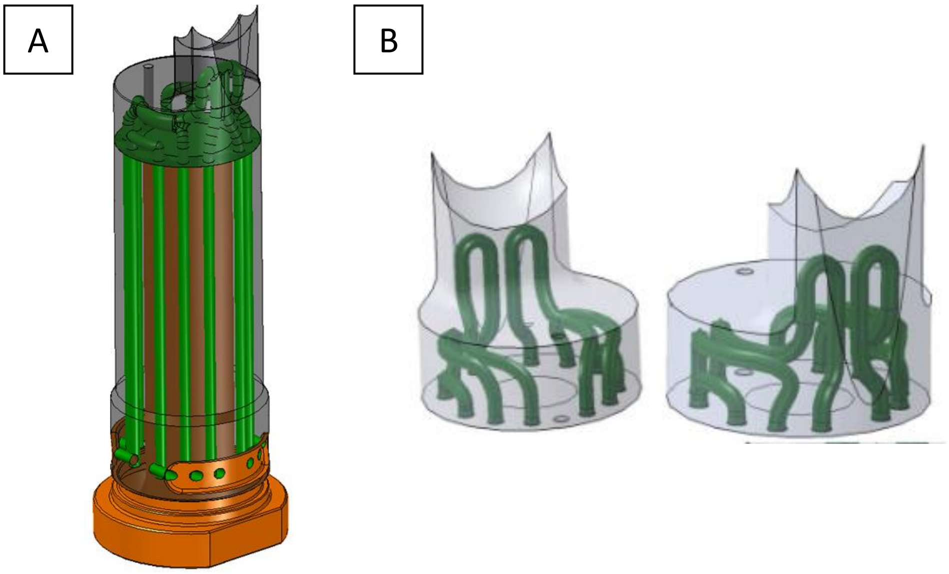

Figure 56: (A) Mold assembly of base and AM insert. (B) Detail of the insert with conformal cooling channels.

Further, since the channels act as stress concentrators, the effect of the holes inside the material was investigated. In particular, the effect of an as-built hole and of a machined hole (considered as reference) was investigated.

Samples were produced on an EOS M290 machine by EOS Finland Oy. All the samples were age hardened following EOS heat treatment procedure:

1) Solution treatment at 940°C for 2 hours.
2) Air cooling.
3) Ageing at 490°C for 6 hours.
4) Air cooling.

2.2 Sample characterization

The main test procedure followed during the tests is:

1) The diameter of the samples was measured with a micrometer;
2) Roughness measurements were performed on 1 sample per batch;
3) Samples were tested on the fatigue testing machine to measure fatigue strength following the staircase method (details will be given in the next chapters);
4) At the end of each batch, results were elaborated to calculate fatigue strength in terms of mean value and standard deviation;
5) 2 samples for each batch were selected to observe the fracture surfaces. The selection criteria are the following:
    - the sample that broke after the highest number of cycles under the first peak stress level above the average fatigue life calculated for the corresponding group (hereafter: “average samples”);
    - the specimen with the shortest life under the lowest peak stress level tested for the corresponding group (hereafter: “early broken samples”).

Density and porosity of only aluminum alloy samples were measured as well, to investigate the effect of thermal treatment.

The characterization techniques used in this thesis to analyze the characteristics of the 3 materials are:

- Tensile test: to obtain static mechanical properties;
- Fatigue test: to measure fatigue strength at a given number of cycles;
- Density measurement with Archimedes’ method: to check the density of the parts;
- Confocal microscopy: to measure the roughness of the sample surfaces;
- Optical and electron microscopy: to observe the morphology of surface fractures and the microstructures. A Nikon LV150N optical microscope and a FEI ESEM Quanta 200 were used.

2.2.1 Tensile Testing

The tensile test is the most common method used to obtain the main mechanical properties of a material, including the most important ones, namely:

- Elastic modulus
- Yield Stress
- Ultimate Tensile Stress
- Elongation at fracture

Additionally, all the stress-strain plot is obtained upon testing. This plot is very useful to evaluate the behavior of a material, such as its toughness, strain hardening capability and its failure modality.

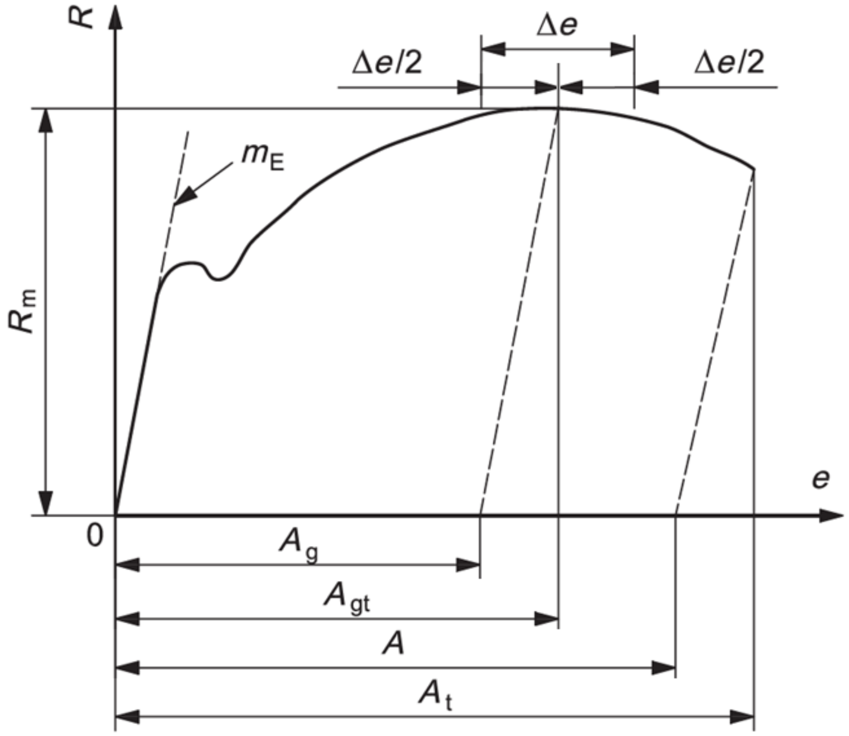

A	percentage elongation after fracture
A_g	percentage plastic extension at maximum force
A_{gt}	percentage total extension at maximum force
A_t	percentage total extension at maximum fracture
e	percentage extension
m_E	slope of the elastic part of the stress-percentage extension curve
R	stress
R_m	tensile strength
Δe	plateau extent

Figure 57: Stress (R) / Strain (e) plot. [160]

Firstly, a specimen that can be attached to the machine must be produced with the material under examination. The specimens shape as well as the test procedure, are regulated by international standards. According to the material class, different standards may be used. For metal parts the most used are ASTM E8/E8M-13, ISO 6892-1, ISO 6892-2, JIS Z2241

Specimens are then mounted into proper attach systems: one end is fixed to the machine while the other one is connected to a moving crosshead. One of the terminals is also connected to a load cell.

During the test, time, load and strain are recorded and the stress/strain plot is generated.

In this work, tests were performed with an Instron 5567, using a load cell with maximum load of 30 kN and a tolerance of ±30N. A mechanical extensometer was used, with a gauge length of 25 mm and a tolerance of ±0.1% in the measure of the percentage elongation.

The reference standard for the tests performed in this work is the ISO 6892-1 [160]. According to this standard, the test can be carried out by setting a fixed strain rate (method A) or a fixed stress rate (method B). However, the machine is not capable of working either under a fixed strain rate or under a fixed stress rate because of the slow control feedback, so a crosshead separation rate had to be set instead.
The specimens' shape was designed according to ISO 6892-1 standard (Figure 58).

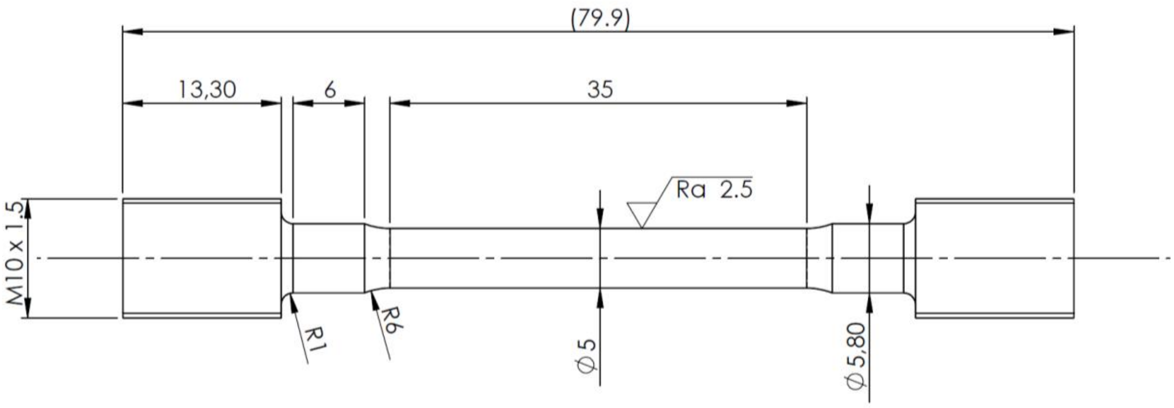

Figure 58: Tensile sample dimensions.

To test titanium specimens, two different strain rates ($\dot{\varepsilon}$) are required, according to standard ISO 6892-1, method A:

- A strain rate of $7 \cdot 10^{-5}$ s^{-1} is required to measure the elastic part.
- A strain rate of $6.7 \cdot 10^{-3}$ s^{-1} is required after the yield stress.

The speed test can be controlled by setting the crosshead separation rate (v_c). To find out a correlation between the crosshead separation rate and the strain rate, data acquired from past tests were analyzed.

The following steps were undertaken on the data of a Ti6Al4V specimen, tested with a crosshead separation rate of 2 mm/min (stress/strain plot can be seen in Figure 59).

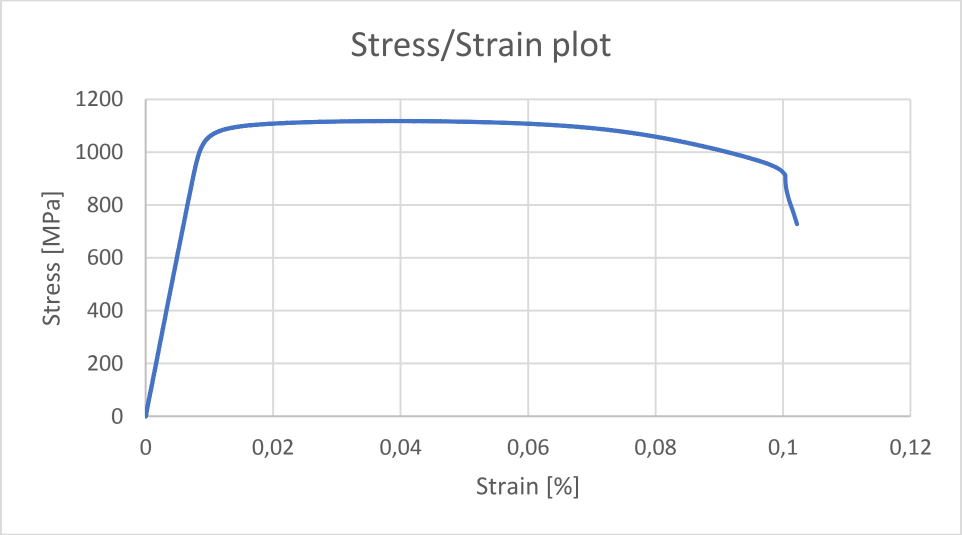

Figure 59: Stress/strain plot of a Ti6Al4V specimen, tested at a crosshead separation speed of 2 mm/min.

The data acquired during the test (every 0.01 seconds) were processed to obtain the strain/time plot (Figure 60).

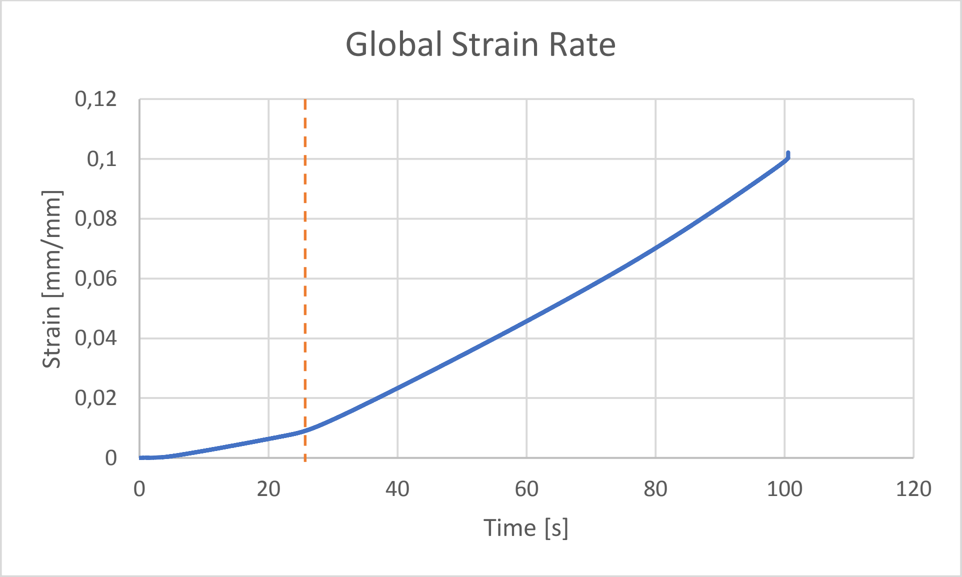

Figure 60: Strain/time plot of the Ti6Al4V specimen tested at a crosshead separation speed of 2 mm/min.

In the chart, two different parts can be distinguished: these two parts are almost linear and correspond to the elastic part and to the plastic part of the stress/strain plot, respectively (Figure 61).

To calculate the strain rate of the two parts, the curve was split in two plots; the corresponding curves were interpolated and the functions were derived.

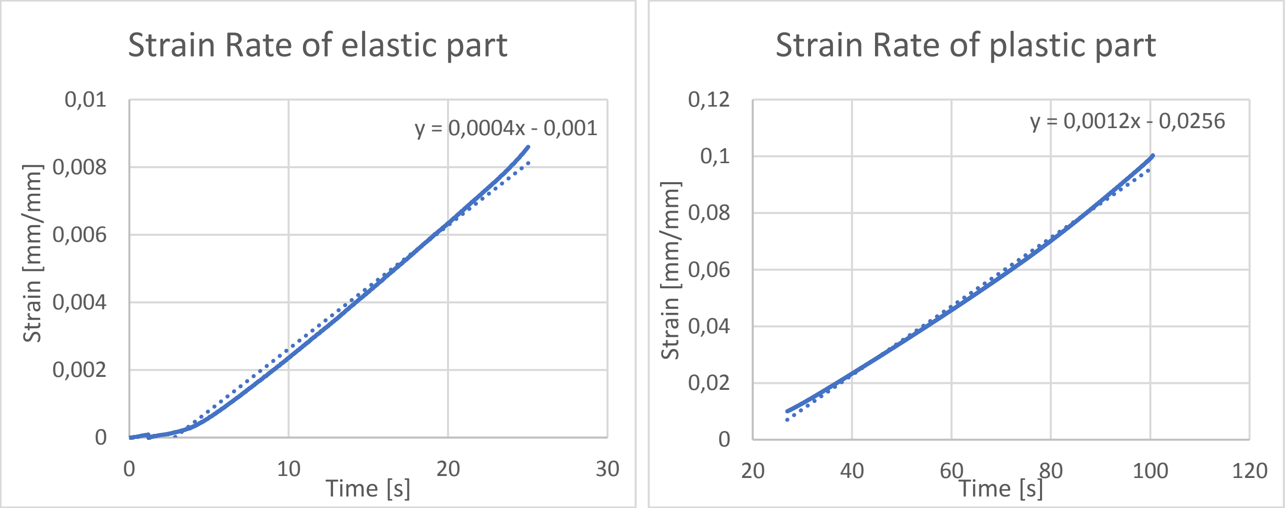

Figure 61: Strain/time plots of the elastic and plastic part, with the regression line (dotted).

Summing up, for a crosshead separation rate of 2 mm/min the calculated strain rates are:

- $4.0 \cdot 10^{-4}$ s^{-1} for the elastic part
- $1.2 \cdot 10^{-3}$ s^{-1} for the plastic part

Assuming that the crosshead separation rate and the strain rate are linearly correlated, to achieve the requested values of strain rate the crosshead separation rate can be calculated as in Eq. 5 – 8.

$$\frac{7.0 \cdot 10^{-5}}{4.0 \cdot 10^{-4}} = \frac{v_{c,el.}}{2} \tag{5}$$

$$v_{c,el.} = 0.35\ \frac{mm}{min} \tag{6}$$

$$\frac{6.7 \cdot 10^{-3}}{1.2 \cdot 10^{-3}} = \frac{v_{c,pl.}}{2} \tag{7}$$

$$v_{c,pl.} = 11.17\ \frac{mm}{min} \tag{8}$$

Where $v_{c,el.}$ and $v_{c,pl.}$ are the crosshead separation rate for the elastic part and for the plastic part, respectively.

A test was carried out with the calculated crosshead speeds and the corresponding plot is shown in Figure 62.

Figure 62: Stress/strain plot of the Ti6Al4V specimen tested using the two crosshead separation speeds

Due to the sharp change of the test speed, an irregular load increment is shown at the moment of the change. However, it does not affect the measure, that remains reliable.
The resulting strain rates are:

- $6 \cdot 10^{-5}$ for the elastic part, instead of $7 \cdot 10^{-5}$
- $6.5 \cdot 10^{-3}$ for the plastic part, instead of $6.7 \cdot 10^{-3}$

These values are within the relative tolerance of the strain rate of ±20%, as stated in the standard, so the crosshead separation speeds selected are correct.

Tensile tests performed on aluminum samples required a constant crosshead separation rate of 0.5 mm/min. This value is consistent with the strain rate suggested by the standard for the elastic part of the curve but too slow for the plastic part.

No tensile tests were performed on maraging steel samples because of logistic issues.

In this work, the results of tensile tests will be presented with the 4 main data:

- Young modulus (E).
- Proof strength ($R_{p0.2}$), the stress at which the plastic extension is equal to a specified percentage of the extensometer gauge length. The 0.2% value has been chosen as the most used value to consider the part in pure plastic deformation.
- Tensile strength (R_m), the stress corresponding to the highest force that the test piece withstands during the test.
- Percentage total extension at fracture (A_t): total extension (elastic + plastic) at the moment of fracture, expressed as a percentage of the extensometer gauge length.

Tests have been performed at room temperature.

2.2.2 Fatigue testing

Fatigue, related to a material, is defined as the weakening of the material caused by cyclic loading that results in progressive and localized structural damage and the growth of cracks [161].

Fatigue test methods involve testing specimens under various stress states, such as uniaxial tension/compression, bending and torsion.
The load cycle is characterized by the amplitude and the mean value of the load, hence by the minimum and maximum loads applied. Figure 63 [162] shows the main variables of a fatigue stress cycle.
The ratio between the minimum and the maximum load applied during the cycle is defined as R.
Depending on the value of R, there can be 2 types of stress cycles:

- $R \geq 0$: Pulsed tension or compression
- $R < 0$: Reversed

The load cycle is repeated continuously until the part fails or a high number of cycles is reached, beyond which the part is considered to withstand an infinite number of cycles at the stress set.

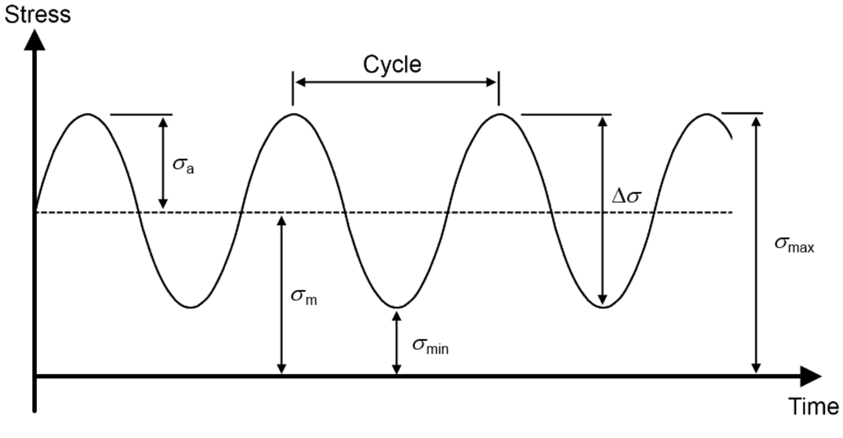

Figure 63: Stress/time plot showing the main parameters of a fatigue cycle. [162]

The most common fatigue tests for material characterization are the uniaxial and the rotating bending tests. In the uniaxial test, a specimen is subject to pure tension/compression stress while in rotating bending, a circular specimen is kept in rotation and a bending moment is applied to the attach units to induce bending at the center of the sample.

The results are then elaborated to obtain plots and values for fatigue strength of the material; the most popular presentation of data for a series of related fatigue tests is the S-N diagram. It is obtained by plotting the number of cycles to failure as the abscissa and the stress range as the ordinate. A logarithmic scale is commonly used for the number of cycles and a linear scale for the stress axis. This diagram is used to estimate the number of cycles that a material can sustain before breaking at a certain stress.

Otherwise, if the aim of the test is to obtain the maximum stress at which a material can withstand to an "infinite" cycle amount, other methods can be used, including the staircase method that will be explained soon.

Generally, fatigue testing of metals is regulated by these standards:

- ISO 1099 Metallic materials — Fatigue testing — Axial force-controlled method
- ISO 1143 Metallic materials — Rotating bar bending fatigue testing
- ISO 12106 Metallic materials — Fatigue testing — Axial-strain-controlled method
- ISO 12107 Metallic materials — Fatigue testing — Statistical planning and analysis of data
- ISO 12108 Metallic materials — Fatigue testing — Fatigue crack growth method
- ASTM E466 - 15 Standard Practice for Conducting Force Controlled Constant Amplitude Axial Fatigue Tests of Metallic Materials
- ASTM E606 - 12 Standard Test Method for Strain-Controlled Fatigue Testing
- ASTM E739 – 10 Standard Practice for Statistical Analysis of Linear or Linearized Stress-Life (S-N) and Strain-Life (ε-N) Fatigue Data

In this work, samples were subject to uniaxial fatigue test. The tests were carried out in compliance with the Staircase method described by the ISO 12107 standard [163].

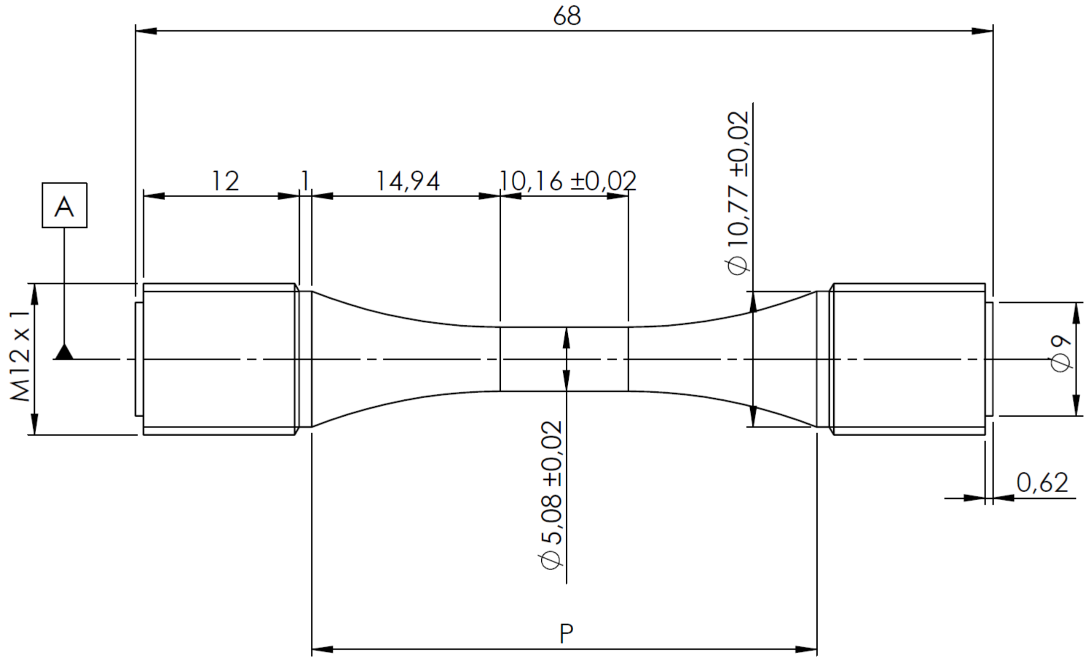

Figure 64: Sample dimensions for uniaxial fatigue tests.

The samples for uniaxial tests were designed according to UNI EN 3987 standard [164] (Figure 64); machined and polished samples required a value of $R_a = 0.2\ \mu m$ in the extent of P.

Fatigue tests were performed on a Rumul Mikrotron with a 20kN load cell. This machine is mainly composed of a mass-spring system, connected to the specimen and to a load cell.
The system oscillates at its natural frequency resulting from the mass and the spring constant; by adding different masses, the natural frequency can be changed, ranging from 68 to 240 Hz.
The tests were performed at 78 - 80 Hz (depending on the geometry and the Young modulus of the material tested). No heat is produced during the test, as confirmed by the IR thermal image (Figure 65).

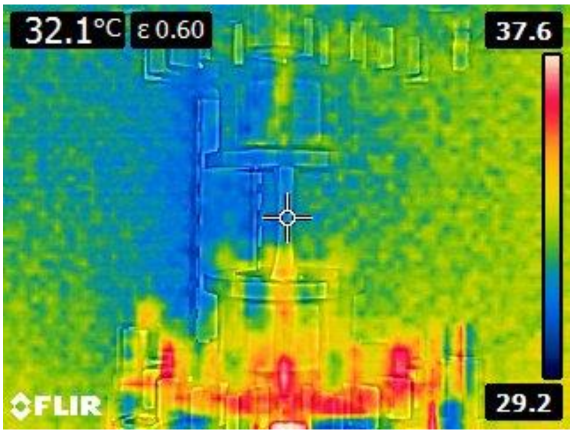

Figure 65: Infrared thermal image of a sample during fatigue testing at 79 Hz. Its temperature is 32.1°C.

The load cycle chosen in the present research is a pure tension with R = 0.01. The runout number of cycles was set to 10^7.

2.2.3 Staircase method

The staircase method was introduced by Dixon and Mood for explosive testing data analysis in 1948 [165]. This test, called "up and down method" can be used for any sensitivity experiment and in general to study events that can show only 2 states, occur or not-occur. It has some important advantages:

- It automatically concentrates testing near the mean, increasing the accuracy with which the mean can be estimated
- Simple statistical analysis

Main disadvantages are:

- Each specimen must be tested separately, waiting for the result of the previous test.
- The method is particularly effective for estimating the mean, but it is not good for small or large percentage points because of the assumption of normal distribution.

Further, some conditions must be satisfied to perform the statistical analysis:

- The variate under analysis must be normally distributed or, it has to be transformed to one which does have the normal distribution.
- The sample size must be large (Dixon and Mood suggest more than 40 samples)
- The standard deviation should be roughly estimated before the test because the interval between testing levels should be less than twice the standard deviation.

The method provides approximate formulas to calculate the mean and standard deviation, assuming that all the mentioned conditions are satisfied.

The staircase method was then applied in the estimation of fatigue life in 1950 by Ransom and Mehl [166] as an abbreviated statistical method to determine the fatigue average endurance limit and standard deviation.

The test procedure is the following: in a series of tests, the stress level at which a specimen is tested, is determined by whether the previous specimen failed or ran unbroken over the runout cycle number. If the specimen fails, the stress on the next test is reduced by one step; otherwise it is increased if the previous specimen survives. [167] The maximum cycle count is assumed to be large enough to reasonably consider that over that cycle number, the specimen would not fail. However, for some materials this limit may not exist.

The full procedure and statistical analysis will be now explained, following the ISO 12107 standard [163].

Some parameters must be chosen before starting the tests:

- First stress level: if the material has not been tested yet, half the maximum stress level measured in tensile test ($R_m/2$) can be considered.
- Stress step: the difference between two stress levels. A step of about 5% of the estimated mean fatigue strength may be used. Further, it should result between 0.5s and 2s (where s = standard deviation) in order to meet the conditions for the applicability of the statistic method.
- Runout cycle number: number of cycles over which we consider infinite life

The method consists in these steps:

1) Test a first specimen, randomly chosen, at the first stress level and find if it fails before the given number of cycles;
2) Test another specimen, also randomly chosen, increasing the stress level by a step if the preceding specimen did not fail, and decreasing the stress by the same amount if it failed.
3) Continue testing until all the specimens have been tested.

Exploratory research requires a minimum of 15 specimens to estimate the mean and the standard deviation of the fatigue strength. Reliability data requires at least 30 specimens.

Then, the test data must be rearranged to count failure and non-failure for every stress step, as shown in Table 11.

Stress		**Tests [Test n° / Specimen ID]**															**Results**	
Stress Level	**Max Stress [MPa]**	**1**	**2**	**3**	**4**	**5**	**6**	**7**	**8**	**9**	**10**	**11**	**12**	**13**	**14**	**15**	**X**	**O**
		F1	F2	F3	F4	F5	F6	F7	F8	F9	F10	F11	F12	F13	F14	F15		
3	140								X		X						2	0
2	130	X						O		O		X				X	3	2
1	120		X		X		O						X		O		3	2
0	110			O		O								O			0	3
																	8	**7**

Table 11: Example of results presentation in staircase fatigue testing.

The statistical analysis then is performed on the group with the lower number of observations (the non-failure in Table 11).

Firstly, the coefficients A, B, C and D ought to be calculated as in equations 9 – 12.

$$A = \sum_{i=0}^{i_{max}} i f_i \tag{9}$$

$$B = \sum_{i=0}^{i_{max}} i^2 f_i \tag{10}$$

$$C = \sum_{i=0}^{i_{max}} f_i \tag{11}$$

$$D = \frac{BC - A^2}{C^2} \tag{12}$$

Where:

- i = stress level. The first stress level must be chosen according to the most frequent event:
    - If most of specimens broke, the event that will be study is the non-failure and the lowest level will be the lowest step at which a specimen survived
    - On the other hand, if most of the specimens survived, the failure event will be studied and the lowest level will be the lowest step at which a specimen failed.
- i_{max} = number of stress levels
- f_i = number of events

Following the example, the results would be as in Table 12.

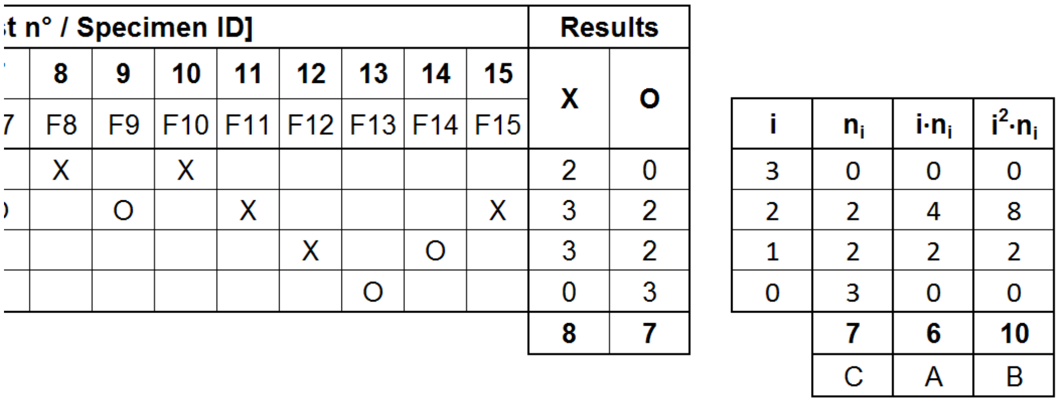

t n° / Specimen ID]								Results	
8	**9**	**10**	**11**	**12**	**13**	**14**	**15**	**X**	**O**
F8	F9	F10	F11	F12	F13	F14	F15		
X		X						2	0
	O		X				X	3	2
				X		O		3	2
					O			0	3
								8	**7**

i	**n_i**	**$i \cdot n_i$**	**$i^2 \cdot n_i$**
3	0	0	0
2	2	4	8
1	2	2	2
0	3	0	0
	7	**6**	**10**
	C	A	B

Table 12: Example of data elaboration in staircase fatigue testing.

After that, it is possible to calculate the mean value as presented in Eq. 13.

$$\hat{\mu}_y = S_0 + d\left(\frac{A}{C} \pm \frac{1}{2}\right) \tag{13}$$

Where:

- d = stress step (e.g. 10 MPa in the example)
- S_0 = stress value of the lowest stress level in which appears the event with smaller number of observations (so the one considered in the statistical analysis). In the example it is 110 MPa.
- The value of ±1/2 is:
    - -1/2 when the event analyzed is failure
    - +1/2 when the event analyzed is non-failure

Meanwhile it is possible to calculate the standard deviation as in Eq. 14 and 15.

$$\hat{\sigma}_y = 1.62d(D + 0.029) \tag{14}$$

The equation is valid only when D > 0.3. If D ≤ 0.3 the following equation should be used:

$$\hat{\sigma}_y = 0.53d \tag{15}$$

If the staircase fatigue test is repeated, the mean and the standard deviation will most likely be different than in previous tests. Therefore, it is necessary to assure with a given confidence that the repeated test values will be above the chosen fatigue limit by using a confidence interval for the sample mean.
If the assumption of a normal distribution of the fatigue strength is correct, the lower limit of the fatigue strength at a probability of failure P can be calculated for the population at a confidence level of $1 - \alpha$ from Eq. 16.

$$\hat{y}_{(P,1-\alpha)} = \hat{\mu}_y - k_{(P,1-\alpha,\nu)}\hat{\sigma}_y \tag{16}$$

Where:

- $k_{(P,1-\alpha,\nu)}$ = one-sided tolerance limit for a normal distribution
- ν = number of degrees of freedom. It corresponds to the number of observations of the less frequent event, minus one.

The values of k are obtained using Table 13.

To calculate these values, a procedure was illustrated by G. Lieberman [168].

Lieberman's procedure states that firstly, a non-central t statistic should be defined, with $n - 1$ degrees of freedom and a non-centrality parameter of $\sqrt{n}K_\alpha$ where K_α is defined by Eq. 17.

$$\frac{1}{\sqrt{2\pi}}\int_{K_\alpha}^{\infty} e^{-z^2}\, dz = \alpha \tag{17}$$

and it can be found from the tables of normal distribution corresponding to a probability α.

The value of t_0 should be determined to satisfy Eq. 18.

$$P\{t_{n-1,\ \sqrt{n}K_\alpha} > t_0\} = 1 - \gamma \tag{18}$$

Where γ is the confidence level.

Actually, the values of t_0 may be obtained by the tables of the distribution of non-central t statistic such as Resnikoff and Lieberman's [169]

Finally, k is obtained by Eq. 19.

$$k = \frac{t_0}{\sqrt{n}} \tag{19}$$

Exhaustive tables can be found in Johnson and Owen work [170] or an approximation can be calculated as described by C. Link et al. [171].

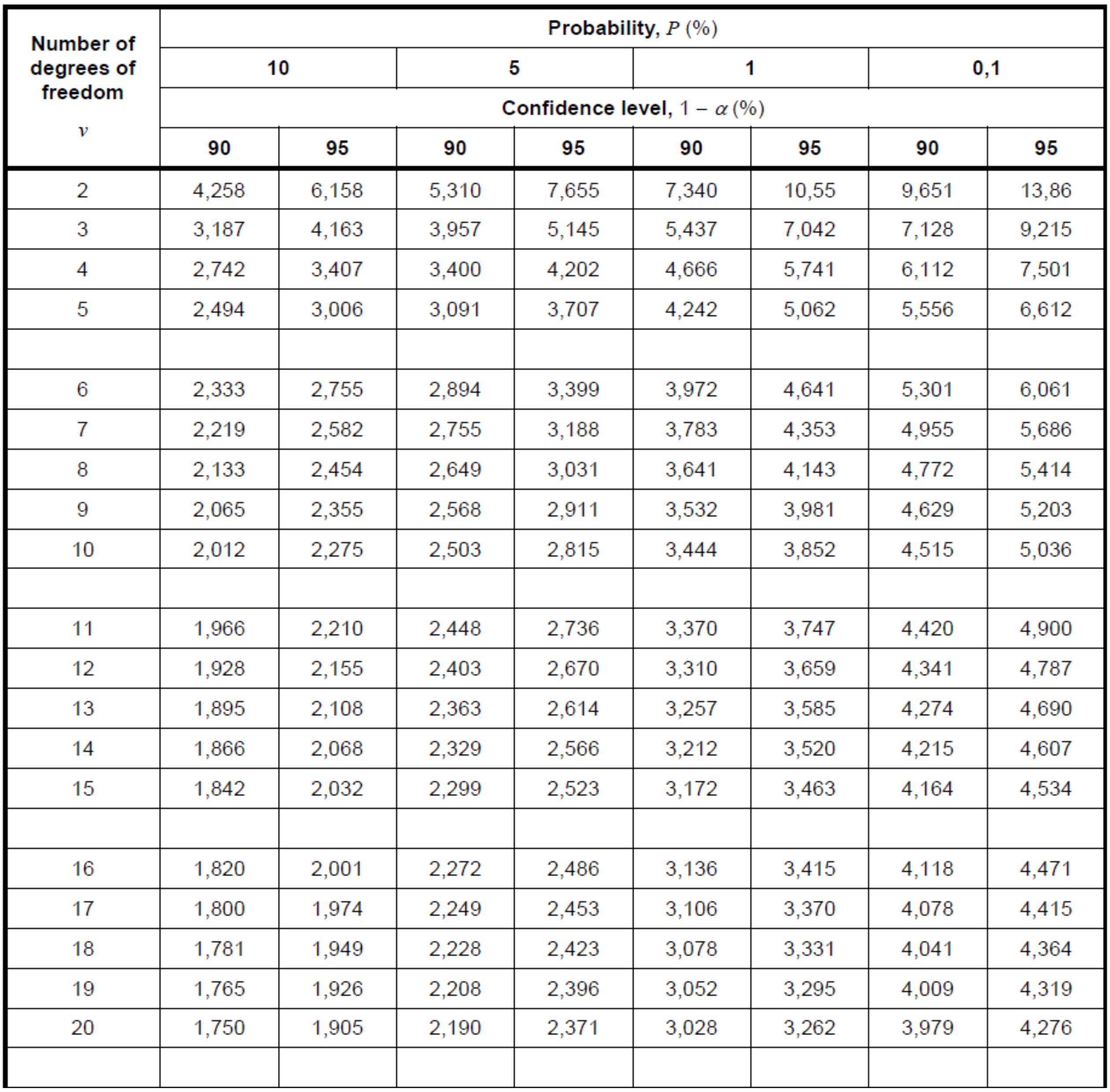

Number of degrees of freedom v	Probability, P (%)							
	10		5		1		0,1	
	Confidence level, $1-\alpha$ (%)							
	90	95	90	95	90	95	90	95
2	4,258	6,158	5,310	7,655	7,340	10,55	9,651	13,86
3	3,187	4,163	3,957	5,145	5,437	7,042	7,128	9,215
4	2,742	3,407	3,400	4,202	4,666	5,741	6,112	7,501
5	2,494	3,006	3,091	3,707	4,242	5,062	5,556	6,612
6	2,333	2,755	2,894	3,399	3,972	4,641	5,301	6,061
7	2,219	2,582	2,755	3,188	3,783	4,353	4,955	5,686
8	2,133	2,454	2,649	3,031	3,641	4,143	4,772	5,414
9	2,065	2,355	2,568	2,911	3,532	3,981	4,629	5,203
10	2,012	2,275	2,503	2,815	3,444	3,852	4,515	5,036
11	1,966	2,210	2,448	2,736	3,370	3,747	4,420	4,900
12	1,928	2,155	2,403	2,670	3,310	3,659	4,341	4,787
13	1,895	2,108	2,363	2,614	3,257	3,585	4,274	4,690
14	1,866	2,068	2,329	2,566	3,212	3,520	4,215	4,607
15	1,842	2,032	2,299	2,523	3,172	3,463	4,164	4,534
16	1,820	2,001	2,272	2,486	3,136	3,415	4,118	4,471
17	1,800	1,974	2,249	2,453	3,106	3,370	4,078	4,415
18	1,781	1,949	2,228	2,423	3,078	3,331	4,041	4,364
19	1,765	1,926	2,208	2,396	3,052	3,295	4,009	4,319
20	1,750	1,905	2,190	2,371	3,028	3,262	3,979	4,276

Table 13: Coefficients for the one-sided tolerance limit for a normal distribution for point P%. [163]

It is important to mention that the reliability of the test results is primarily dependent on the number of specimens tested.

According to the probability of failure that should be investigated (P) and to the confidence level required (1-α), the minimum number of specimens that should be tested (n) can be calculated as in Eq. 20.

$$n = \frac{ln\alpha}{\ln(1-P)} \tag{20}$$

In Table 14 some values are listed.

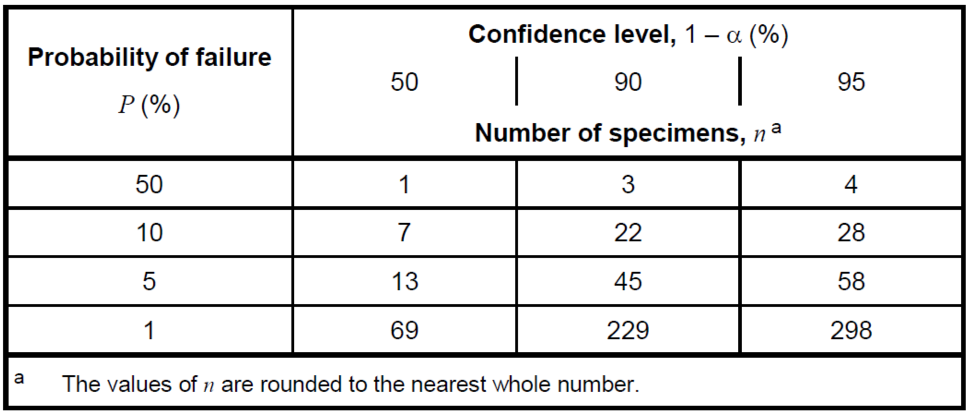

Probability of failure P (%)	Confidence level, $1 - \alpha$ (%)		
	50	90	95
	Number of specimens, n [a]		
50	1	3	4
10	7	22	28
5	13	45	58
1	69	229	298

[a] The values of n are rounded to the nearest whole number.

Table 14: Number of samples required so that the minimum value of test data can be expected to fall below the true value for the population at a given level of probability of failure at various confidence levels. [163]

According to the standard, to estimate the fatigue strength at a given fatigue life, reliable data require at least 30 specimens.

In this work, because of the numerous variables considered, only 15 samples for every condition were produced and tested. The values that will be calculated are the mean value and the standard deviation of the fatigue strength as well as the fatigue strength with P = 10% of failure with a confidence level of 90%. This value is given as an indication, since at least 22 samples would be necessary.

Finally, an example of a practical application of the statistical analysis is showed, starting from Table 15.

Staircase method Example																		
Stress		**Tests**															**Results**	
Stress Level	**Max Stress [MPa]**	**1**	**2**	**3**	**4**	**5**	**6**	**7**	**8**	**9**	**10**	**11**	**12**	**13**	**14**	**15**	**X**	**O**
3	**625**		**X**				**X**						**X**				**3**	**0**
2	**600**	**O**		**X**		**O**		**X**				**O**		**X**		**X**	**4**	**3**
1	**575**				**O**				**X**		**O**				**O**		**1**	**3**
0	**550**									**O**							**0**	**1**
																TOTAL =	**8**	**7**

Table 15: Example of result of staircase fatigue testing.

In this example, the less frequent event is non-rupture, so it will be the analyzed event.

The non-rupture counts are then used to calculate the A, B, C and D parameters:

$$A = \sum_{i=0}^{i_{max}} i f_i = \sum_{i=0}^{3} 0 \cdot 1 + 1 \cdot 3 + 2 \cdot 3 + 3 \cdot 0 = 9$$

$$B = \sum_{i=0}^{i_{max}} i^2 f_i = \sum_{i=0}^{3} 0^2 \cdot 1 + 1^2 \cdot 3 + 2^2 \cdot 3 + 3^2 \cdot 0 = 15$$

$$C = \sum_{i=0}^{i_{max}} f_i = \sum_{i=0}^{3} 1 + 3 + 3 = 7$$

$$D = \frac{BC - A^2}{C^2} = \frac{15 \cdot 7 - 9^2}{7^2} \cong 0.48$$

From the parameters, mean and standard deviation can be easily calculated:

$$\hat{\mu}_y = S_0 + d\left(\frac{A}{C} \pm \frac{1}{2}\right) = 550 + 25\left(\frac{9}{7} + \frac{1}{2}\right) \cong 595\ MPa$$

$$\hat{\sigma}_y = 1.62d(D + 0.029) = 1.62 \cdot 25(0.48 + 0.029) \cong 21\ MPa$$

After that, if we want to state with a confidence level of 0.95 that 90% of the samples will not fail, the parameter $k_{(P,1-\alpha,\nu)}$ will be chosen from the table with P = 10%, $1 - \alpha$ = 95% and ν = 6 so:

$$\hat{y}_{(10,\ 0.95)} = 595 - 2.755 \cdot 21 = 537\ MPa$$

2.2.4 Density measurement: Archimedes' method

Density tests were performed on specimens cut from tensile or fatigue samples. To measure the density, an analytical balance equipped with an Archimedes density kit has been used. The density measurement according to the Archimedes' principle is based on the force generated by an immersed volume (Eq. 21).

$$F_b = \rho_l V g \tag{21}$$

where:

- F_b = upward buoyant force [N]
- ρ_l = density of the liquid [kg/m^3]
- V = volume of the part
- g = gravitational acceleration [9.80665 m/s^2]

The forces applied on an immerse object are schematized in Figure 66 [172]. Eq. 22 shows the force balance result.

$$m_a g - F_b = m_b g \tag{22}$$

where:

- m_a = mass of the part measured in air
- m_b = mass of the part measured in the auxiliary liquid

Eq. 23 is obtained by combining Eq. 21 and Eq. 22. Then m_b is obtained by Eq. 24.

$$m_a g - \rho_l V g = m_b g \tag{23}$$

$$m_a - \rho_l V = m_b \tag{24}$$

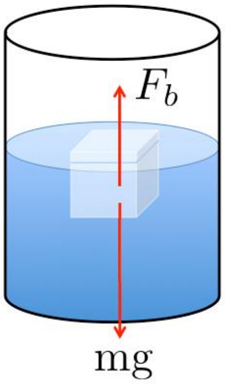

Figure 66: Forces applied to an object immersed in a liquid. [172]

Since the density of a part can be calculated as mass (m) divided by volume (V), the volume of the part can be calculated as in Eq. 25.

$$V = \frac{m_a - m_b}{\rho_l} \tag{25}$$

The density of the part can be finally calculated as in Eq. 26.

$$\rho = \frac{m}{V} = \frac{m_a}{m_a - m_b}\rho_l \tag{26}$$

To include the effects of the air density it is possible to use the Eq. 27.

$$\rho = \frac{m_a}{m_a - m_b}(\rho_l - \rho_{air}) + \rho_{air} \tag{27}$$

where ρ_{air} = 0.0012 g/cm^3

Finally, to obtain accurate results, it is recommended to include the effect of the temperature.
Solids are generally insensitive to temperature fluctuations and therefore the corresponding density changes do not have relevant consequence. However, the density of liquids is more sensitive to temperature changes (order of magnitude of 0.1 to 1% per °C) so the auxiliary liquid density variations with temperature must be considered.

Using distilled water as auxiliary liquid, the relation between density and temperature is expressed by eq. 30 [173] that estimates the function in Figure 67 [174].

$$\rho_l = \rho_{distilled\ water} = 1000\left[1 - \frac{T + 288.9414}{508929.2(T + 68.12963)}(T - 3.9863)^2\right] \tag{30}$$

The density was calculated taking into account the air density and the variation of the water density with the temperature.

To obtain the best results, cubes should be perfectly cleaned up with acetone or other solvents and dried. Finally, it is necessary to make sure that there are no bubbles under the plate and under the part. The uncertainty of the measure can be considered 0.1mg as the repeatability declared in the datasheet of the analytical balance.

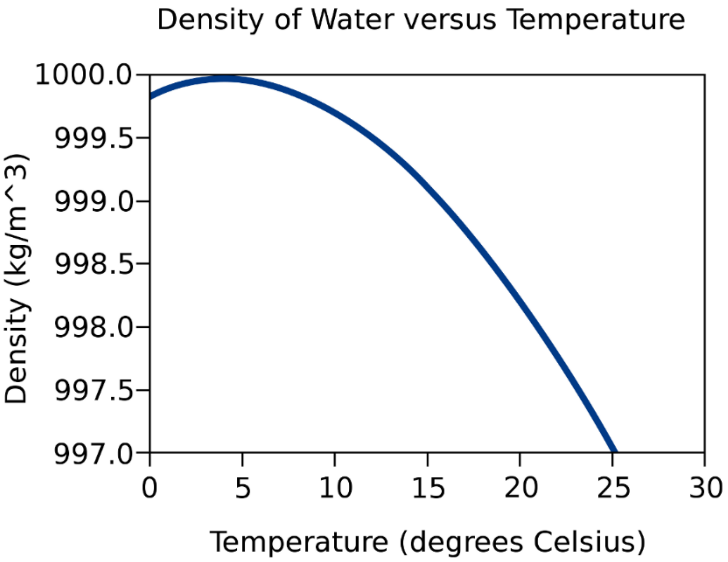

Figure 67: Water density vs temperature plot. [174]

2.2.5 Roughness measurement and confocal microscopy

The surface texture of mechanical components is an important characteristic that influences aspects such as fatigue properties, friction, positional accuracy, aesthetic appearance and surface cleanability (particularly critical in food processing industry) of a component.

The surface topology is the result of manufacturing technology of the component, surface treatments and external degradation phenomena.

Surface topology can be investigated through the acquisition of one or more profiles of the surface.

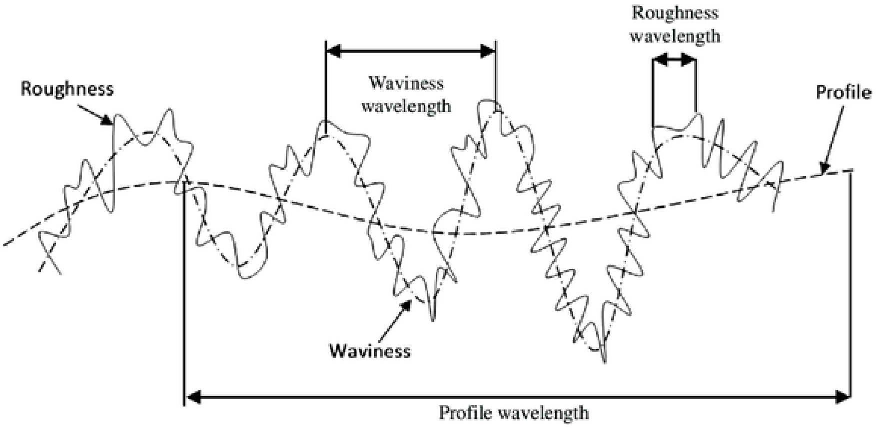

Figure 68: Explanation of the main components of a surface profile. [176]

According ISO 4287 [175], the surface profile is composed of 3 main components, according to their wavelength:

- Primary profile: direction of the predominant surface pattern (the shape of the part), it is usually visible to naked eye. It is described by the P-parameters.
- Roughness profile: considered the high-frequency, short-wavelength component of the measured surface. It is derived from primary profile by suppressing the longwave component using the profile filter λ_c defined in the ISO 4287 standard. The parameters related to roughness are the R-parameters.

- Waviness profile: defined as irregularities whose spacing is greater than the roughness sampling length. The parameters calculated from the waviness profile are the W-parameters.

Figure 68 [176] shows an explanation of the 3 components mentioned.

The profile parameters can be calculated on the whole profile (evaluation length) or on sampling lengths and then averaged. As exemplified in Figure 69, sampling length is usually defined as the cut-off length (λ_c) of the filter used to separate roughness and waviness.

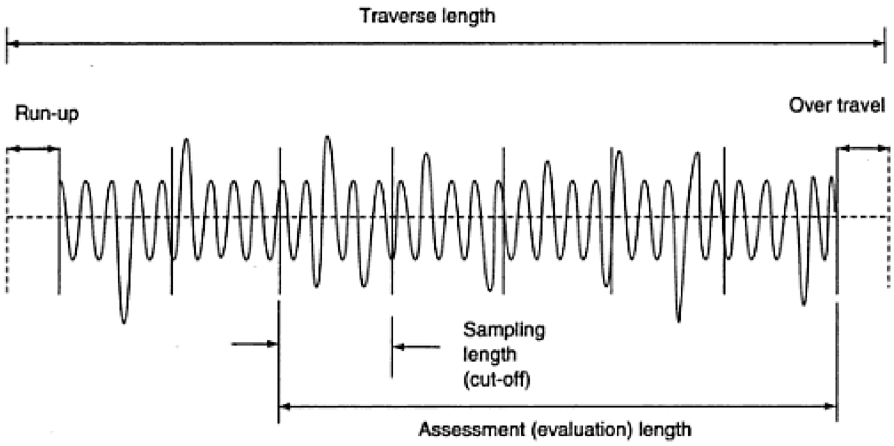

Figure 69: Sampling length and evaluation length of a measured profile. [176]

The definitions of the parameters are the same for primary, roughness and waviness profiles. As to the roughness profile, the following definitions apply [177]:

- Maximum profile peak height (R_p): maximum height of the profile above the mean line within a sampling length.
- Maximum profile valley depth (R_v): maximum depth of the profile below the mean line, within a sampling length.
- Maximum height of profile (R_z): sum of the height of the largest profile peak height and the largest profile valley depth within a sampling length. This parameter is frequently used to check whether the profile has protruding peaks that might affect static or sliding contact function.
- Total height of profile (R_t, R_{max}): vertical distance between the highest peak and the lowest valley along the assessment length of the profile.
- Arithmetic Average Height (R_a): average absolute deviation of the roughness irregularities from the mean line over one sampling length. It is the most used roughness parameter for general surface quality control.

  It is represented by the mean line in the roughness plot (Figure 70) and it is calculated as in Eq. 31.

$$R_a = \frac{1}{l}\int_0^l |y(x)|dx \tag{31}$$

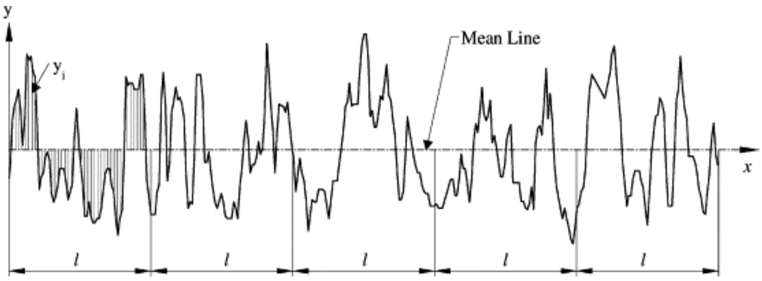

Figure 70: Ra representation. [177]

- Root mean square roughness (R_q): it represents the standard deviation of the distribution of surface heights. It is calculated as in Eq. 32.

$$R_q = \sqrt{\frac{1}{l}\int_0^l y^2(x)dx} \tag{32}$$

  This parameter is more sensitive to large deviation from the mean line represented by R_a.
- Skewness (R_{sk}): it is the third central moment of th profile amplitude probability density function, measured over the assessment length (Figure 71). It is used to measure the symmetry of the profile about the mean line. It is calculated as in Eq. 33.

$$R_{sk} = \frac{1}{{R_q}^3}\left[\frac{1}{l_r}\int_0^{l_r} y^3(x)dx\right] \tag{33}$$

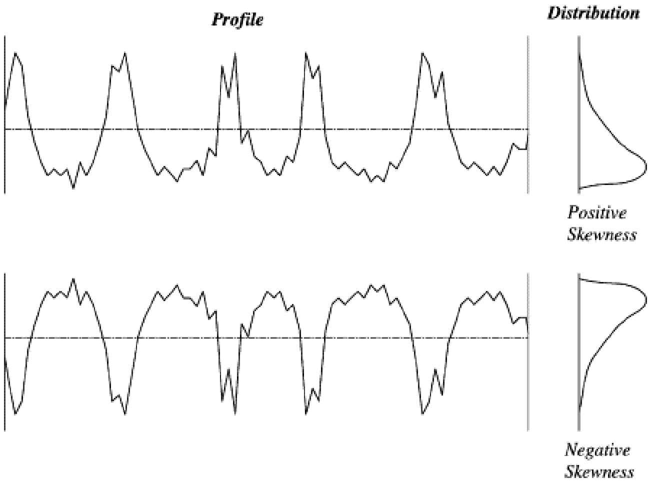

Figure 71: Skewness explanation. [177]

- Kurtosis (R_{ku}): fourth central moment of the profile amplitude probability density function, measured over the assessment length (Figure 72). It describes the sharpness of the profile. It is calculated as in Eq. 34.

$$R_{ku} = \frac{1}{{R_q}^4}\left[\frac{1}{l_r}\int_0^{l_r} y^4(x)dx\right] \tag{34}$$

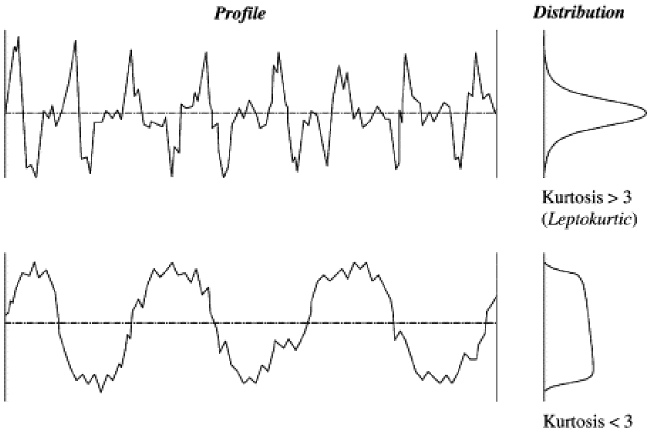

Figure 72: Kurtosis explanation. [177]

The measure of different surface profile is considered a reliable method for quality assurance. However, in order to obtain data of an entire surface, it is necessary to use 3D scanning methods. In this case, the meaning of the profile parameters mentioned before is maintained and the calculations are often an extension to a surface of the profile expressions. For example, S_a is the analogous of R_a measured on an entire area "A" and it is defined in the ISO 25178-2 [178] as in Eq. 35.

$$S_a = \frac{1}{A}\iint_A |Z(x,y)|dxdy \tag{35}$$

In spite of the correlation between 2D and 3D surface parameters, some significant differences exist [179], so that specific standards are available for 3D surface texture characterization, especially all the ISO 25178 standards on areal analysis and the ISO 16610 standards for data filtering.

For example, while for a line profile Pa, Ra and Wa can be calculated, for surfaces, Sa is the only parameter, which can therefore be a parameter of roughness or waviness, depending on the pre-filtering that is applied before the parameter is calculated. This decision is based upon the multiplicity of processing and filtering methods that are available for extracting information from a surface. These processing methods do not necessarily separate the surface texture into two components that are roughness and waviness but in certain cases they alter the surface in a more subtle manner, for example by correcting errors in the acquired data [179].

Confocal Microscopy, or Confocal Laser Scanning Microscopy (CLSM), is an optical imaging technique that obtains images of a small area by means of a laser beam.

By capturing multiple two-dimensional images at different depths in a sample, a three-dimensional structure is re-constructed, generally in a form of a point cloud [180]. On the point cloud, different analyses can be performed such as roughness evaluation, measurement of a hole, calculation of the wear volume in tribology tests.

This instrument allows to measure the topological parameters of a surface rather than only a line, as typically done with roughness meters. This leads to a more reliable and representative surface characterization.

In this work, a Nikon LV150 optical microscope, equipped with a confocal head has been used to acquire and characterize the surface texture of fatigue samples. An area of 0.5 mm x 1.5 mm was acquired on the samples, with a Z (vertical) resolution of 0.2 μm.

The acquired point cloud was elaborated with the software Mountains Map (by DigitalSurf) by applying the following filters, according to ISO 16610:

1) Shape removal: the cylindrical shape of the sample is removed from the analysis
2) Micro-roughness filtering: a standard Gauss filter is applied with a cut-off of 8 μm to filter the micro-roughness
3) Bilateral symmetric threshold filtering: to remove spikes

This filtering method was applied to remove the main shape of the surface and the micro-roughness, leaving a mixture of roughness and waviness components.

The Surface parameters were calculated according to ISO 25178: S_q, S_{sk}, S_{ku}, S_p, S_v, S_z, S_a.

3. Results and discussion

In the next chapters, the results of tensile and fatigue tests performed on the 3 materials will be presented. Tensile tests results will be shown first, then fatigue testing results will be presented as follows: the results of staircase fatigue tests are summed up in tables where the sample ID and the corresponding stress levels are indicated; the result of every test is described by an “X” if the sample fails or a “O” if the sample reaches the runout cycle number. In case of fail, the number of cycles is indicated.
In the title of the tables the following data are specified, depending on the variables considered for a specific material: Material – Building orientation – Process package – Contamination – Surface condition – Heat treatment – Batch number.
Every table is followed by the SEM images of the fracture surfaces of early broken sample and medium sample (as described before), in particular the crack initiation defect is shown.

3.1 AlSi7Mg alloy

Table 16 sums up the test plan for the AlSi7Mg alloy. Further, other tests were performed on the tensile and fatigue samples to acquire other information such as surface roughness and microstructural characteristics.

AlSi7Mg Test Variables			
Test	**Orientation**	**Heat Treatment**	**Surface**
Tensile	XY	T6	As-built
	Z	T6	As-built
Fatigue	XY	As-built	Mach. + Pol.
	Z	As-built	Mach. + Pol.
	XY	T6	Mach. + Pol.
	Z	T6	Mach. + Pol.
	Z	T6	As-built
	Z	T6 + ATV	As-built

Table 16: AlSi7Mg test plan presenting the variables considered.

3.1.1 Tensile tests results

In Table 17 are reported the detailed results of the tensile tests performed on the aluminum samples. As described in Table 16, these samples were shot peened and they were subjected to T6 heat treatment.

The tensile properties found in this work are consistent with those found in literature [101,106,108,181].

As can be seen in Figure 73, the tensile properties are not significantly different for the two building orientations, except for the elongation at fracture that is considerably higher for XY samples. This behavior is confirmed in the literature cited before [101,106,108]. Despite the more homogeneous microstructure generated by the T6 heat treatment (as can be seen in Figure 82), slightly higher performance is recorded for XY samples as compared to Z samples. This is due to the slightly retained anisotropy in the Mg-Si particles distribution even after ageing treatment. Increasing the treatment time is expected to reduce anisotropy as a result of a more even distribution of the Mg-Si particles. Nonetheless, treating for a longer time is also expected to increase the particle size, hence reducing ductility [101].

Sample ID	Orientation	E [GPa]	$R_{p\,0.2}$ [MPa]	R_m [MPa]	A_t [%]
1V	Z	65	245	274	1.9
2V	Z	64	251	287	2.6
3V	Z	65	252	294	3.6
4V	Z	63	251	280	1.9
1H	XY	65	250	301	4.4
2H	XY	65	253	303	4.1
3H	XY	65	254	303	4.4
4H	XY	61	250	310	5.5

Table 17: AlSi7Mg tensile tests results.

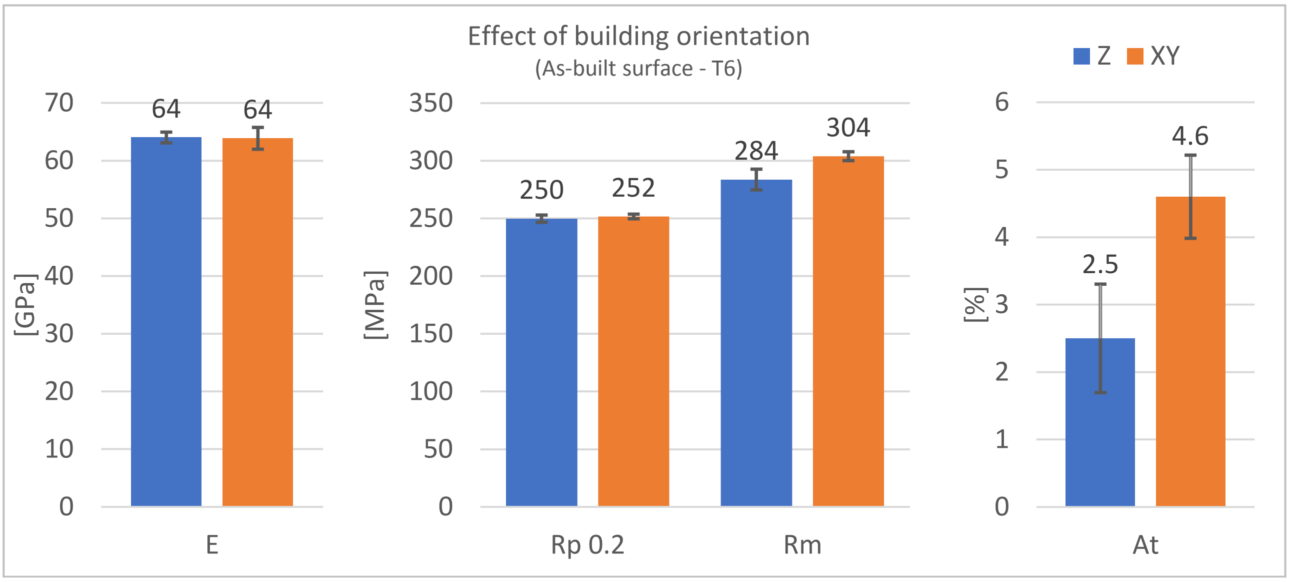

Figure 73: Comparison plot of AlSi7Mg tensile properties.

3.1.2 Fatigue tests results

Firstly, the results of surface texture analysis on fatigue samples are discussed. The roughness characteristics of a randomly chosen polished sample and another randomly chosen as-built sample are summed up in Table 18.

ISO 25178 Surface GPS		
Param.	**Polished**	**As-built**
S_q	0.307 μm	22 μm
S_{sk}	-0.003	1.09
S_{ku}	2.74	5.56
S_p	0.735 μm	92.7 μm
S_v	0.733 μm	51.8 μm
S_z	1.47 μm	145.0 μm
S_a	0.246 μm	16.0 μm

Table 18: Roughness parameters of polished and as-built samples

The value of S_a for as-built samples is comparable with the value in the datasheet of AlSi10Mg of EOS [182]. Then the value of S_a of the polished sample is within a good tolerance with the target value of 0.2 μm. Figure 74 shows the 3D maps acquired with the confocal microscope for the surface analysis.

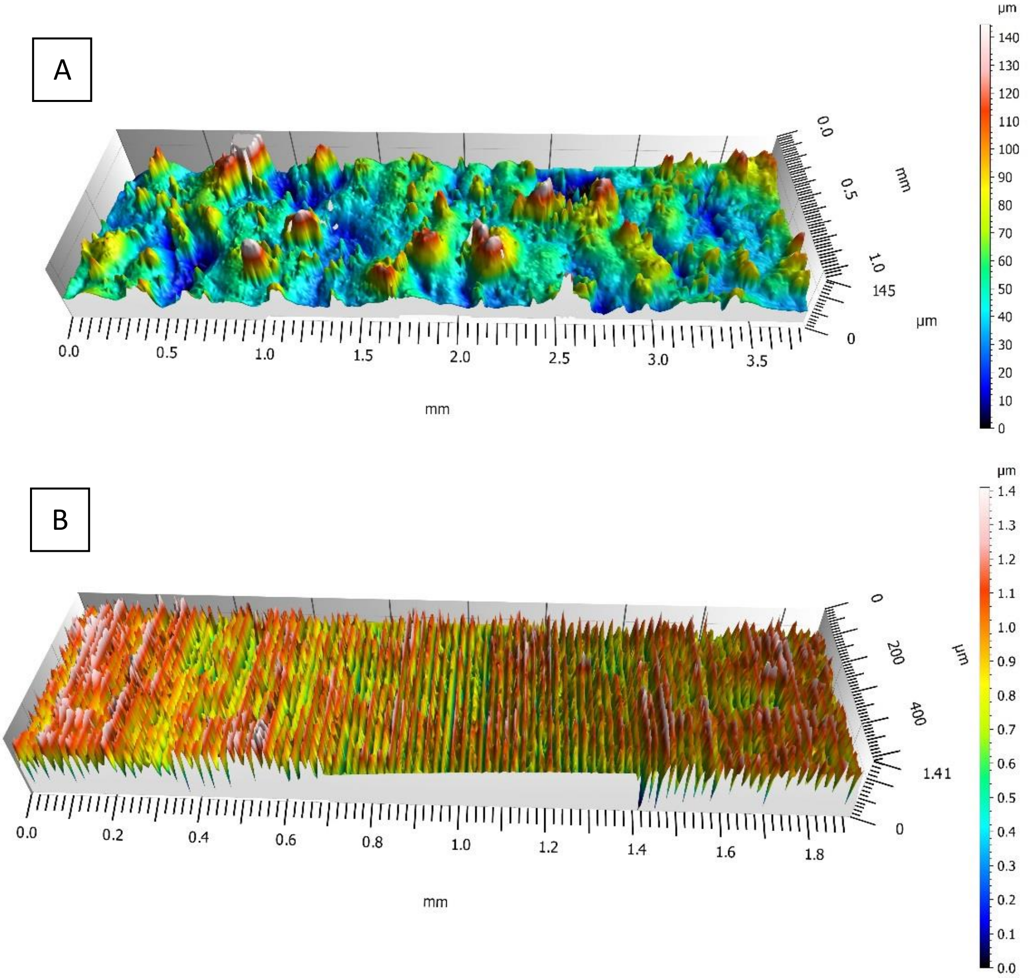

Figure 74: 3D acquisition of (A) as-built and (B) polished AlSi7Mg samples surface. Note the scalebar values.

The results of the fatigue tests managed with the staircase method are shown in the tables 19 – 24.
In the title of the tables the following data are indicated: Material – Building orientation – Surface condition – Heat treatment – Batch number.
Every table is followed by the SEM images of the fracture surface of early broken samples and medium samples (samples with an average behavior in term of fatigue performance).

AlSi7Mg - Z - Machined and polished – As-built – 010																		
Stress		**Tests [Test n° / Specimen ID / Cycles to rupture]**															**Results**	
Stress Level	**Max Stress [MPa]**	**1**	**2**	**3**	**4**	**5**	**6**	**7**	**8**	**9**	**10**	**11**	**12**	**13**	**14**	**15**	**X**	**O**
		F1	F2	F3	F4	F5	F6	F7	F8	F9	F10	F11	F12	F13	F14	F15		
		2.82 E+05	6.59 E+05	1.00 E+07	1.00 E+07	3.01 E+05	8.63 E+05	4.55 E+05	1.00 E+07	1.00 E+07	2.46 E+05	9.09 E+05	1.00 E+07	1.41 E+06	1.00 E+07	5.92 E+05		
3	140	X				X											2	0
2	130		X		O		X				X						3	1
1	120			O				X		O		X		X		X	4	2
0	110								O				O		O		0	3
																	9	**6**

Table 19: Staircase fatigue results for AlSi7Mg samples. Build and treatment details are given in the title of the table.

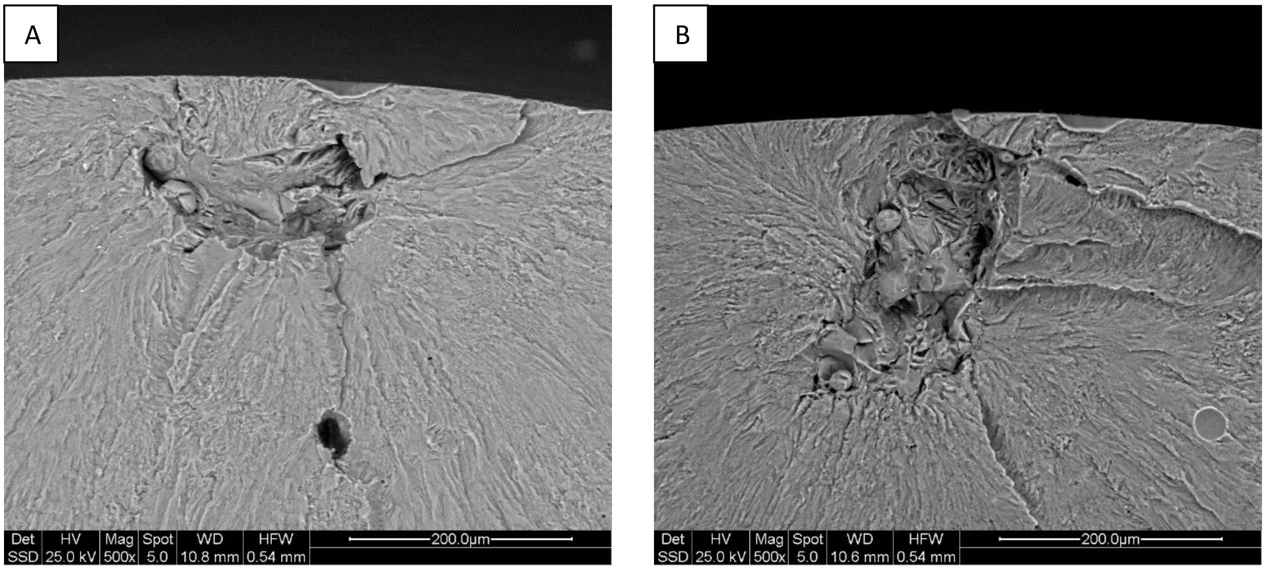

Figure 75: SEM images of crack initiation defects of samples: F6 - Medium (A) and F7 - Early (B)

In Figure 75, the crack initiation defects can be seen. They are typical lack of fusions (LOF) as described by Zhang et al. [85], characterized by partially unfused area, often accompanied with unfused powder particles. They can result mainly due to lack of energy input during the process or due to oxidation caused by the residual oxygen always present in the building chamber (generally about 0.1%). These defects can occur randomly in a cross-section of the part. However, as exemplified in Figure 75, in the present samples the LOFs acting as triggering defects always appear on the surface of the sample. This aspect is not correlated to some sort of laser contour scan strategy because the contour was removed during the machining operations to obtain the correct sample geometry. The positioning on the surface is due to the fact that when this kind of defect happens to be located on the surface of the part or just under the surface, it acts as stress concentration spot, resulting almost always as the start of the crack, therefore they can be seen on the fracture surface. This behavior is common to all the defects found on the fracture surface observed in this work.

AlSi7Mg - XY - Machined and polished – As-built – 020																		
Stress		**Tests [Test n° / Specimen ID / Cycles to rupture]**															**Results**	
Stress Level	**Max Stress [MPa]**	**1**	**2**	**3**	**4**	**5**	**6**	**7**	**8**	**9**	**10**	**11**	**12**	**13**	**14**	**15**	**X**	**O**
		912	972	932	992	952	982	913	973	933	993	911	983	951	981	953		
		5.03 E+05	1.00 E+07	1.00 E+07	4.97 E+05	7.74 E+05	1.00 E+07	1.19 E+06	1.00 E+07	1.22 E+06	1.00 E+07	3.43 E+05	4.09 E+06	1.00 E+07	1.00 E+07	1.00 E+07		
3	150				X												1	0
2	140	X		O		X		X		X		X				O	5	2
1	130		O				O		O		O		X		O		1	5
0	120													O			0	1
																	7	**8**

Table 20: Staircase fatigue results for AlSi7Mg samples. Build and treatment details are given in the title of the table.

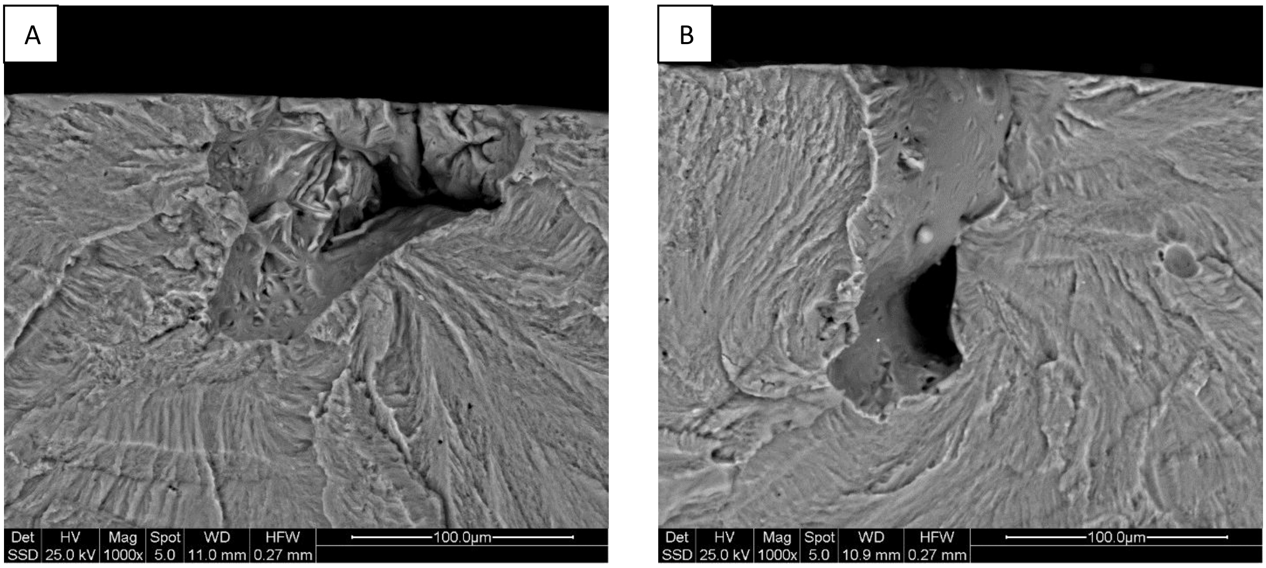

Figure 76: SEM images of crack initiation defects of samples: 933 - Medium (A) and 983 - Early (B)

Figure 76 shows other sub-superficial defects. In the medium sample, the critical defect is a LOF with an approximate dimension of 100 μm with an irregular internal surface. Some areas where unfused particles were attached can be seen. The early sample on the other hand, shows a defect with a more regular and smooth surface. In this case, the reason for the defect generation could be the expansion of a gas bubble, as discussed by Zhang et al. [85]. The oxidized surface induces lower wetting capability hence poor adhesion with the molten metal around the defect.

Figure 77 shows the fracture surfaces of samples subjected to T6 heat treatment. Small but numerous pores can be seen, unlike as-built samples. These pores are generated by the T6 heat treatment (the explanation of this phenomenon will be given in page 88). Medium sample shows a small defect (20 μm approximately) while early sample shows a 200 μm irregular LOF with a possible oxidation of the surface of the defect.

AlSi7Mg - Z - Machined and polished – T6 – 030																		
Stress		**Tests [Test n° / Specimen ID / Cycles to rupture]**															**Results**	
Stress Level	**Max Stress [MPa]**	**1**	**2**	**3**	**4**	**5**	**6**	**7**	**8**	**9**	**10**	**11**	**12**	**13**	**14**	**15**	**X**	**O**
		F1	F2	F3	F4	F5	F6	F7	F8	F9	F10	F11	F12	F13	F14	F15		
		2.31 E+05	4.43 E+05	1.00 E+07	1.20 E+06	1.00 E+07	1.00 E+07	1.00 E+07	9.70 E+05	1.00 E+07	4.29 E+05	5.68 E+05	7.67 E+05	1.00 E+07	1.00 E+07	6.61 E+05		
3	140								X		X						2	0
2	130	X						O		O		X				X	3	2
1	120		X		X		O						X		O		3	2
0	110			O		O								O			0	3
																	8	**7**

Table 21: Staircase fatigue results for AlSi7Mg samples. Build and treatment details are given in the title of the table.

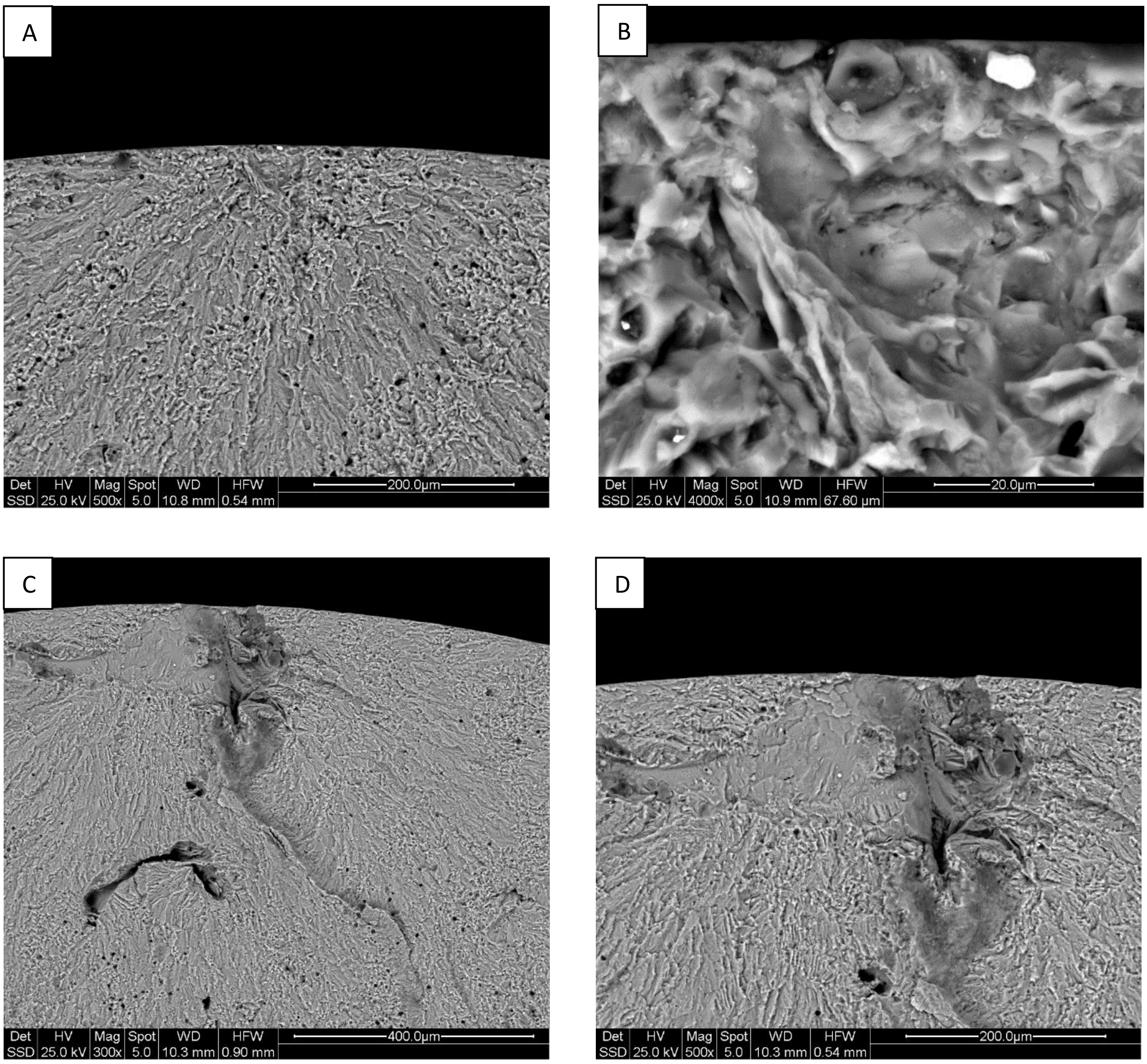

Figure 77: SEM images of crack initiation defects of samples: F15 - Medium (A and B) and F2 - Early (C and D). The bright spot in figure A and B is a dirt particle due to incomplete cleaning of the surface.

AlSi7Mg - XY - Machined and polished – T6 – 040

Stress		Tests [Test n° / Specimen ID / Cycles to rupture]															Results	
Stress Level	Max Stress [MPa]	1	2	3	4	5	6	7	8	9	10	11	12	13	14	15	X	O
		922	923	911	971	931	991	951	981	912	972	932	992	952	982	913		
		1.00 E+07	7.13 E+05	2.07 E+06	1.00 E+07	1.00 E+07	3.42 E+06	1.00 E+07	1.00 E+07	7.56 E+05	4.29 E+05	1.00 E+07	1.00 E+07	5.11 E+05	3.21 E+06	1.01 E+06		
3	140									X				X			2	0
2	130		X				X		O		X		O		X		4	2
1	120	O		X		O		O				O				X	2	4
0	110				O												0	1
																	8	**7**

Table 22: Staircase fatigue results for AlSi7Mg samples. Build and treatment details are given in the title of the table.

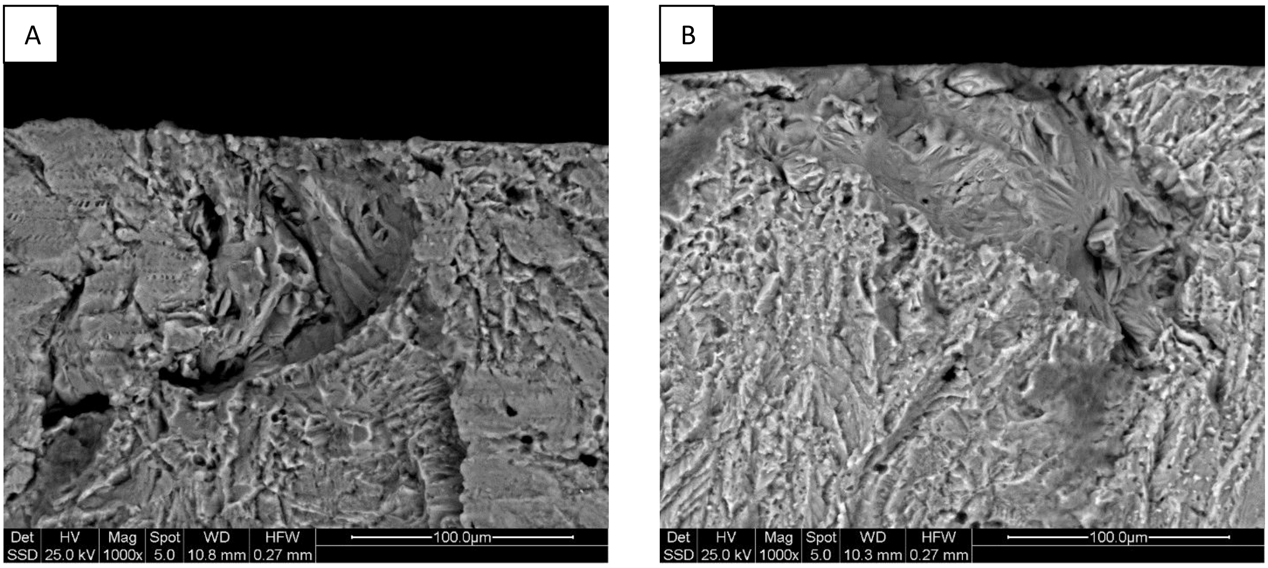

Figure 78: SEM images of crack initiation defects of samples: 991 - Medium (A) and 913 - Early (B)

Samples built in XY direction and heat-treated show relatively small critical defects, with an irregular surface (Figure 78).

AlSi7Mg - Z – As-built – T6 + ATV – 050

Stress		Tests [Test n° / Specimen ID / Cycles to rupture]															Results	
Stress Level	Max Stress [MPa]	1	2	3	4	5	6	7	8	9	10	11	12	13	14	15	X	O
		4	10	12	6	1	14	5	11	8	2	13	9	16	3	15		
		5.93 E+06	1.00 E+07	7.49 E+05	5.83 E+06	1.00 E+07	1.00 E+07	9.55 E+05	1.00 E+07	1.00 E+07	1.37 E+06	9.11 E+06	1.00 E+07	1.11 E+06	1.00 E+07	1.00 E+07		
3	110										X						1	0
2	100	X		X				X		O		X		X		O	5	2
1	90		O		X		O		O				O		O		1	5
0	80					O											0	1
																	7	**8**

Table 23: Staircase fatigue results for AlSi7Mg samples. Build and treatment details are given in the title of the table.

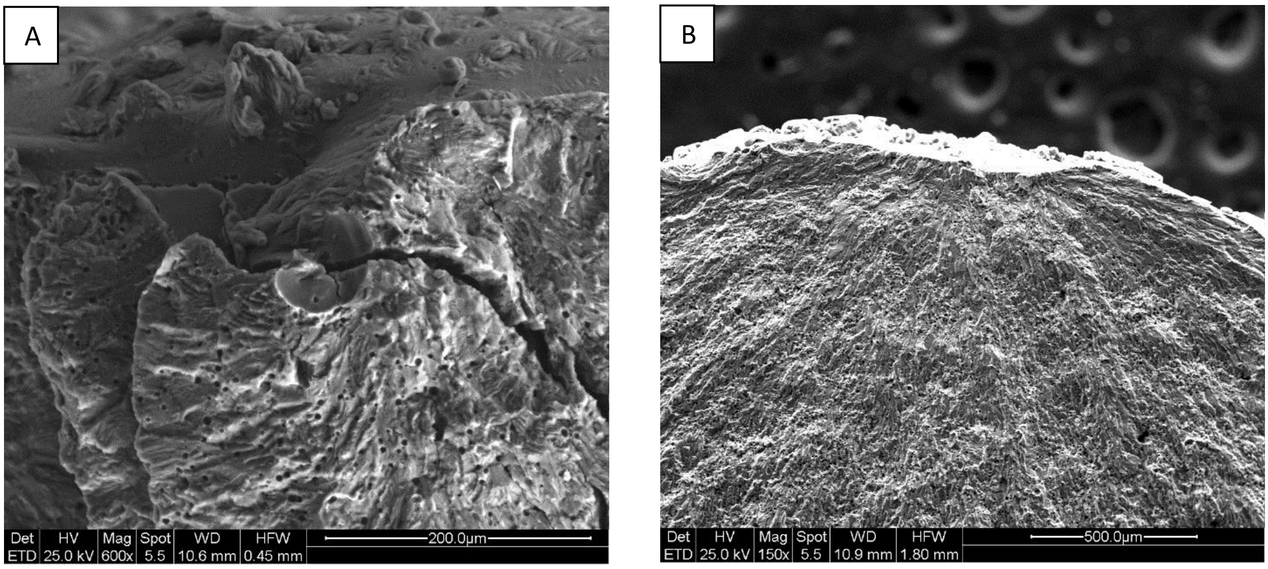

Figure 79: SEM images of crack initiation defects of samples: 4 - Medium (A) and 12 - Early (B)

In this case, the surface of the samples has not been machined and it is therefore in the as-built condition. Figure 79-A shows the starting point of a big crack on the surface of the medium sample. Thus, the behavior of as-built samples is heavily affected by the topology and the consistency of their surface, as expected and as confirmed by the following results.

The early sample does not show an evident defect on the fracture surface; however, the fracture surface texture indicates that the crack starting defect is located on the surface of the sample.

AlSi7Mg - Z – As-built – T6 – 060																		
Stress		**Tests [Test n° / Specimen ID / Cycles to rupture]**															**Results**	
Stress Level	**Max Stress [MPa]**	**1**	**2**	**3**	**4**	**5**	**6**	**7**	**8**	**9**	**10**	**11**	**12**	**13**	**14**	**15**	**X**	**O**
		21	17	27	18	28	19	32	25	29	22	26	31	20	24	23		
		2.03 E+06	1.00 E+07	1.97 E+06	7.76 E+05	1.00 E+07	1.00 E+07	4.88 E+05	1.00 E+07	1.32 E+06	1.91 E+06	1.00 E+07	1.00 E+07	1.79 E+06	1.00 E+07	1.65 E+06		
2	110	X		X				X		X				X		X	6	0
1	100		O		X		O		O		X		O		O		2	5
0	90					O						O					0	2
																	8	**7**

Table 24: Staircase fatigue results for AlSi7Mg samples. Build and treatment details are given in the title of the table.

Figure 80 shows the crack initiation defects of heat-treated samples, with as-built surface. Porosities generated by the T6 heat treatment are clearly visible in Figure 80-B. The defects, both for early and medium samples, are generated on the surface of the sample, probably due to an issue in the consolidation of the contour or due to oxidation phenomena.

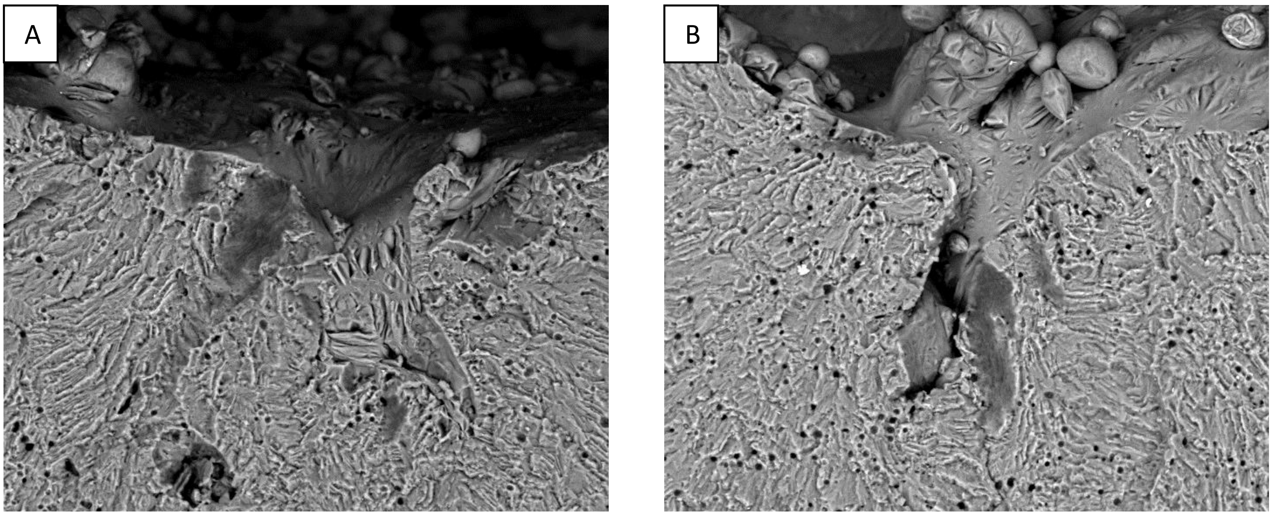

Figure 80: SEM images of crack initiation defects of samples: 21 - Medium (A) and 32 - Early (B)

The results of the fatigue tests were used to calculate the fatigue strength of the material in terms of mean value and standard deviation. Further the fatigue strength at a 90% level of confidence, for a 10% probability of failure, was calculated.

The results are summed up in Table 25:

Heat Treatment	Orientation	Surface finish	Fatigue strength [MPa]		
			Mean	Std Dev	10% / 0.90
As-built	Z	Machined and polished	122	10	98
As-built	XY	Machined and polished	135	5	123
T6	Z	Machined and polished	124	12	96
T6	XY	Machined and polished	126	7	110
Pre-ATV (only T6)	Z	As-built	102	5	90
Post-ATV (T6 + ATV)	Z	As-built	95	5	83

Table 25: Fatigue strength data of AlSi7Mg with respect to different heat treatments, orientation and surface finish.

Firstly, the effects of the building orientation and of the heat treatment are evaluated, in terms of mean value of the fatigue strength (Figure 81).

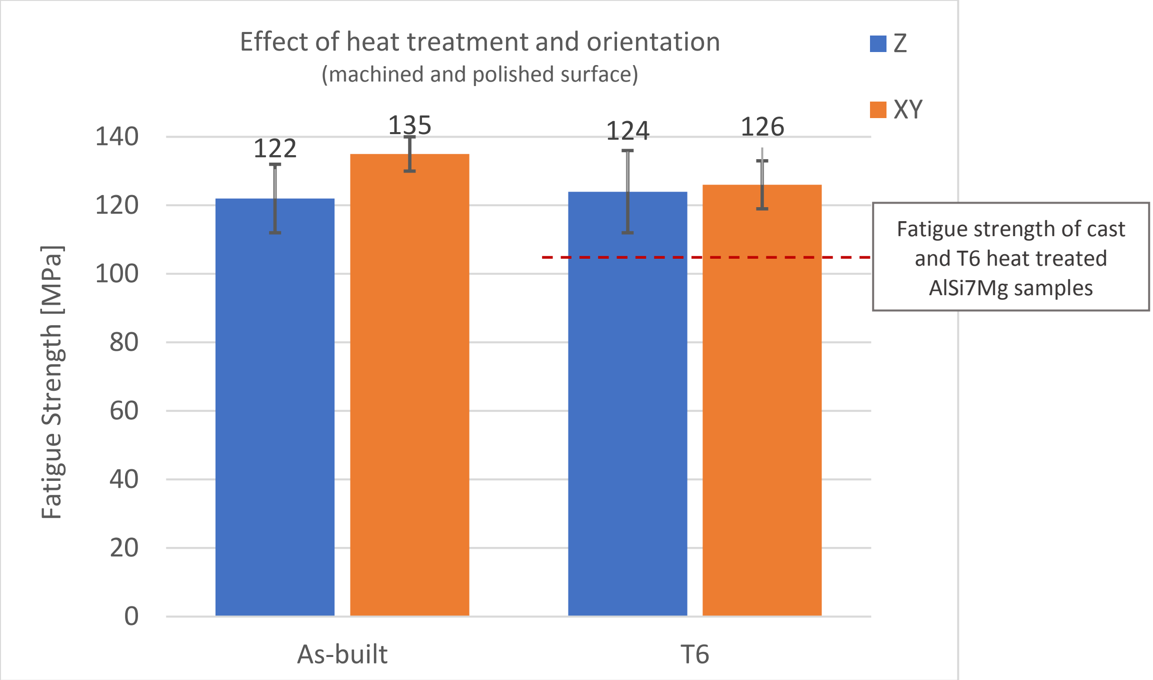

Figure 81: Fatigue strength comparison plot between XY and Z orientations and heat treatment conditions. The value of fatigue strength of cast samples was acquired by other tests performed in the very same conditions. Cast samples were T6 heat treated.

Prior to the evaluation of the effects of heat treatment and orientation, the comparison between cast and L-PBF parts can be noted: as can be seen in the plot in Figure 81, the fatigue strength of L-PBF parts is higher than that of cast parts, for all the considered conditions. In particular, after T6 treatment, L-PBF samples show significantly higher fatigue strength (+19%), as compared to cast samples.

The effect of the orientation (so material anisotropy) is more accentuated for the as-built samples while the T6 treated samples seem to be less affected. This behavior can be explained by the optical microscope images (Figure 82): cross-sections of melt pools can be seen in the micrograph parallel to the building direction as overlapping semi-circles (Figure 82-B). They are all partly inter-connected, which ensures perfect bonding between adjacent layers. On the contrary, long laser scan tracks can be distinguished in the micrograph parallel to the build platform (Figure 82-A). Overlapped scan tracks are differently oriented as a result of the specific core scanning strategy used to build the samples [181]. All these features indicate an anisotropy of the material.

After the T6 heat treatment (Figure 82-C and D), scan lines are no more visible. A homogeneous microstructure is shown in both the orientations and, as mentioned before, several small pores appear (diameter 10 μm). As described in chapter 1.9.1, as a consequence of T6 treatment, silicon diffuses and forms spheroidal particles in the aluminum matrix. This spheroidization transformation results therefore into a more homogenous microstructure, because the original L-PBF features are overshadowed by the heat-induced spatial redistribution and rearrangement of the constituent elements [110,183].

Microstructural features can be appreciated more clearly in the FEG-SEM images in Figure 83.

The same microstructure previously reported by Yang et al. [101] can be seen (Figure 83-A and B), with α-Al cells, separated by a network of extremely fine and packed circular eutectic Si particles. After T6 heat treatment, only coarsened and irregular silicon particles can be seen (Figure 83-C and D).

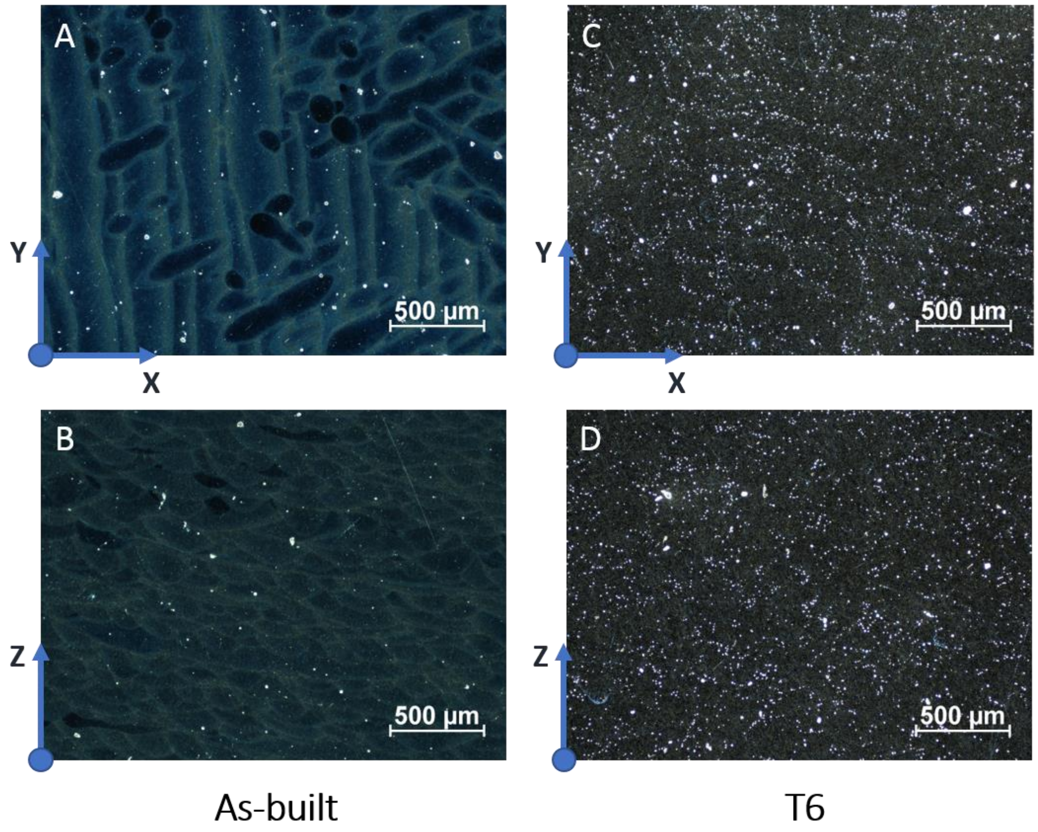

Figure 82: Optical microscope images of AlSi7Mg samples in the two orientations and with 2 heat treatment conditions. The porosities appear white instead of dark because the images have been acquired with grazing incidence illumination in order to see the laser scan tracks.

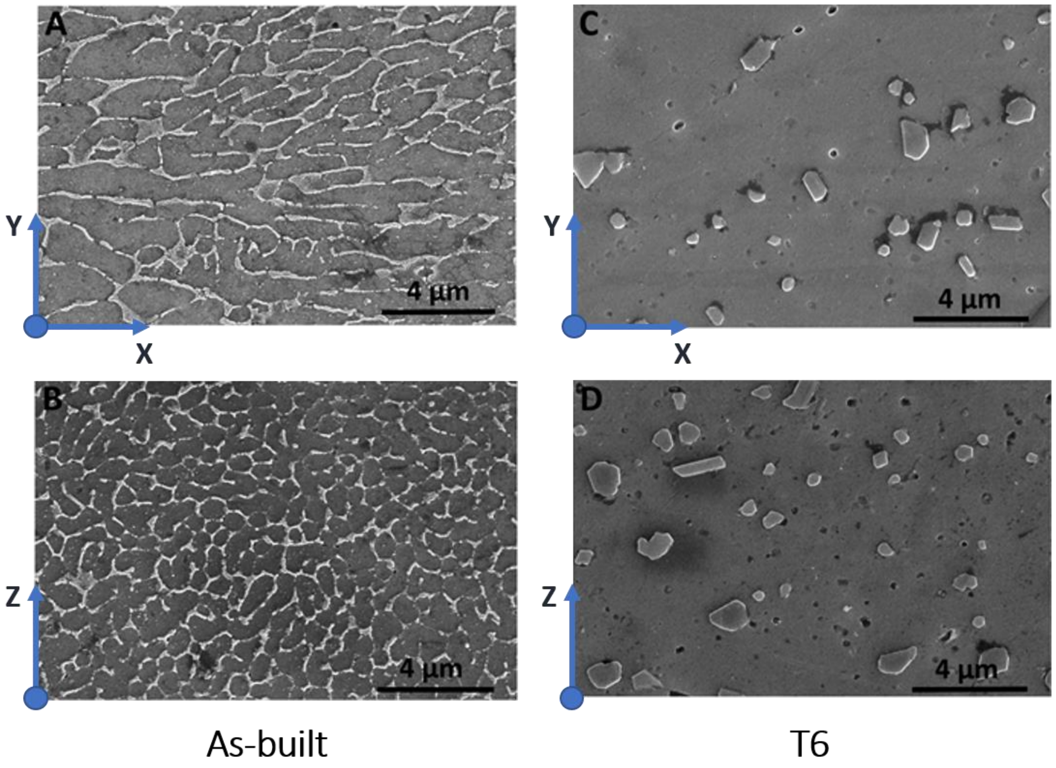

Figure 83: SEM-FEG images of the AlSi7Mg samples in the two orientations and the two heat treatment conditions.

The density values measured by means of Archimedes' method and the porosity values measured with optical images processing are shown in Table 26 for the 4 conditions. These analyses were performed on cut portions of broken fatigue samples.

According to Spierings et al. [184], in principle the porosity values determined through the Archimedes method are expected to be more reliable than those based on image analysis, since all the volume of the sample is taken into account, and not just some single cross sectional areas.

On the other hand, the preliminary machining operation may cause the opening of sub-superficial pores [101], thus influencing the results of the porosity evaluation based on the Archimedes method [184]. Nonetheless, it is interesting to note that, in the present case, both experimental approaches gave comparable results and confirmed that as-built samples were almost fully dense, as long as all the corresponding porosity values ranged between 0.15% to 0.30% independently of the building orientation. After T6 treatment, the porosity amount significantly increased to around 1%. During solution heat treatment, entrapped gas pores can expand and thus cause blistering [185].

Heat Treatment	Orientation	Porosity, Image Analysis [%]	Porosity, Archimedes [%]
As-built	Z	0.30	0.15
As-built	XY	0.15	0.19
T6	Z	0.83	1.01
T6	XY	0.75	1.27

Table 26: Residual porosity for each group of samples as determined via image elaboration and Archimedes method.

In terms of fatigue strength, the performance is almost unchanged before and after the T6 treatment, and is also practically the same in the two build orientations, with only a slight advantage for XY specimens in terms of reliability, which becomes sizeable only if the accepted probability of failure is reduced to 10%.

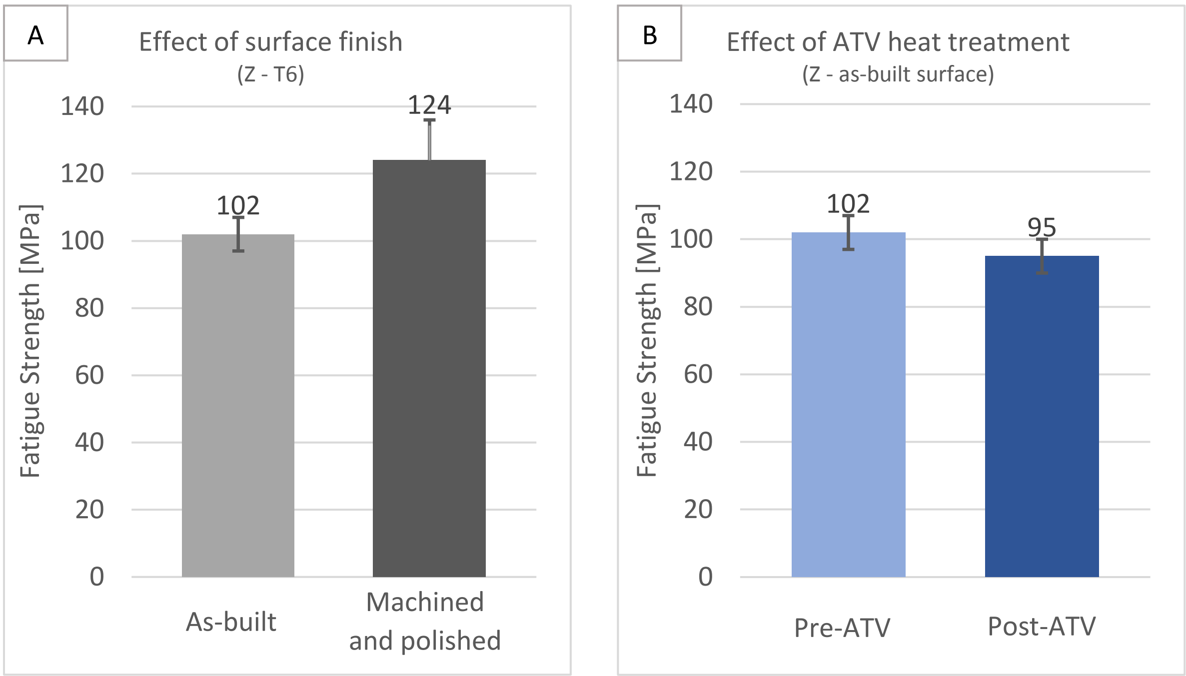

Figure 84: (A) Comparison between as-built vs. polished surface and (B) effect of ATV heat treatment on fatigue strength.

Effect of the surface finish can be then investigated by comparing the samples built along Z direction in the as-built condition and with the polished surface. These samples were not heat treated. The results are shown in Figure 84-A.

As expected, lower roughness and better surface consistency leads to an increase in the fatigue strength, in fact, samples with polished surface show a 22% increase of the fatigue strength. As seen in the images of the fracture surface, the irregularities on the surface of as-built parts act as stress concentrators, leading to lower fatigue strength.

Finally, the effect of the ATV heat treatment can be evaluated. Even if the T-t curve of the treatment is not available (due to confidentiality), the temperature for paint curing is generally around 200°C [186], hence far from a temperature which can cause microstructural alteration. However, over-aging phenomena can already happen at 200°C: diffusion mechanisms are activated so an increase in the dimension of the Mg-Si particles can occur, reducing the strengthening effect of the precipitated particles. A 7% reduce of fatigue strength after the ATV process can be seen from the tests, though the fatigue strength values of ATV and Non-ATV treated samples are consistent considering the standard deviation.

3.2 Ti6Al4V alloy

Table 27 sums up the test conditions for the Ti6Al4V alloy. The tensile tests of the optimized process package were not performed due to logistic issues.

Ti6Al4V Test Variables				
Test	**Process package**	**Powder**	**Orientation**	**Surface condition**
Tensile	Standard	Pure	XY	Machined
			Z	
		Contaminated	XY	
			Z	
	Optimized	Pure	XY	
			Z	
		Contaminated	XY	
			Z	
Fatigue	Standard	Pure	XY	Mach. + Pol.
		Contaminated	XY	
	Optimized	Pure	XY	Mach. + Pol.
		Contaminated	XY	
		Pure	Z	Mach. + Pol.
		Pure	Z	As-built

Table 27: Ti6Al4V test plan. Red colored samples conditions were not tested due to logistic issues.

3.2.1 Tensile tests results

Tensile tests conditions are explained in chapter 2.2.1. The mechanical properties measured are summed up in Table 28, comparison plots are then presented in Figure 85.

The first thing that can be noted is a global increase in tensile properties due to the use of contaminated powder (0.5% wt of X3NiCoMoTi powder). The increase is small, nearly 2.8% for the values of $R_{p0.2}$ and R_m. However, the value of A_t raises up to 25% due to the presence of the contaminant. However, the results of the comparison should be considered with caution and confirmed by additional trials due to the high dispersion of the results and the small amount of samples used for the tests.

Sample ID	Powder	Orientation	E [GPa]	$R_{p\,0.2}$ [MPa]	R_m [MPa]	A_t [%]
111	Pure	XY	117	956	1070	14.9
112	Pure	XY	116	942	1056	13.9
113	Pure	XY	116	952	1063	9.9
361	Pure	Z	119	1001	1096	12.3
362	Pure	Z	120	996	1092	10.7
363	Pure	Z	117	991	1091	13.3
111	Contam.	XY	117	984	1092	15.7
112	Contam.	XY	118	992	1097	17.3
113	Contam.	XY	118	986	1095	15.3
361	Contam.	Z	121	1026	1114	15.3
362	Contam.	Z	124	1023	1112	14.1
363	Contam.	Z	119	1021	1107	13.7

Table 28: Tensile tests results of Ti6Al4V samples.

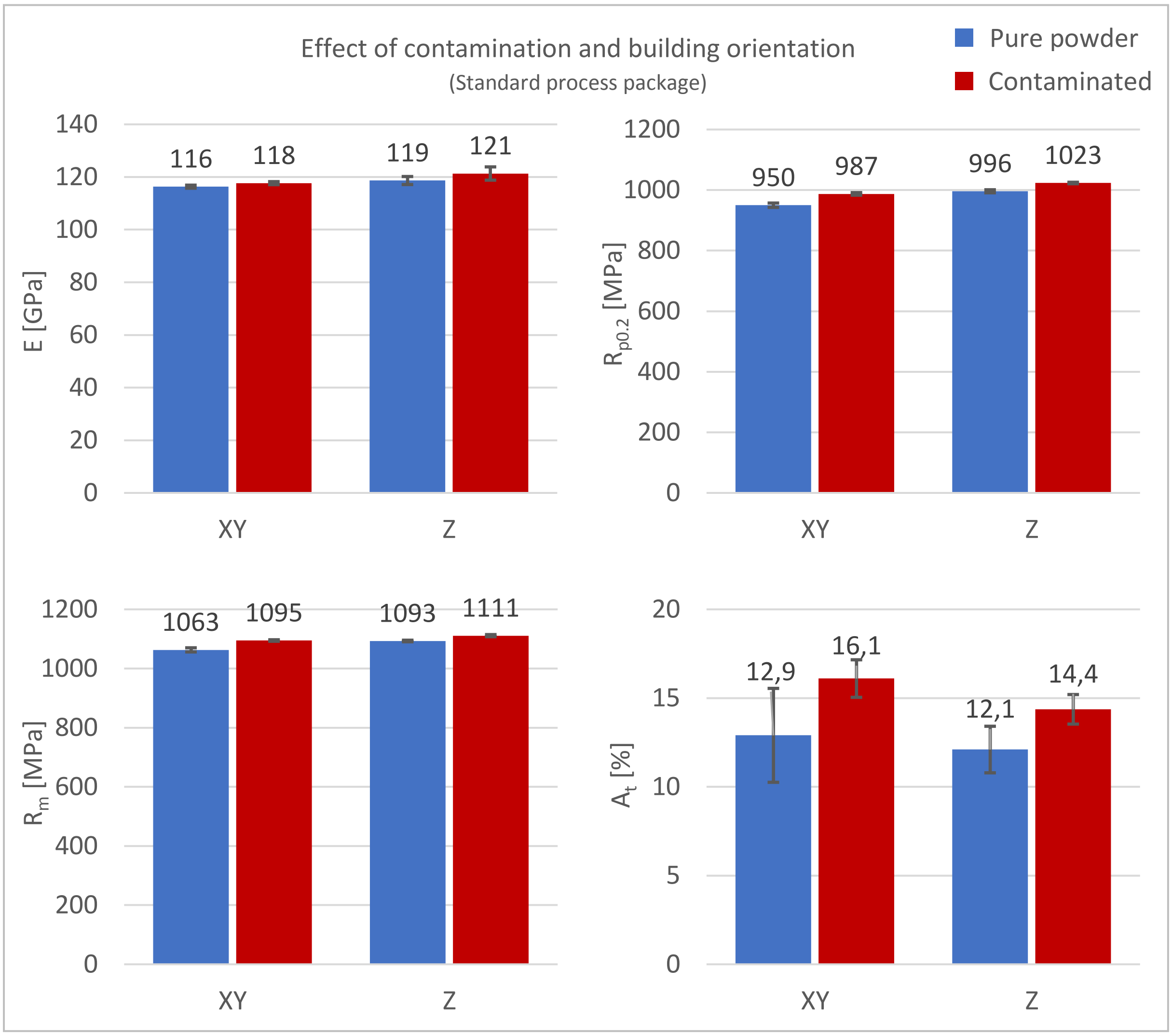

Figure 85: comparison plot of the mechanical properties of Ti6Al4V samples produced with pure and contaminated powder, in XY and Z directions.

3.2.2 Fatigue tests results

Tables 29 – 34 show the results of the fatigue tests performed on Ti6Al4V samples, using the staircase method. In the title of the table are indicated: Material – Powder – Process package – Orientation – Surface condition – Batch number.

Ti6Al4V – Pure Powder – Standard – XY – Machined and polished – 010

Stress		Tests [Test n° / Specimen ID / Cycles to rupture]															Results	
Stress Level	Max Stress [MPa]	1	2	3	4	5	6	7	8	9	10	11	12	13	14	15	X	O
		912	971	951	953	981	972	931	991	992	952	911	932	993	983	982		
		9.60 E+05	1.00 E+07	4.68 E+05	1.00 E+07	2.32 E+05	1.00 E+07	1.00 E+07	1.62 E+05	4.78 E+05	1.14 E+06	1.00 E+07	1.00 E+07	1.83 E+05	1.00 E+07	4.74 E+05		
3	450								X								1	0
2	425	X		X		X		O		X				X		X	6	1
1	400		O		O		O				X		O		O		1	5
0	375											O					0	1
																	8	**7**

Table 29: Staircase fatigue results for Ti6Al4V samples. Build and treatment details are given in the title of the table.

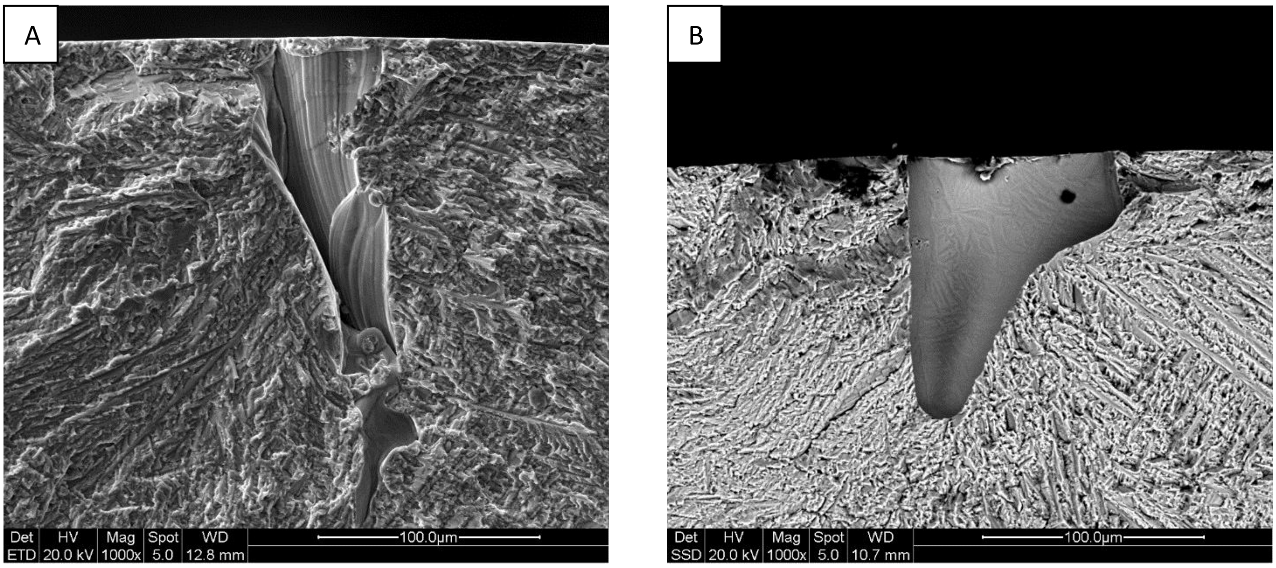

Figure 86: SEM images of crack initiation defects of samples: 912 - Medium (A) and 993 - Early (B)

The defects shown in Figure 86 have a dimension of approximately 100 µm and they are characterized by smooth internal surface. Similarly to AlSi7Mg samples, these defects are caused by the expansion of gases and consequent oxidation. In fact, also Ti6Al4V is prone to oxidation [112].

Ti6Al4V – Contaminated Powder – Standard – XY – Machined and polished – 020																		
Stress		**Tests [Test n° / Specimen ID / Cycles to rupture]**															**Results**	
Stress Level	**Max Stress [MPa]**	**1**	**2**	**3**	**4**	**5**	**6**	**7**	**8**	**9**	**10**	**11**	**12**	**13**	**14**	**15**	**X**	**O**
		911	932	983	993	992	981	982	991	912	972	953	951	952	971	913		
		7.68 E+04	1.00 E+07	1.40 E+05	1.80 E+05	1.90 E+05	3.24 E+05	1.60 E+05	1.00 E+07	1.51 E+05	1.00 E+07	1.20 E+06	1.00 E+07	1.00 E+07	2.26 E+05	1.00 E+07		
5	500	X		X													2	0
4	475		O		X												1	1
3	450					X											1	0
2	425						X								X		2	0
1	400							X		X		X		O		O	3	2
0	375								O		O		O				0	3
																	9	**6**

Table 30: Staircase fatigue results for Ti6Al4V samples. Build and treatment details are given in the title of the table.

A first effect of the contamination can be seen from the staircase table (Table 30), in fact more stress levels are used as compared to non-contaminated samples. This will cause higher standard deviation in the definition of the fatigue strength value.

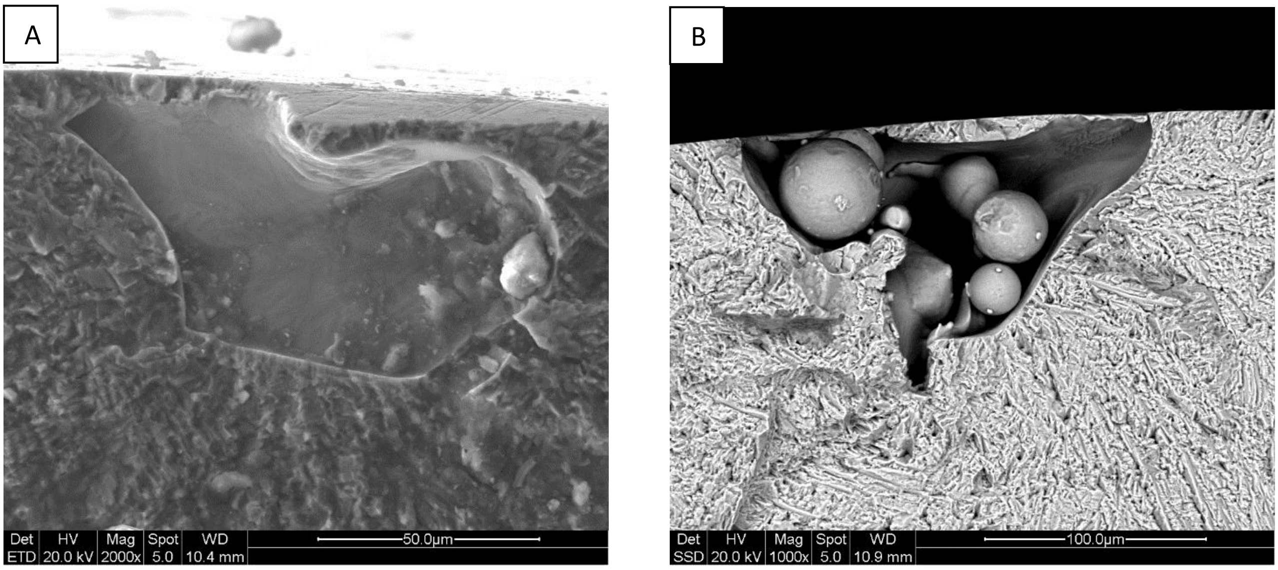

Figure 87: SEM images of crack initiation defects of samples: 953 - Medium (A) and 912 - Early (B)

In contaminated samples, no traces of maraging particles were found, neither in the critical defect, nor in the bulk area of the sample. The initiation points are similar to those of samples made with pure powder, with smooth surfaces and sometimes unfused powder particles (Figure 87). The dimension of the defects is approximately 100 µm in length.

Ti6Al4V – Pure Powder – Optimized – XY – Machined and polished – 030																		
Stress		**Tests [Test n° / Specimen ID / Cycles to rupture]**															**Results**	
Stress Level	**Max Stress [MPa]**	**1**	**2**	**3**	**4**	**5**	**6**	**7**	**8**	**9**	**10**	**11**	**12**	**13**	**14**	**15**	**X**	**O**
		953	991	983	981	992	913	931	912	933	972	951	973	932	982	952		
		1.00 E+07	2.78 E+05	6.45 E+06	1.00 E+07	1.00 E+07	5.87 E+06	1.91 E+06	1.22 E+06	1.00 E+07	1.00 E+07	1.00 E+07	7.91 E+06	6.97 E+06	1.00 E+07	9.34 E+06		
3	625		X				X						X				3	0
2	600	O		X		O		X				O		X		X	4	3
1	575				O				X		O				O		1	3
0	550									O							0	1
																	8	**7**

Table 31: Staircase fatigue results for Ti6Al4V samples. Build and treatment details are given in the title of the table.

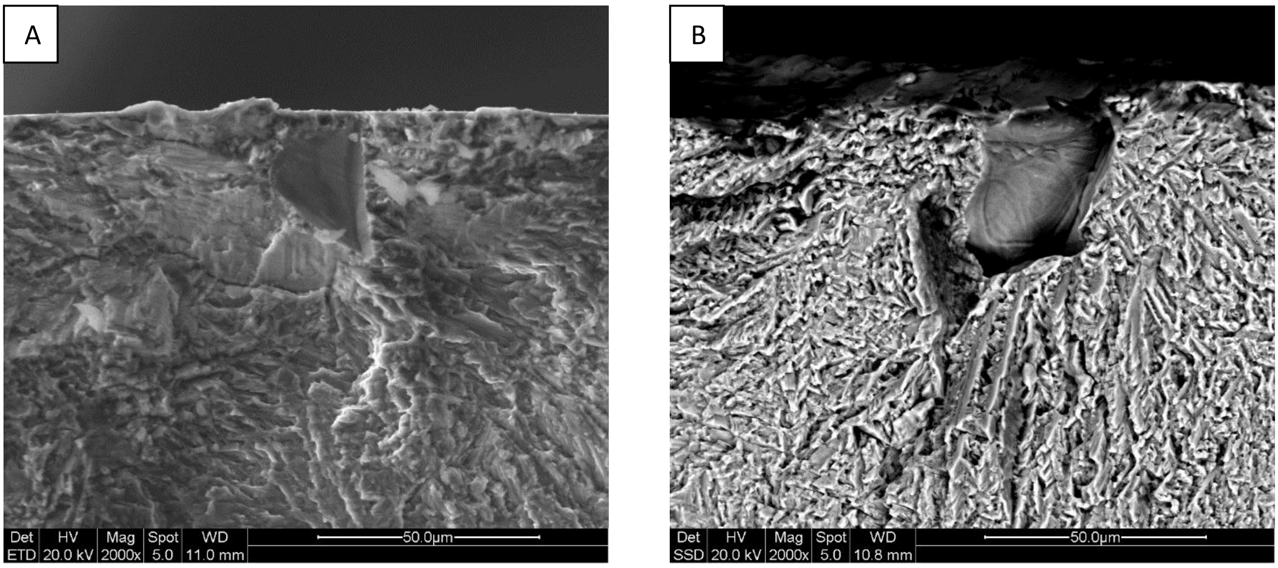

Figure 88: SEM images of crack initiation defects of samples: 952 - Medium (A) and 991 - Early (B)

As for standard parameters samples, the defects in the parts made with optimized process are characterized by smooth surfaces, indicating gas bubble expansion phenomenon.

However, they are smaller than the defects found in standard process samples, in fact, as can be seen in Figure 88, their dimension is lower than 30 µm. This could be a first advantage in the use of the new process package for Ti6Al4V.

Ti6Al4V – Contaminated Powder – Optimized – XY – Machined and polished – 040																		
Stress		**Tests [Test n° / Specimen ID / Cycles to rupture]**															**Results**	
Stress Level	**Max Stress [MPa]**	**1**	**2**	**3**	**4**	**5**	**6**	**7**	**8**	**9**	**10**	**11**	**12**	**13**	**14**	**15**	**X**	**O**
		933	981	911	951	931	971	973	982	993	991	932	972	952	992	983		
		1.87 E+05	1.00 E+07	6.99 E+04	1.28 E+06	1.41 E+05	4.44 E+06	1.53 E+05	1.00 E+07	1.00 E+07	3.65 E+05	1.00 E+07	1.00 E+07	1.00 E+07	1.08 E+05	8.22 E+04		
5	600	X		X													2	0
4	575		O		X										X		2	1
3	550					X								O		X	2	1
2	525						X				X		O				2	1
1	500							X		O		O					1	2
0	475								O								0	1
																	9	**6**

Table 32: Staircase fatigue results for Ti6Al4V samples. Build and treatment details are given in the title of the table.

As can be seen from Table 32, as already seen for the standard process package, contamination has the effect of scattering the results, introducing a higher number of stress levels, hence a higher standard deviation.

Defects are the same of non-contaminated samples, even though they are larger (50-100 µm) (Figure 89).

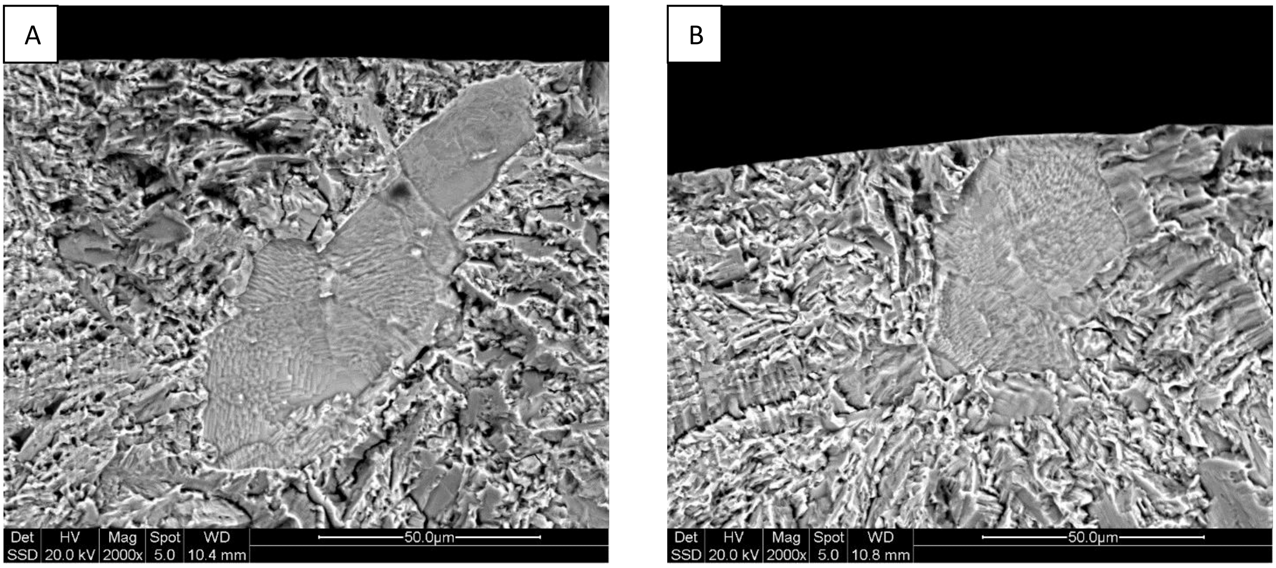

Figure 89: SEM images of crack initiation defects of samples: 971 - Medium (A) and 973 - Early (B)

Ti6Al4V – Pure Powder – Optimized – Z – Machined and polished – 050																		
Stress		**Tests [Test n° / Specimen ID / Cycles to rupture]**															**Results**	
Stress Level	**Max Stress [MPa]**	**1**	**2**	**3**	**4**	**5**	**6**	**7**	**8**	**9**	**10**	**11**	**12**	**13**	**14**	**15**	**X**	**O**
		862	843	861	882	893	863	883	831	833	852	892	841	832	842	853		
		1.00 E+07	8.32 E+06	1.00 E+07	1.00 E+07	3.32 E+06	1.00 E+07	7.70 E+06	1.00 E+07	1.00 E+07	1.00 E+07	1.68 E+06	1.00 E+07	5.81 E+06	1.00 E+07	7.72 E+06		
4	675											X		X		X	3	0
3	650										O		O		O		0	3
2	625					X		X		O							2	1
1	600		X		O		O		O								1	3
0	575	O		O													0	2
																	6	**9**

Table 33: Staircase fatigue results for Ti6Al4V samples. Build and treatment details are given in the title of the table.

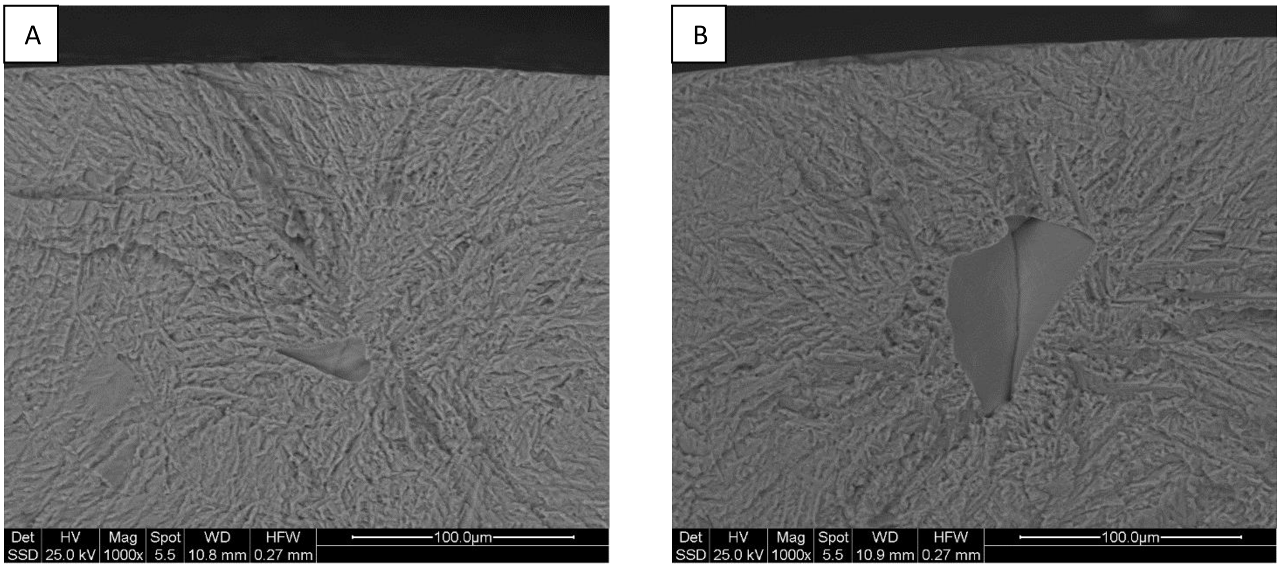

Figure 90: SEM images of crack initiation defects of samples: 842 - Medium (A) and 891 - Early (B)

Defects found on the fracture surface of samples built along Z direction still show smooth surface. In the case of medium sample (Figure 90-A) the dimension is 40 µm then early broken sample shows a 90 µm long defect. Defects dimension is still lower for samples made with optimized process than for standard process samples.

Ti6Al4V – Pure Powder – Optimized – Z – As-Built – 060																		
Stress		**Tests [Test n° / Specimen ID / Cycles to rupture]**															**Results**	
Stress Level	**Max Stress [MPa]**	**1**	**2**	**3**	**4**	**5**	**6**	**7**	**8**	**9**	**10**	**11**	**12**	**13**	**14**	**15**	**X**	**O**
		852	863	862	833	842	832	883	851	841	843	831	882	881				
		1.00 E+07	2.06 E+05	3.93 E+05	1.00 E+07	1.00 E+07	1.00 E+07	1.96 E+05	5.24 E+05	2.68 E+05	1.00 E+07	3.60 E+05	1.00 E+07	1.00 E+07				
3	350							X									1	0
2	325		X				O		X								2	1
1	300	O		X		O				X		X		O			3	3
0	275				O						O		O				0	3
																	6	**7**

Table 34: Staircase fatigue results for Ti6Al4V samples. Build and treatment details are given in the title of the table.

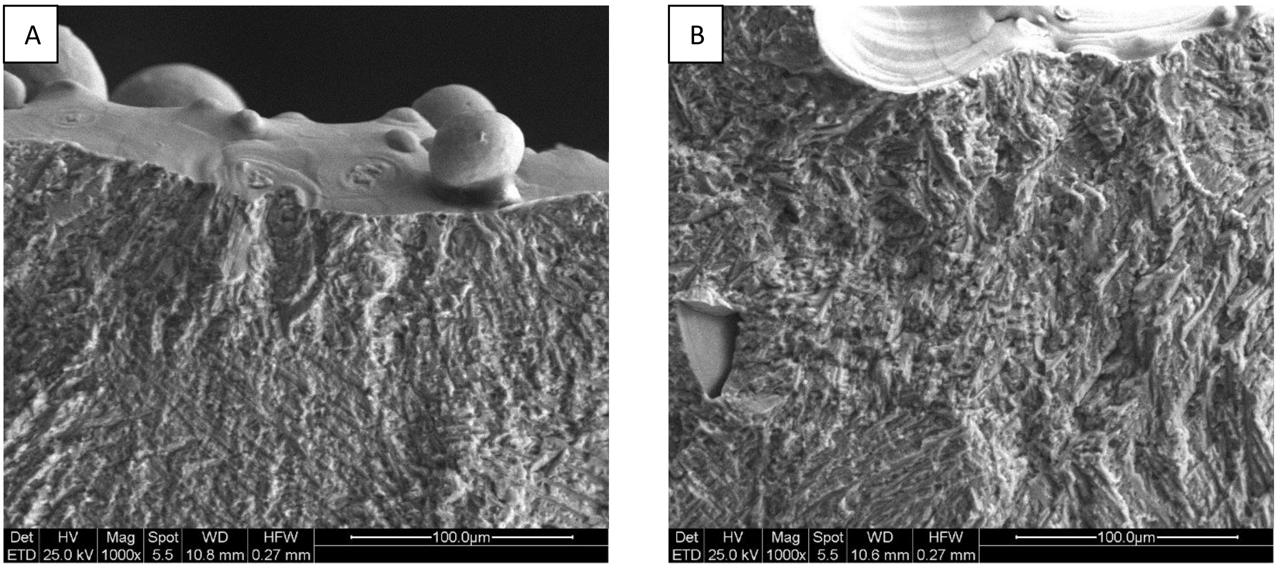

Figure 91: SEM images of crack initiation defects of samples: 851 - Medium (A) and 841 - Early (B)

Despite the advantage seen in term of fatigue strength for optimized process parts, as-built samples are heavily affected by surface unevenness that reduce the fatigue life due to stress intensification on the part surface. Medium sample (Figure 91-A) shows a 30 µm wide superficial defect, probably caused by a crack underneath a partially fuse particle (a circular mark can be seen on the surface of the sample). Early broken sample (Figure 91-B) shows a sub-superficial void characterized by the typical smooth surface with a dimension of 40 µm. The crack may have started from the combination of this defect and the irregularities on the top-right of the image.

Defects dimension is still small, as already seen for the samples made with the optimized process in XY orientation.

The results of fatigue tests on Ti6Al4V are summed up in Table 35.

Process package	Orientation	Surface finish	Powder	Fatigue strength [MPa]		
				Mean	Std Dev	10% / 0.90
Standard	XY	Machined and polished	Pure	413	13	382
Standard	XY	Machined and polished	Contaminated	413	82	208
Optimized	XY	Machined and polished	Pure	595	21	546
Optimized	XY	Machined and polished	Contaminated	533	74	348
Optimized	Z	Machined and polished	Pure	644	70	470
Optimized	Z	As-built	Pure	304	24	245

Table 35: Fatigue strength results for Ti6Al4V alloy with respect to different process package, orientation, surface finish and contaminant content.

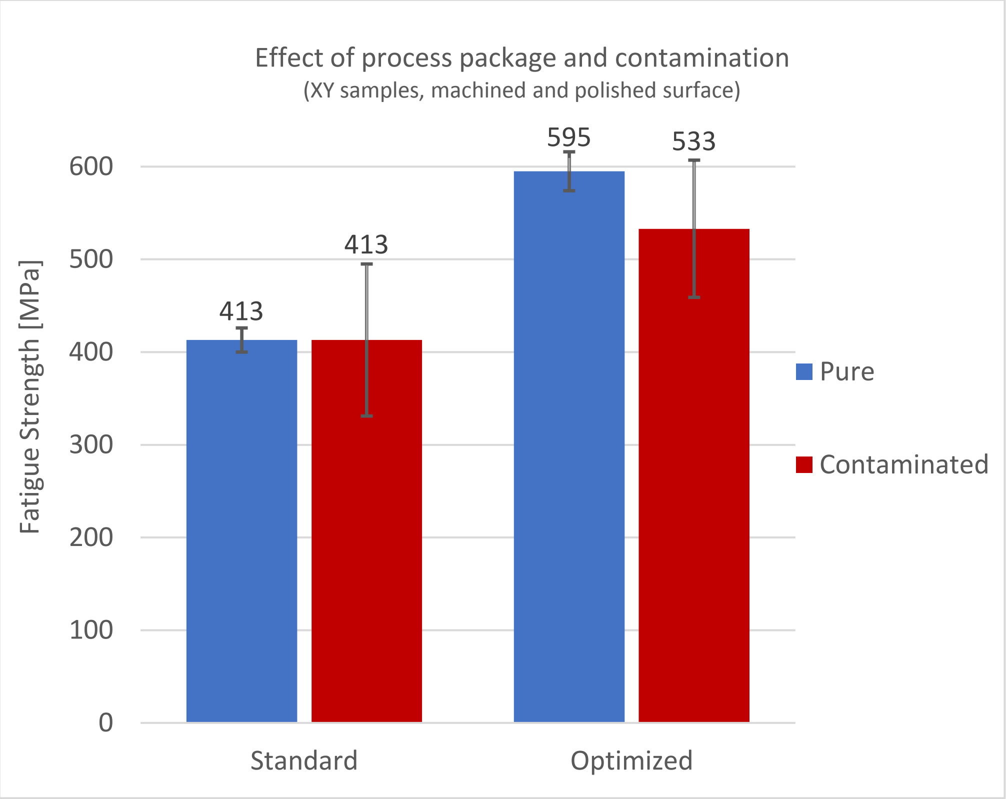

Figure 92: Comparison of the fatigue strength of standard and optimized samples. Contamination effect is considered as well.

As can be seen in the comparison plot of Figure 92, a remarkable increase in fatigue strength is achieved by the optimized process package. The increase respect to the standard process is up to 44%.

Contamination has no effects on the mean value of fatigue strength for standard process package, however, the standard deviation significantly increases.

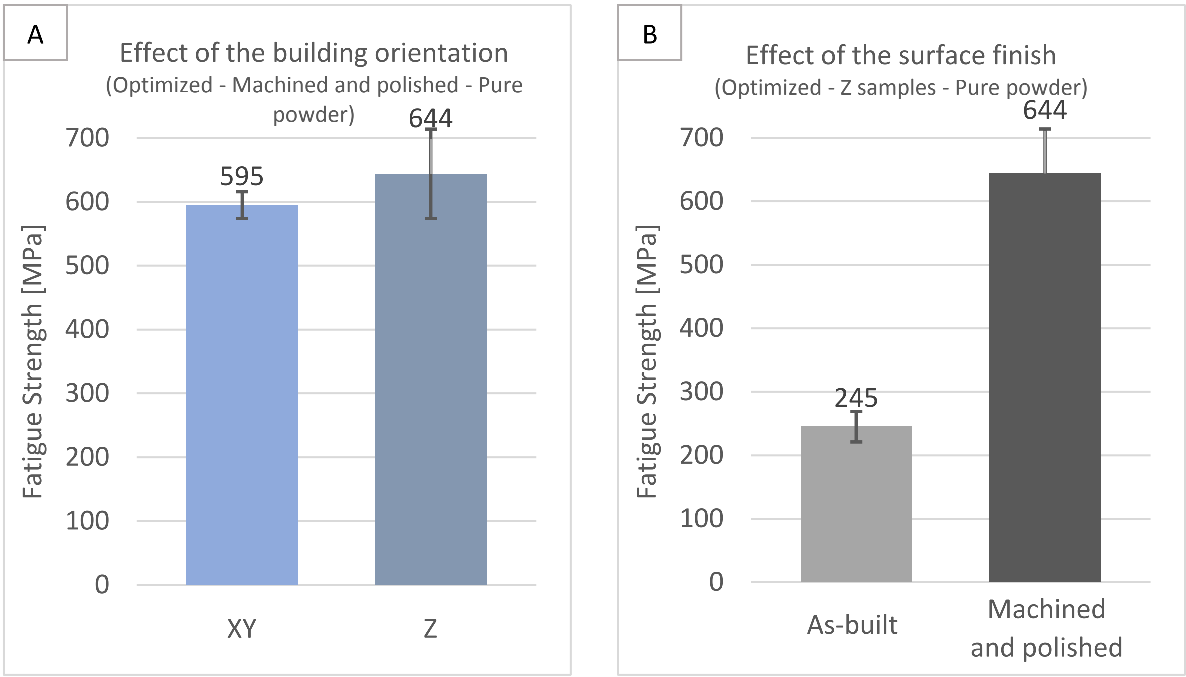

Figure 93: Graphical comparison of the fatigue strength for samples produced with the optimized process package: XY vs. Z direction (A) and as-built vs. machined condition (B)

The same happens for optimized process package where contamination scatters the results and causes a slight decrease of fatigue strength average value (-10%). Due to the high standard deviation induced by the contamination, the fatigue strength calculated at a 10% probability of failure decreases from 382 MPa to 208 MPa (-46%) for standard process and from 546 MPa to 348 MPa (-36%) for the optimized process. So, contamination significantly affect the fatigue strength of the material but the decay is less important for optimized process.

Fatigue strength is not significantly affected by building orientation. Despite the relatively high standard deviation, the mean value of fatigue strength for Z samples is consistent with that of XY samples (Figure 93-A).

Fatigue strength then dramatically decreases if the part is left in the as-built condition. Comparing Z samples (Figure 93-B), fatigue strength decreases from 644 MPa to 254 MPa (-62%). The effect is much more evident than that seen for AlSi7Mg (Figure 84-A) where fatigue strength decreases by 18% if the samples remain in the as-built condition.

3.3 X3NiCoMoTi alloy

Table 36 lists the sample conditions subjected to fatigue testing. All the samples were built in XY direction, so parallel to the building plate. No tensile tests were planned since the mold company was interested only in the study of fatigue behavior.

Test	Process package	Hole	Surface condition
Fatigue	Standard	No	Mach. + Pol.
	Optimized	No	
	Standard	Yes, as-built	Machined
		Yes, machined	

Table 36: X3NiCoMoTi alloy test plan.

3.3.1 Fatigue tests results: regular samples

Table 37 and Table 38 present the results of the fatigue tests performed on X3NiCoMoTi alloy using the staircase method. In the title of the tables are indicated: Material – Parameters set – Building orientation – Surface condition – Batch number.

Maraging steel – Standard – XY – Machined and polished – 010																		
Stress		**Tests [Test n° / Specimen ID / Cycles to rupture]**															**Results**	
Stress Level	**Max Stress [MPa]**	**1**	**2**	**3**	**4**	**5**	**6**	**7**	**8**	**9**	**10**	**11**	**12**	**13**	**14**	**15**	**X**	**O**
		931	991	951	981	912	972	932	992	952	982	913	973	933	993	953		
		4.01 E+05	1.00 E+07	1.00 E+07	1.00 E+07	5.45 E+05	1.00 E+07	2.07 E+05	2.90 E+06	1.00 E+07	1.00 E+07	9.74 E+04	1.00 E+07	1.07 E+05	1.00 E+07	1.00 E+07		
3	650					X		X				X		X		O	4	1
2	625				O		O		X		O		O		O		1	5
1	600	X		O						O							1	2
0	575		O														0	1
																	6	**9**

Table 37: Staircase fatigue results for X3NiCoMoTi samples. Build and treatment details are given in the title of the table.

The fracture surface of the medium sample built with the standard process shows 2 possible crack initiation defects (Figure 94-A, B and C). The first one (Figure 94-B) is an irregularly shaped LOF, 50 µm long, with some unfused particles inside it. The defect starts from the surface of the sample and develops inside the part. The other defect is another superficial irregularly shaped LOF with a maximum dimension of 100 µm. Cracks start from both the defects but failure is generated by the defect in Figure 94-B. In fact, in Figure 94-C, the clamshell marking can be seen, starting from the initiation defect but it interrupts abruptly due to the main crack developing path, starting from the defect of Figure 94-B.

Figure 94-D shows the critical defect of the early broken sample. EDS analysis was performed on the darker area, resulting in a titanium contamination. This result is consistent with the fact that the standard process has a material formulation for which purity could be improved.

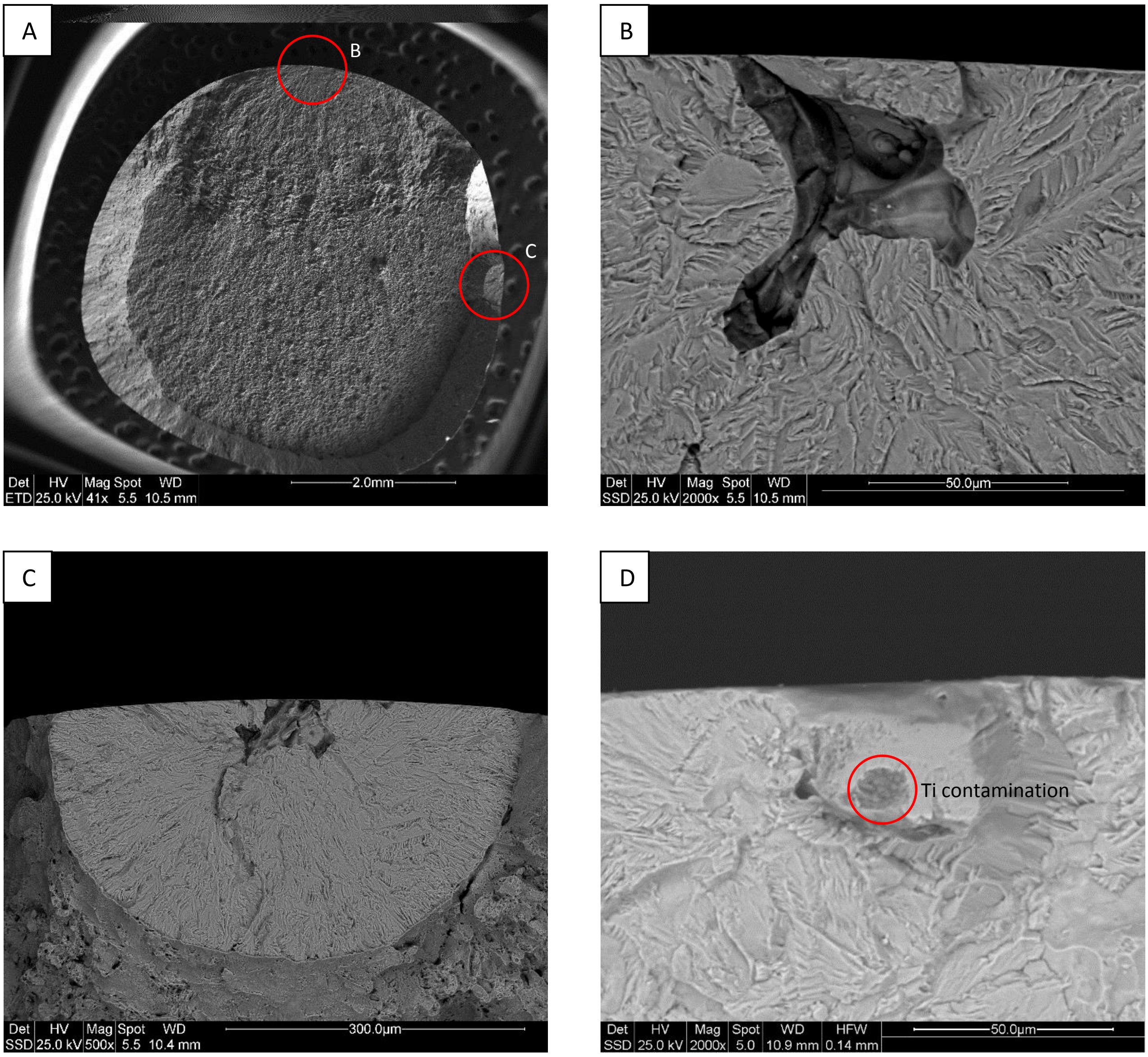

Figure 94: SEM global image of the fracture surface of sample 912 – Medium (A). The red circles indicate the two initiation points of the crack. SEM images of crack initiation defects of samples 912: defect 1 (B) and defect 2 (C). SEM image of crack initiation defect of sample 913 - Early (D); the darker spot is a titanium particle contamination.

Maraging steel – Optimized – XY – Machined and polished – 020																		
Stress		**Tests [Test n° / Specimen ID / Cycles to rupture]**															**Results**	
Stress Level	**Max Stress [MPa]**	**1**	**2**	**3**	**4**	**5**	**6**	**7**	**8**	**9**	**10**	**11**	**12**	**13**	**14**	**15**	**X**	**O**
		951	912	913	983	932	933	952	972	993	992	982	991	971	973	931		
		1.00 E+07	8.67 E+04	1.39 E+05	1.00 E+07	1.40 E+05	8.60 E+04	1.00 E+07	1.00 E+07	4.86 E+06	1.00 E+07	1.60 E+06	7.32 E+05	1.00 E+07	4.34 E+05	1.35 E+05		
3	700		X														1	0
2	675	O		X		X				X		X					4	1
1	650				O		X		O		O		X		X		3	3
0	625							O						O		X	1	2
																	9	**6**

Table 38: Staircase fatigue results for X3NiCoMoTi samples. Build and treatment details are given in the title of the table.

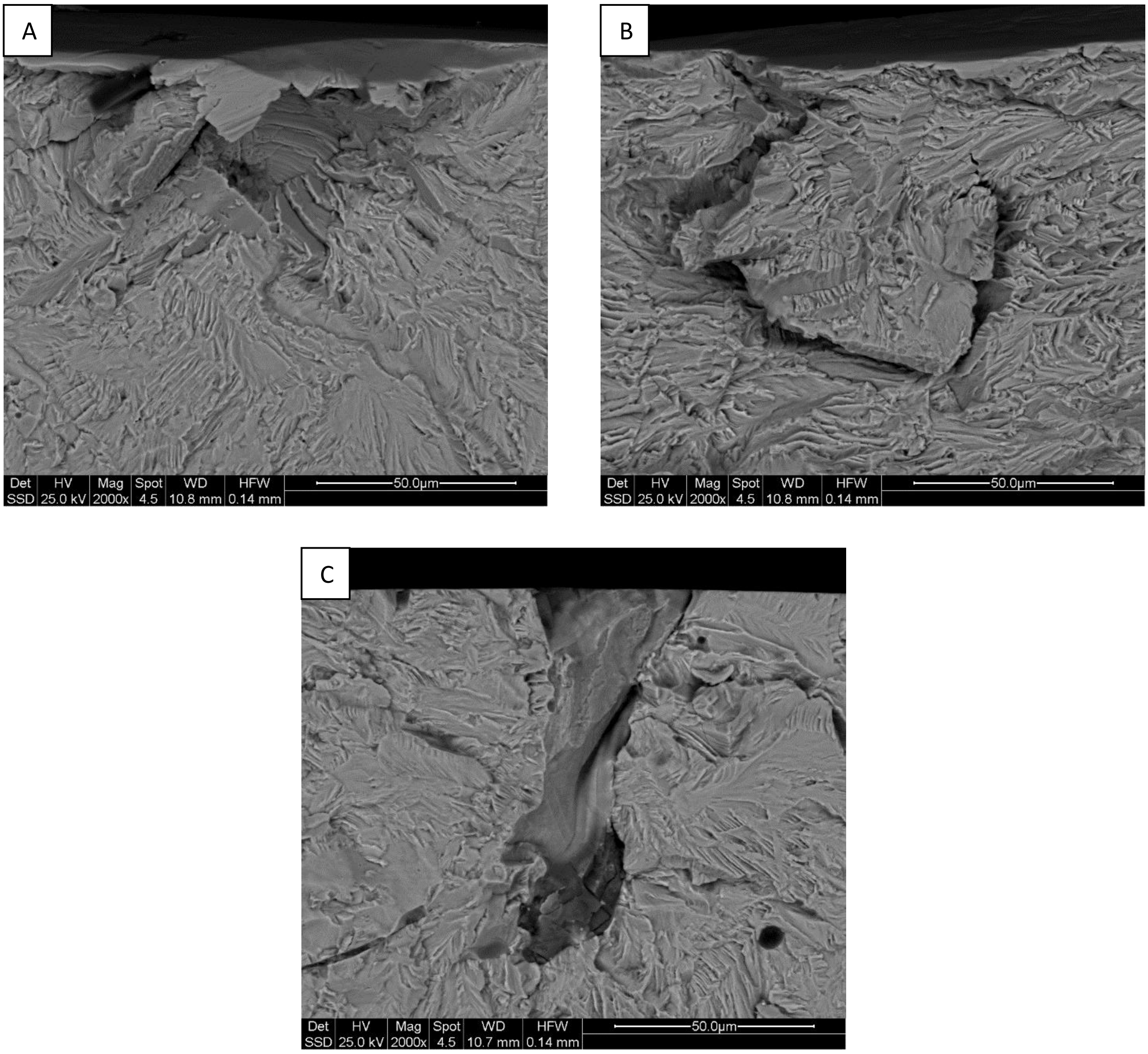

Figure 95: SEM images of crack initiation defects of samples: 982 - Medium (A and B) and 933 - Early (C)

As regards the optimized process package, the average sample shows 2 initiation defects placed 300 μm far from each other. The first one (Figure 95-A) is less than 50 μm long and it is placed right under the surface, covered by a layer of material that was probably spread during the polishing process. The defect does not seem a proper lack of fusion but most probably a poor bonding area caused by slight oxidation.
The second defect (Figure 95-B) is a crack. It indicates some sort of residual stress retained in the part, probably not completely relieved by the heat treatment and then worsened by the machining process.

Early broken sample shows a regular lack of fusion defect starting from the surface of the sample and going deeper for 90 μm. As the defects found for Titanium samples, this one shows a smooth internal surface, denoting a possible expansion of a gas bubble developed inside the melt pool during the building process.

None of the analyzed defects showed titanium contamination.

Table 39 summarizes the results of fatigue tests performed on the 2 sample batches and Figure 96 compares the results.

Process package	Fatigue strength [MPa]		
	Mean	Std Dev	10% / 0.90
Standard	625	25	563
Optimized	658	20	608

Table 39: Results of staircase fatigue testing on X3NiCoMoTi alloy.

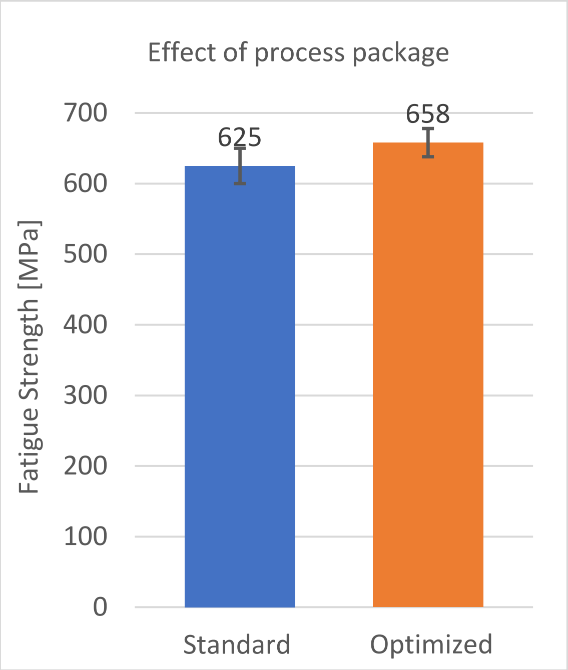

Figure 96: Comparison of fatigue strength of standard and optimized process samples.

The fatigue strength achieved with the optimized process is compared to the standard process in Figure 96. The average value gain is only of 5%, however, optimized process also provides lower standard deviation, which proves a more consistent fatigue behavior and turns into an increase in fatigue strength of 8% if a probability of failure of only 10% is accepted.

3.3.2 Fatigue tests results: samples with hole

The results of the tests on samples with hole are summed up in Table 40. The maximum stress has been used to calculate the maximum load applied in the fatigue cycle. The load was calculated by considering the actual minimum cross section area of the sample, reduced by the presence of the hole.

Sample ID	Hole condition	Sample D [mm]	Hole D [mm]	Max Stress [MPa]	Cycles count
1_AB	As-built	5.03	1.75	200	2.23E+05
2_AB	As-built	5.05	1.82	100	>1.00E+07
3_AB	As-built	5.09	1.87	150	1.12E+06
1_M	Machined	5.06	1.96	300	3.15E+05
2_M	Machined	5.06	2.00	200	>1.00E+07
3_M	Machined	5.07	2.02	250	6.80E+05

Table 40: Results of fatigue testing on X3NiCoMoTi samples with transverse hole.

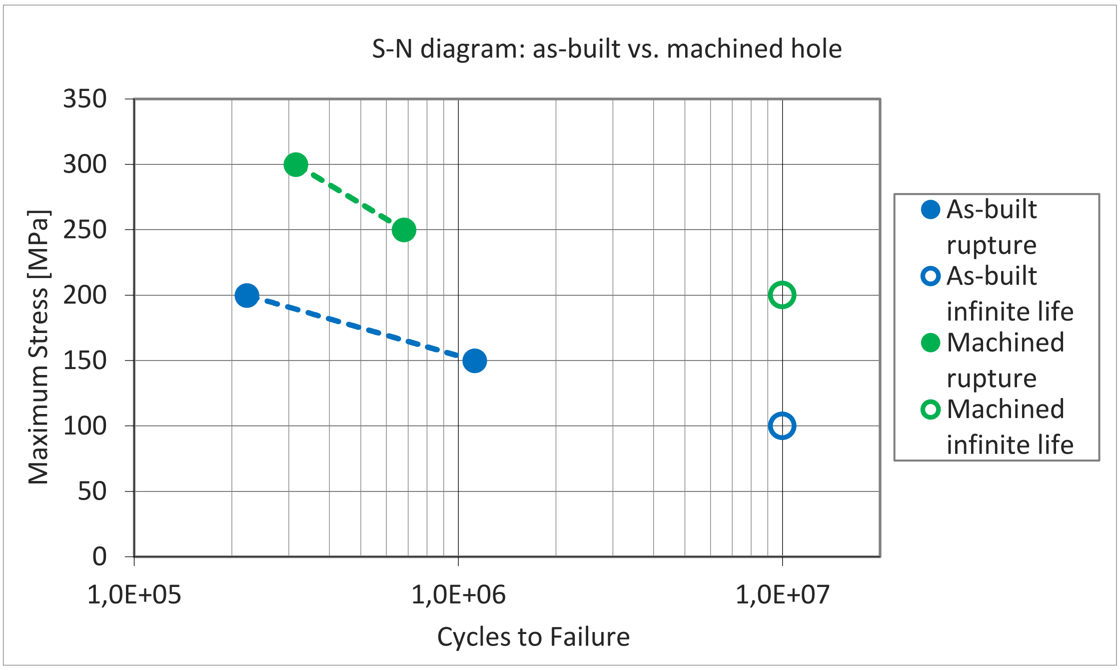

Figure 97: S-N diagram of fatigue tests results of samples with hole.

As predictable, the hole acts as a stress intensifier, so the fatigue strength is reduced by its presence. For the same geometry of the hole, Figure 97 allows to distinguish the effect of the surface roughness inside the hole, as it is achieved by the laser powder bed fusion process. As a rough estimate, leaving the hole surface in the as-built state causes a decrease in the maximum fatigue stress of about 100 MPa, for the same number of cycles to rupture as well as for infinite life. The effect can be ascribed to the surface unevenness that can be observed inside the as-built hole, particularly in the down-skin side. In fact, as can be seen in Figure 98, due to the orientation of the sample during the building process, the transverse hole has an upward and a downward surface. Downward surface was consolidated on loose powder, causing an irregular surface composed of partially melted particles (Figure 99-A). The upward surface, on the other hand, is more regular and smoother as can be seen in Figure 99-B.

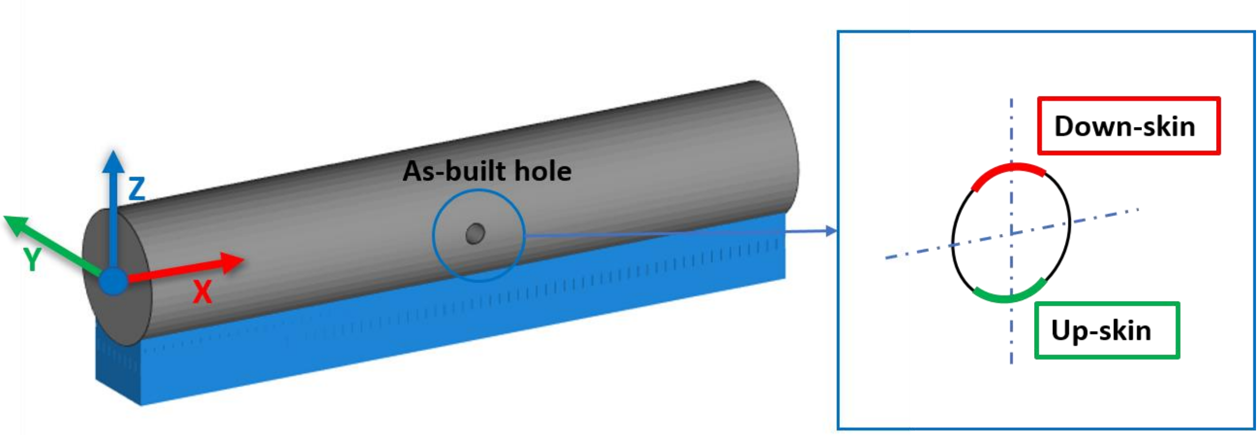

Figure 98: Building orientation of the samples with transverse hole, detailing the up-skin and down-skin areas of the hole.

Hence, the failure is most likely caused by the unevenness of the down-skin area, as shown in Figure 99-C and D where multiple crack initiation points can be spotted along the down-skin side.

On the other hand, the fracture surface of the sample with drilled hole (Figure 100) does not show any particular initiation defect. By evaluating the development lines of the crack, the failure seems to start from the corner visible in Figure 100-B. This is consistent with the theory according to which the stress at the hole edge is 3 times the mean stress [187].

After rupture, the inner morphology of the holes was measured by confocal scanning microscopy. The results are listed in Table 41, where roughness of the as-built hole appears around two orders of magnitude higher than that of the drilled holes.

ISO 25178 Surface GPS		
Param.	As-built hole	Mach. hole
S_q	15.8 µm	0.22 µm
S_{sk}	1.37	1.09
S_{ku}	5.51	11.2
S_p	64.9 µm	1.23 µm
S_v	26.2 µm	0.84 µm
S_z	91.1 µm	2.06 µm
S_a	11.7 µm	0.14 µm

Table 41: Results of roughness measures on the surface of the samples' hole, after rupture.

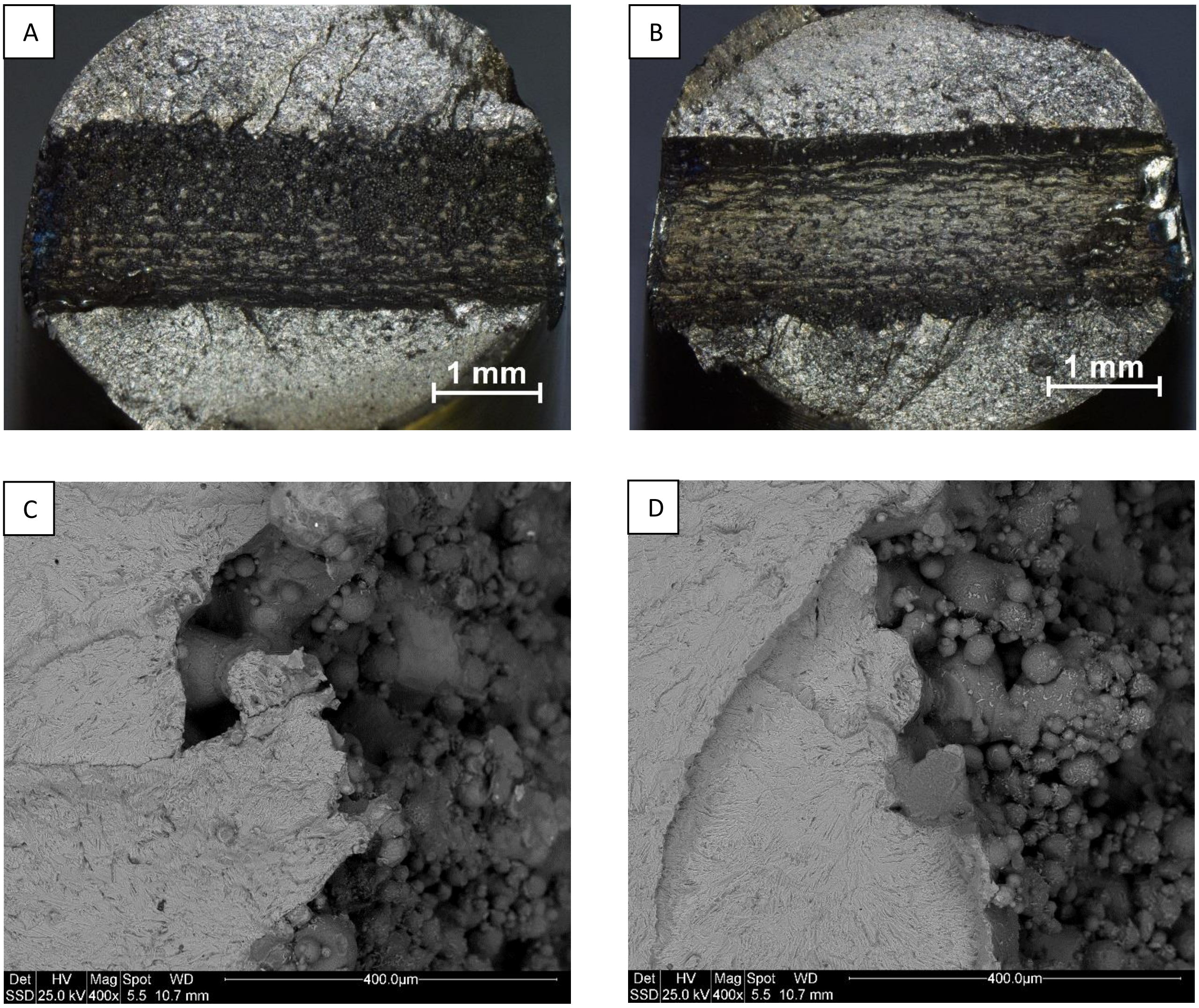

Figure 99: Optical images of the as-built hole. The sample has been tilted to expose (A) downskin and (B) upskin of the hole. Figure (C) and (D) show details of some defects located in the downskin area of the fracture surface.

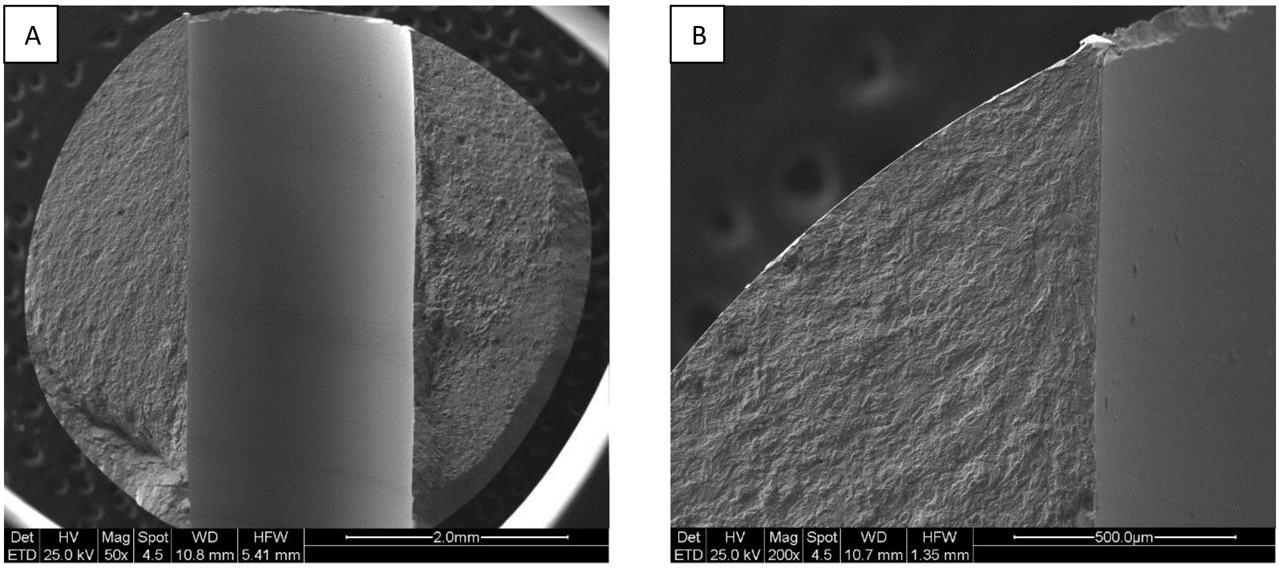

Figure 100: SEM images of the fracture surface of a sample with drilled hole.

4. Conclusions

In conclusion, the research carried out during the PhD covered a vast experimental investigation on the fatigue life of metallic materials constructed through the laser powder bed fusion process.

The main findings of this work are the following:

- A heat treatment performed at a temperature above the stress relief temperature tends to homogenize the tensile and fatigue properties obtained for samples built in the two building directions. Hence the anisotropy generated during the building process is minimised. This aspect has been verified for AlSi7Mg (subjected to solution heat treatment) and Ti6Al4V (subjected to stress relief heat treatment). However, porosity increases from 0.2% to 1% in AlSi7Mg after solution heat treatment as a consequence of blistering.
- The optimized process package used to produce Ti6Al4V samples results in an impressive increase in the fatigue strength by 44% (considering samples made with pure powder).
- A controlled contamination of 0.5% wt. of maraging steel in Ti6Al4V powder does not deteriorate significantly the tensile properties of Ti6Al4V samples that, on the contrary, slightly increase.
  Fatigue strength is heavily affected, in particular in term of reliability. In fact, due to the high standard deviation resulting from the tests of contaminated samples, the fatigue strength with a 10% probability of failure decreases by 46% for standard process and by 36% for optimized process.
- The fatigue performance of as-built samples is always worse than that of polished samples as a consequence of the surface unevenness that promotes crack initiation. The difference is less significant for AlSi7Mg (-18%) but prominent for Ti6Al4V (-62%).
- The fatigue strength of maraging steel improved as a consequence of process optimization. Although the enhancement was less important than that observed for Ti6Al4V, the value of fatigue strength for a 10% probability of failure increases by 8%. This confirms the importance of optimizing the entire process variables to control the fatigue behavior of L-PBF parts.
- As expected, samples with transverse hole exhibits a much lower fatigue strength with respect to solid parts (∼150 MPa instead of 625 MPa) due to the stress concentration induced by the hole. However, a drilled hole offers roughly 100 MPa higher fatigue strength than as-built hole. Since no machining can be performed inside internal cooling channels, the effects of a finishing process for internal channels such as Abrasive flow machining (AFM) should be studied.

The fatigue tests performed in this work helped in the evaluation of many variables involved in the manufacturing process and in the practical application of L-PBF.
Future research could aim at improving further the reliability of the results by testing more samples for every condition, 28 for instance, as suggested by ISO 12107 standard.

Additionally, much interest is focused on the welding of AlSi7Mg and generally aluminum alloys made by L-PBF. In particular, the sports car company involved in this work is going to study the fatigue performance of L-PBF part and cast part weld junction.

For Ti6Al4V, future research may involve the optimization of building process and mass surface finishing operations to improve the fatigue performance of as-built parts.

As mentioned above, interesting studies could be performed on X3NiCoMoTi alloy, to evaluate the mechanical and flow behavior of internal cooling channels treated with AFM.

For their extension and deepness, the results achieved represent an undoubted progress as compared to the state of the art on this topic. The study allowed to build an extended panorama on the fatigue behavior of three of the most used metal alloys in additive manufacturing, taking into consideration the effect of the optimization of the process parameters, of the build orientation, of the heat treatment condition and of the surface finish.

The main value of this research is therefore to represent a reference for what concerns the numerical quantification and the understanding of the mechanisms that govern the fatigue behavior of metal alloys built through the laser powder bed fusion process, guaranteeing solid foundations for a more conscious and reliable industrial application.

References

1. Attaran, M. The rise of 3-D printing: The advantages of additive manufacturing over traditional manufacturing. *Bus. Horiz.* **2017**, *60*, 677–688, doi:10.1016/j.bushor.2017.05.011.
2. Prototype Available online: https://en.wikipedia.org/wiki/Prototype.
3. ASTM INTERNATIONAL ASTM F2792-12a. *Rapid Manuf. Assoc.* **2013**, 1–3, doi:10.1520/F2792-12A.2.
4. Gebhardt, A. *Understanding Additive Manufacturing*; Carl Hanser Verlag GmbH & Co. KG: München, 2011; ISBN 978-3-446-42552-1.
5. Kalpakjian, S.; Schmid, S. *Manufacturing Engineering & Technology, 7th Edition*; 2014; ISBN 9780133128741.
6. Lasemi, A.; Xue, D.; Gu, P. Recent development in CNC machining of freeform surfaces: A state-of-the-art review. *Comput. Des.* **2010**, *42*, 641–654, doi:10.1016/j.cad.2010.04.002.
7. Nicolaou, P.; Thurston, D.L.; Carnahan, J. V. Machining Quality and Cost: Estimation and Tradeoffs. *J. Manuf. Sci. Eng.* **2002**, *124*, 840–851, doi:10.1115/1.1511169.
8. Salonitis, K.; Zarban, S. Al Redesign Optimization for Manufacturing Using Additive Layer Techniques. *Procedia CIRP* **2015**, *36*, 193–198, doi:10.1016/j.procir.2015.01.058.
9. Dassault Systemes TOSCA - Efficient optimization based on FEA and CFD simulations Available online: http://www.3ds.com/products-services/simulia/products/tosca/.
10. General Electrics Mind Meld: How GE And A 3D-Printing Visionary Joined Forces Available online: https://www.ge.com/reports/mind-meld-ge-3d-printing-visionary-joined-forces/fuel-nozzle/.
11. Tomas Kellner An Epiphany Of Disruption: GE Additive Chief Explains How 3D Printing Will Upend Manufacturing Available online: https://www.ge.com/reports/epiphany-disruption-ge-additive-chief-explains-3d-printing-will-upend-manufacturing/.
12. Zhang, P.; Liu, J.; To, A.C. Role of anisotropic properties on topology optimization of additive manufactured load bearing structures. *Scr. Mater.* **2017**, *135*, 148–152, doi:10.1016/j.scriptamat.2016.10.021.
13. Manogharan, G.; Wysk, R.A.; Harrysson, O.L.A. Additive manufacturing–integrated hybrid manufacturing and subtractive processes: economic model and analysis. *Int. J. Comput. Integr. Manuf.* **2016**, *29*, 473–488, doi:10.1080/0951192X.2015.1067920.
14. Baumers, M.; Dickens, P.; Tuck, C.; Hague, R. The cost of additive manufacturing: machine productivity, economies of scale and technology-push. *Technol. Forecast. Soc. Change* **2016**, *102*, 193–201, doi:10.1016/j.techfore.2015.02.015.
15. Jabil Additive Manufacturing and Time to Market for the Win Available online: https://www.jabil.com/solutions/additive-manufacturing/time-to-market.html.
16. Froes, F.; Boyer, R. *Additive Manufacturing for the Aerospace Industry*; Elsevier, 2019; ISBN 9780128140628.
17. King, R. 3D Printing Coming to the Manufacturing Space and Outer Space. **2012**.
18. Siemens 3D Prints Power Turbine Blades Available online: http://www.rapidreadytech.com/2017/06/siemens-3d-prints-power-turbine-blades/.
19. EOS GmbH RUAG - Additive Manufacturing of Satellite Components Available online: https://www.eos.info/case_studies/additive-manufacturing-of-antenna-bracket-for-satellite.

20. Milewski, J.O. *Additive Manufacturing of Metals*; Springer Series in Materials Science; Springer International Publishing: Cham, 2017; Vol. 258; ISBN 978-3-319-58204-7.

21. Rennteam Automotive: Formula Student Germany – EOS supports racing team by producing a topology-optimized steering stub axle Available online: https://www.eos.info/press/customer_case_studies/rennteam_uni_stuttgart.

22. Hirschvogel Tech Solutions Case Report Car Steering Knuckle Hirschvogel Tech Solutions.

23. Bugatti - World premiere: brake caliper from 3-D printer Available online: https://www.bugatti.com/media/news/2018/world-premiere-brake-caliper-from-3-d-printer/.

24. Leal, R.; Barreiros, F.M.; Alves, L.; Romeiro, F.; Vasco, J.C.; Santos, M.; Marto, C. Additive manufacturing tooling for the automotive industry. *Int. J. Adv. Manuf. Technol.* **2017**, *92*, 1671–1676, doi:10.1007/s00170-017-0239-8.

25. Sachdev, A. Transforming metal additive manufacturing for automotive Available online: https://www.theengineer.co.uk/additive-manufacturing-automotive/.

26. Singh, S.; Ramakrishna, S. Biomedical applications of additive manufacturing: Present and future. *Curr. Opin. Biomed. Eng.* **2017**, *2*, 105–115, doi:10.1016/j.cobme.2017.05.006.

27. 3D Printed Prosthetics Where We Are Today - Amputee Coalition Available online: https://www.amputee-coalition.org/3d-printed-prosthetics/.

28. Root, W. EXO prosthetic leg Available online: https://www.behance.net/gallery/20696469/Exo-Prosthetic-Leg.

29. Chen, R.K.; Jin, Y.; Wensman, J.; Shih, A. Additive manufacturing of custom orthoses and prostheses—A review. *Addit. Manuf.* **2016**, *12*, 77–89, doi:10.1016/j.addma.2016.04.002.

30. New Procedures for Hip Surgery.

31. Murr, L.E.; Gaytan, S.M.; Martinez, E.; Medina, F.; Wicker, R.B. Next generation orthopaedic implants by additive manufacturing using electron beam melting. *Int. J. Biomater.* **2012**, *2012*, doi:10.1155/2012/245727.

32. 3D printing of dental restorations. *Met. Powder Rep.* **2013**, *68*, 32–33, doi:10.1016/S0026-0657(13)70062-6.

33. General Electrics Applications in dentistry and orthodontics Available online: https://www.ge.com/additive/additive-manufacturing/industries/dentistry.

34. An, J.; Teoh, J.E.M.; Suntornnond, R.; Chua, C.K. Design and 3D Printing of Scaffolds and Tissues. *Engineering* **2015**, *1*, 261–268, doi:10.15302/J-ENG-2015061.

35. Additive Manufacturing and Metal Casting Available online: https://www.additivemanufacturing.media/blog/post/additive-manufacturing-and-metal-casting(2).

36. 3D Systems Conformal cooling Available online: https://www.3dsystems.com/conformal-cooling.

37. Ruffner, T. Conformal Cooling Using DMLS. *GPI Prototype Manuf. Serv. Inc.* **2012**, *60044*.

38. Auricchio, F. *Additive Manufacturing processes*;

39. Gatto, A.; Bassoli, E.; Denti, L.; Iuliano, L. *Produrre*; 2019;

40. Calignano, F.; Manfredi, D.; Ambrosio, E.P.; Biamino, S.; Lombardi, M.; Atzeni, E.; Salmi, A.; Minetola, P.; Iuliano, L.; Fino, P. Overview on additive manufacturing technologies. *Proc. IEEE* **2017**, *105*, 593–612, doi:10.1109/JPROC.2016.2625098.

41. Guo, N.; Leu, M.C. Additive manufacturing: Technology, applications and research needs. *Front. Mech. Eng.* **2013**, *8*, 215–243, doi:10.1007/s11465-013-0248-8.

42. Atzeni, E.; Salmi, A. Economics of additive manufacturing for end-usable metal parts. *Int. J. Adv. Manuf. Technol.* **2012**, *62*, 1147–1155, doi:10.1007/s00170-011-3878-1.

43. Gu, D.; Wang, H.; Chang, F.; Dai, D.; Yuan, P.; Hagedorn, Y.-C.; Meiners, W. Selective Laser Melting Additive Manufacturing of TiC/AlSi10Mg Bulk-form Nanocomposites with Tailored Microstructures and Properties. *Phys. Procedia* **2014**, *56*, 108–116, doi:10.1016/j.phpro.2014.08.153.

44. SLM Solutions *SLM 280 HL Manual*; 2017;

45. SLM Solutions Material for Selective Laser Melting.

46. EOS GmbH EOS Materials Metal Technical Data. **2018**.

47. Lee Kwok-san, T.S. What is laser? Available online: http://www.hk-phy.org/articles/laser/laser_e.html.

48. Principles and Applications of Laser Available online: http://electrons.wikidot.com/principle-and-application-of-laser.

49. Majumder, S. *Laser*;

50. Patil, N.; Pal, D.; Teng, C.; Zeng, K.; Sublette, T.; Stucker, B. A study of transverse laser modes using a novel multi-scale simulation architecture for laser-based manufacturing technologies. In; Helvajian, H., Piqué, A., Wegener, M., Gu, B., Eds.; 2015; p. 935313.

51. Edmund Optics Gaussian Beam Propagation Available online: https://www.edmundoptics.com/knowledge-center/application-notes/lasers/gaussian-beam-propagation/.

52. Singh, S.C.; Zeng, H.; Guo, C.; Cai, W. Lasers: Fundamentals, Types, and Operations. *Nanomater. Process. Charact. with Lasers* **2012**, 1–34, doi:10.1002/9783527646821.ch1.

53. Ferguson, J. How does a light bulb produce different colors of light? Available online: https://www.quora.com/How-does-a-light-bulb-produce-different-colors-of-light.

54. Radiance Available online: https://www.rp-photonics.com/radiance.html.

55. Modes of Laser Operation Available online: https://www.rp-photonics.com/modes_of_laser_operation.html.

56. Paschotta, R. Solid state lasers Available online: https://www.rp-photonics.com/solid_state_lasers.html.

57. Chang, I.; Zhao, Y. *Advances in Powder Metallurgy - 1st Edition*; Woodhead Publishing, 2013; ISBN 9780857094209.

58. Carpenter Additive Methods of AM Powder production Available online: https://www.carpenteradditive.com/technical-library/powder-production/.

59. Sun, P.; Fang, Z.Z.; Zhang, Y.; Xia, Y. Review of the Methods for Production of Spherical Ti and Ti Alloy Powder. *Jom* **2017**, *69*, 1853–1860, doi:10.1007/s11837-017-2513-5.

60. Entezarian, M.; Allaire, F.; Tsantrizos, P.; Drew, R.A.L. Plasma atomization: A new process for the production of fine, spherical powders. *Jom* **1996**, *48*, 53–55, doi:10.1007/BF03222969.

61. Slotwinski, J.A.; Garboczi, E.J.; Stutzman, P.E.; Ferraris, C.F.; Watson, S.S.; Peltz, M.A. Characterization of Metal Powders Used for Additive Manufacturing. *J. Res. Natl. Inst. Stand.*

Technol. **2014**, *119*, 460, doi:10.6028/jres.119.018.

62. Vock, S.; Klöden, B.; Kirchner, A.; Weißgärber, T.; Kieback, B. Powders for powder bed fusion: a review. *Prog. Addit. Manuf.* **2019**, *0*, 0, doi:10.1007/s40964-019-00078-6.

63. F3049 − 14, A. Standard Guide for Characterizing Properties of Metal Powders Used for Additive Manufacturing Processes. *F3049 - 14* **2014**, 1–3, doi:10.1520/F3049-14.

64. Anton Paar The influence of particles on suspension rheology Available online: https://wiki.anton-paar.com/it-it/linfluenza-delle-particelle-sulla-reologia-della-sospensione/.

65. Horiba Scientific Understanding and Interpreting Particle Size Distribution Calculations Available online: https://www.horiba.com/uk/scientific/products/particle-characterization/education/general-information/data-interpretation/understanding-particle-size-distribution-calculations/.

66. Koseski, R.P.; Suri, P.; Earhardt, N.B.; German, R.M.; Kwon, Y.-S. Microstructural evolution of injection molded gas- and water-atomized 316L stainless steel powder during sintering. *Mater. Sci. Eng. A* **2005**, *390*, 171–177, doi:10.1016/j.msea.2004.08.002.

67. freemantechnology Powder Rheology Available online: https://www.freemantech.co.uk/learn/powder-rheology.

68. Hebert, R.J. Viewpoint: metallurgical aspects of powder bed metal additive manufacturing. *J. Mater. Sci.* **2016**, *51*, 1165–1175, doi:10.1007/s10853-015-9479-x.

69. ASTM INTERNATIONAL Standard Test Methods for Flow Rate of Metal Powders Using the Hall Flowmeter Funnel. *ASTM Int.* **2014**, *i*, 213–216, doi:10.1520/B0213-13.2.

70. ASTM INTERNATIONAL Standard Test Methods for Flow Rate of Metal Powders Using the Carney Funnel. *ASTM Stand.* **2016**, 4–6, doi:10.1520/B0964-16.2.

71. Optical Penetration Depth of Laser beams in Powder Bed Available online: https://www.insidemetaladditivemanufacturing.com/blog/optical-penetration-depth-of-laser-beams-in-powder-bed#.

72. Zeng, K.; Pal, D.; Stucker, B. A review of thermal analysis methods in laser sintering and selective laser melting. *23rd Annu. Int. Solid Free. Fabr. Symp. - An Addit. Manuf. Conf. SFF 2012* **2012**, 796–814.

73. Spears, T.G.; Gold, S.A. In-process sensing in selective laser melting (SLM) additive manufacturing. *Integr. Mater. Manuf. Innov.* **2016**, *5*, 16–40, doi:10.1186/s40192-016-0045-4.

74. Clijsters, S.; Craeghs, T.; Buls, S.; Kempen, K.; Kruth, J.-P. In situ quality control of the selective laser melting process using a high-speed, real-time melt pool monitoring system. *Int. J. Adv. Manuf. Technol.* **2014**, *75*, 1089–1101, doi:10.1007/s00170-014-6214-8.

75. Yin, J.; Zhu, H.; Ke, L.; Hu, P.; He, C.; Zhang, H.; Zeng, X. A finite element model of thermal evolution in laser micro sintering. *Int. J. Adv. Manuf. Technol.* **2016**, *83*, 1847–1859, doi:10.1007/s00170-015-7609-x.

76. Yin, J.; Yang, L.L.; Yang, X.; Zhu, H.; Wang, D.; Ke, L.; Wang, Z.; Wang, G.; Zeng, X. High-power laser-matter interaction during laser powder bed fusion. *Addit. Manuf.* **2019**, *29*, 100778, doi:10.1016/j.addma.2019.100778.

77. Cook, P.S.; Murphy, A.B. Simulation of melt pool behaviour during additive manufacturing: Underlying physics and progress. *Addit. Manuf.* **2020**, *31*, 100909, doi:10.1016/j.addma.2019.100909.

78. Foroozmehr, A.; Badrossamay, M.; Foroozmehr, E.; Golabi, S. Finite Element Simulation of Selective Laser Melting process considering Optical Penetration Depth of laser in powder bed. *Mater. Des.* **2016**, *89*, 255–263, doi:10.1016/j.matdes.2015.10.002.

79. Gong, H.; Rafi, K.; Starr, T.; Stucker, B. The effects of processing parameters on defect regularity in Ti-6Al-4V parts fabricated by Selective Laser Melting and Electron Beam Melting. *24th Int. SFF Symp. - An Addit. Manuf. Conf. SFF 2013* **2013**, 424–439.

80. Aboulkhair, N.T.; Everitt, N.M.; Ashcroft, I.; Tuck, C. Reducing porosity in AlSi10Mg parts processed by selective laser melting. *Addit. Manuf.* **2014**, *1*, 77–86, doi:10.1016/j.addma.2014.08.001.

81. Tang, M.; Pistorius, P.C.; Beuth, J.L. Prediction of lack-of-fusion porosity for powder bed fusion. *Addit. Manuf.* **2017**, *14*, 39–48, doi:10.1016/j.addma.2016.12.001.

82. Gusarov, A. V.; Smurov, I. Modeling the interaction of laser radiation with powder bed at selective laser melting. *Phys. Procedia* **2010**, *5*, 381–394, doi:10.1016/j.phpro.2010.08.065.

83. Materialise *SLM Build Processor*; 2016;

84. Ali, H.; Ghadbeigi, H.; Mumtaz, K. Effect of scanning strategies on residual stress and mechanical properties of Selective Laser Melted Ti6Al4V. *Mater. Sci. Eng. A* **2018**, *712*, 175–187, doi:10.1016/j.msea.2017.11.103.

85. Zhang, B.; Li, Y.; Bai, Q. Defect Formation Mechanisms in Selective Laser Melting: A Review. *Chinese J. Mech. Eng. (English Ed.* **2017**, *30*, 515–527, doi:10.1007/s10033-017-0121-5.

86. Kempen, K.; Thijs, L.; Humbeeck, J. Van; Kruth, J.P. Processing AlSi10Mg by selective laser melting: Parameter optimisation and material characterisation. *Mater. Sci. Technol. (United Kingdom)* **2015**, *31*, 917–923, doi:10.1179/1743284714Y.0000000702.

87. Read, N.; Wang, W.; Essa, K.; Attallah, M.M. Selective laser melting of AlSi10Mg alloy: Process optimisation and mechanical properties development. *Mater. Des.* **2015**, *65*, 417–424, doi:10.1016/j.matdes.2014.09.044.

88. Gu, D.; Hagedorn, Y.-C.; Meiners, W.; Meng, G.; Batista, R.J.S.; Wissenbach, K.; Poprawe, R. Densification behavior, microstructure evolution, and wear performance of selective laser melting processed commercially pure titanium. *Acta Mater.* **2012**, *60*, 3849–3860, doi:10.1016/j.actamat.2012.04.006.

89. Bhavar, V.; Kattire, P.; Patil, V.; Khot, S.; Gujar, K.; Singh, R. A review on powder bed fusion technology of metal additive manufacturing. In *Additive Manufacturing Handbook*; CRC Press, 2017; pp. 251–253.

90. Boschetto, A.; Bottini, L.; Veniali, F. Roughness modeling of AlSi10Mg parts fabricated by selective laser melting. *J. Mater. Process. Technol.* **2017**, *241*, 154–163, doi:10.1016/j.jmatprotec.2016.11.013.

91. Bassoli, E.; Denti, L.; Comin, A.; Sola, A.; Tognoli, E. Fatigue Behavior of As-Built L-PBF A357.0 Parts. *Metals (Basel).* **2018**, *8*, 634, doi:10.3390/met8080634.

92. Denti, L.; Sola, A. On the effectiveness of different surface finishing techniques on A357.0 parts produced by laser-based powder bed fusion: Surface roughness and fatigue strength. *Metals (Basel).* **2019**, *9*, doi:10.3390/met9121284.

93. Kulekci, M.K.; Esme, U. Critical analysis of processes and apparatus for industrial surface peening technologies. *Int. J. Adv. Manuf. Technol.* **2014**, *74*, 1551–1565, doi:10.1007/s00170-014-6088-9.

94. Knowles, C.R.; Becker, T.H.; Tait, R.B. The effect of heat treatment on the residual stress levels within direct metal laser sintered ti-6al-4v as measured using the hole-drilling strain gauge method.

Not Yet Publ. **2012**, 1–10.

95. Blinn, B.; Krebs, F.; Ley, M.; Teutsch, R.; Beck, T. Determination of the influence of a stress-relief heat treatment and additively manufactured surface on the fatigue behavior of selectively laser melted AISI 316L by using efficient short-time procedures. *Int. J. Fatigue* **2020**, *131*, 105301, doi:10.1016/j.ijfatigue.2019.105301.

96. Milewski, J.O. *Springer Series in Materials Science 258 Additive Manufacturing of Metals*; 2017; ISBN 9783319582047.

97. Wikipedia Casting (Metal working) Available online: https://en.wikipedia.org/wiki/Casting_(metalworking).

98. Todai, M.; Nakano, T.; Liu, T.; Yasuda, H.Y.; Hagihara, K.; Cho, K.; Ueda, M.; Takeyama, M. Effect of building direction on the microstructure and tensile properties of Ti-48Al-2Cr-2Nb alloy additively manufactured by electron beam melting. *Addit. Manuf.* **2017**, *13*, 61–70, doi:10.1016/j.addma.2016.11.001.

99. Solutions, S. *SLM Solutions AlSi7Mg0,6 Datasheet*;

100. Roy, M.J.; Maijer, D.M.; Dancoine, L. Constitutive behavior of as-cast A356. *Mater. Sci. Eng. A* **2012**, *548*, 195–205, doi:10.1016/j.msea.2012.03.106.

101. Yang, K. V.; Rometsch, P.; Davies, C.H.J.; Huang, A.; Wu, X. Effect of heat treatment on the microstructure and anisotropy in mechanical properties of A357 alloy produced by selective laser melting. *Mater. Des.* **2018**, *154*, 275–290, doi:10.1016/j.matdes.2018.05.026.

102. Fine, M.E. Precipitation hardening of aluminum alloys. *Metall. Trans. A* **1975**, *6*, 625–630, doi:10.1007/BF02672283.

103. Jaramillo, R.R.A. and D. Mechanical Behavior of Precipitation Hardened Aluminum Alloys Welds. **2014**, *Light Meta*, doi:10.5772/58418.

104. Vlach, M.; Čížek, J.; Smola, B.; Melikhova, O.; Vlček, M.; Kodetová, V.; Kudrnová, H.; Hruška, P. Heat treatment and age hardening of Al–Si–Mg–Mn commercial alloy with addition of Sc and Zr. *Mater. Charact.* **2017**, *129*, 1–8, doi:10.1016/j.matchar.2017.04.017.

105. van Huis, M.A.; Chen, J.H.; Sluiter, M.H.F.; Zandbergen, H.W. Phase stability and structural features of matrix-embedded hardening precipitates in Al–Mg–Si alloys in the early stages of evolution. *Acta Mater.* **2007**, *55*, 2183–2199, doi:10.1016/j.actamat.2006.11.019.

106. Casati, R.; Masa, V.G. La; Hamidi, M.; Politecnico, N.; Masa, V.G. La Effect of Different Heat Treatment Routes on Microstructure and Mechanical Properties of AlSi7Mg , AlSi10Mg and Al-Mg-Zr-Sc Alloys Produced by Selective Laser Melting © European Powder Metallurgy Association (EPMA) © European Powder Metallurgy Associati. *Euro PM2018* **2018**, *3*.

107. Denti, L. Additive Manufactured A357.0 Samples Using the Laser Powder Bed Fusion Technique: Shear and Tensile Performance. *Metals (Basel).* **2018**, *8*, 670, doi:10.3390/met8090670.

108. Casati, R.; Vedani, M. Aging Response of an A357 Al Alloy Processed by Selective Laser Melting. *Adv. Eng. Mater.* **2019**, *21*, 1–7, doi:10.1002/adem.201800406.

109. Gatto, A.; Bassoli, E.; Denti, L.; Sola, A.; Tognoli, E.; Comin, A.; Porro, J.A.; Cordovilla, F.; Angulo, I.; Ocaña, J.L. Effect of Three Different Finishing Processes on the Surface Morphology and Fatigue Life of A357.0 Parts Produced by Laser-Based Powder Bed Fusion. *Adv. Eng. Mater.* **2019**, *21*, 1–10, doi:10.1002/adem.201801357.

110. Brandl, E.; Heckenberger, U.; Holzinger, V.; Buchbinder, D. Additive manufactured AlSi10Mg samples using Selective Laser Melting (SLM): Microstructure, high cycle fatigue, and fracture behavior.

Mater. Des. **2012**, *34*, 159–169, doi:10.1016/j.matdes.2011.07.067.

111. Lütjering, G.; Williams, J.C. *Titanium*; Engineering Materials, Processes; Springer Berlin Heidelberg: Berlin, Heidelberg, 2007; ISBN 978-3-540-71397-5.

112. Liu, S.; Shin, Y.C. Additive manufacturing of Ti6Al4V alloy: A review. *Mater. Des.* **2019**, *164*, 107552, doi:10.1016/j.matdes.2018.107552.

113. EOS GmbH Ti-6Al-4V powder - technical data sheet. **2011**, *49*, 5.

114. Reda, R.; Nofal, A.; Hussein, A.H. Effect of Single and Duplex Stage Heat Treatment on the Microstructure and Mechanical Properties of Cast Ti-6Al-4V Alloy. *Metallogr. Microstruct. Anal.* **2013**, *2*, 388–393, doi:10.1007/s13632-013-0103-7.

115. Boyer, H.E. Heat Treating of Nonferrous Alloys. *Metallogr. Microstruct. Anal.* **2013**, *2*, 190–195, doi:10.1007/s13632-013-0074-8.

116. Morri, A. Trattamenti termici delle leghe di titanio α+β, correlazioni fra microstruttura e comportamento meccanico. *Metall. Ital.* **2008**, *100*, 1–10.

117. Cottam, R.; Palanisamy, S.; Avdeev, M.; Jarvis, T.; Henry, C.; Cuiuri, D.; Balogh, L.; Abdul Rahman Rashid, R. Diffraction Line Profile Analysis of 3D Wedge Samples of Ti-6Al-4V Fabricated Using Four Different Additive Manufacturing Processes. *Metals (Basel).* **2019**, *9*, 60, doi:10.3390/met9010060.

118. Vrancken, B.; Thijs, L.; Kruth, J.P.; Van Humbeeck, J. Heat treatment of Ti6Al4V produced by Selective Laser Melting: Microstructure and mechanical properties. *J. Alloys Compd.* **2012**, *541*, 177–185, doi:10.1016/j.jallcom.2012.07.022.

119. Ahmed, T.; Rack, H.J. Phase transformations during cooling in alpha+beta titanium alloys. *Mater. Sci. Eng. A* **2002**, *243*, 206–211, doi:10.1016/s0921-5093(97)00802-2.

120. Liang, Z.; Sun, Z.; Zhang, W.; Wu, S.; Chang, H. The effect of heat treatment on microstructure evolution and tensile properties of selective laser melted Ti6Al4V alloy. *J. Alloys Compd.* **2019**, *782*, 1041–1048, doi:10.1016/j.jallcom.2018.12.051.

121. Mower, T.M.; Long, M.J. Mechanical behavior of additive manufactured, powder-bed laser-fused materials. *Mater. Sci. Eng. A* **2016**, *651*, 198–213, doi:10.1016/j.msea.2015.10.068.

122. Rafi, H.K.; Karthik, N. V.; Gong, H.; Starr, T.L.; Stucker, B.E. Microstructures and Mechanical Properties of Ti6Al4V Parts Fabricated by Selective Laser Melting and Electron Beam Melting. *J. Mater. Eng. Perform.* **2013**, *22*, 3872–3883, doi:10.1007/s11665-013-0658-0.

123. Wysocki, B.; Maj, P.; Sitek, R.; Buhagiar, J.; Kurzydłowski, K.; Święszkowski, W. Laser and Electron Beam Additive Manufacturing Methods of Fabricating Titanium Bone Implants. *Appl. Sci.* **2017**, *7*, 657, doi:10.3390/app7070657.

124. Simonelli, M.; Tse, Y.Y.; Tuck, C. Effect of the build orientation on the mechanical properties and fracture modes of SLM Ti–6Al–4V. *Mater. Sci. Eng. A* **2014**, *616*, 1–11, doi:10.1016/j.msea.2014.07.086.

125. Vilaro, T.; Colin, C.; Bartout, J.D. As-Fabricated and Heat-Treated Microstructures of the Ti-6Al-4V Alloy Processed by Selective Laser Melting. *Metall. Mater. Trans. A* **2011**, *42*, 3190–3199, doi:10.1007/s11661-011-0731-y.

126. Wycisk, E.; Solbach, A.; Siddique, S.; Herzog, D.; Walther, F.; Emmelmann, C. Effects of Defects in Laser Additive Manufactured Ti-6Al-4V on Fatigue Properties. *Phys. Procedia* **2014**, *56*, 371–378, doi:10.1016/j.phpro.2014.08.120.

127. Kasperovich, G.; Hausmann, J. Improvement of fatigue resistance and ductility of TiAl6V4 processed

by selective laser melting. *J. Mater. Process. Technol.* **2015**, *220*, 202–214, doi:10.1016/j.jmatprotec.2015.01.025.

128. Vayssette, B.; Saintier, N.; Brugger, C.; Elmay, M.; Pessard, E. Surface roughness of Ti-6Al-4V parts obtained by SLM and EBM: Effect on the High Cycle Fatigue life. *Procedia Eng.* **2018**, *213*, 89–97, doi:10.1016/j.proeng.2018.02.010.

129. Bagehorn, S.; Wehr, J.; Maier, H.J. Application of mechanical surface finishing processes for roughness reduction and fatigue improvement of additively manufactured Ti-6Al-4V parts. *Int. J. Fatigue* **2017**, *102*, 135–142, doi:10.1016/j.ijfatigue.2017.05.008.

130. Leuders, S.; Thöne, M.; Riemer, A.; Niendorf, T.; Tröster, T.; Richard, H.A.; Maier, H.J. On the mechanical behaviour of titanium alloy TiAl6V4 manufactured by selective laser melting: Fatigue resistance and crack growth performance. *Int. J. Fatigue* **2013**, *48*, 300–307, doi:10.1016/j.ijfatigue.2012.11.011.

131. Steels for aircraft structures. In *Introduction to Aerospace Materials*; Elsevier, 2012; pp. 232–250.

132. Kempen, K.; Yasa, E.; Thijs, L.; Kruth, J.P.; Van Humbeeck, J. Microstructure and mechanical properties of selective laser melted 18Ni-300 steel. *Phys. Procedia* **2011**, *12*, 255–263, doi:10.1016/j.phpro.2011.03.033.

133. Robert-Stirling-Ring Material Data Sheet (EOS) - EOS MaragingSteel MS1. **2014**, *49*, 1–5.

134. Yin, S.; Chen, C.; Yan, X.; Feng, X.; Jenkins, R.; O'Reilly, P.; Liu, M.; Li, H.; Lupoi, R. The influence of aging temperature and aging time on the mechanical and tribological properties of selective laser melted maraging 18Ni-300 steel. *Addit. Manuf.* **2018**, *22*, 592–600, doi:10.1016/j.addma.2018.06.005.

135. Bai, Y.; Yang, Y.; Wang, D.; Zhang, M. Influence mechanism of parameters process and mechanical properties evolution mechanism of maraging steel 300 by selective laser melting. *Mater. Sci. Eng. A* **2017**, *703*, 116–123, doi:10.1016/j.msea.2017.06.033.

136. Tan, C.; Zhou, K.; Kuang, M.; Ma, W.; Kuang, T. Microstructural characterization and properties of selective laser melted maraging steel with different build directions. *Sci. Technol. Adv. Mater.* **2018**, *19*, 746–758, doi:10.1080/14686996.2018.1527645.

137. Casati, R.; Lemke, J.; Tuissi, A.; Vedani, M. Aging Behaviour and Mechanical Performance of 18-Ni 300 Steel Processed by Selective Laser Melting. *Metals (Basel).* **2016**, *6*, 218, doi:10.3390/met6090218.

138. Meneghetti, G.; Rigon, D.; Cozzi, D.; Waldhauser, W.; Dabalà, M. Influence of build orientation on static and axial fatigue properties of maraging steel specimens produced by additive manufacturing. *Procedia Struct. Integr.* **2017**, *7*, 149–157, doi:10.1016/j.prostr.2017.11.072.

139. Damon, J.; Hanemann, T.; Dietrich, S.; Graf, G.; Lang, K.-H.; Schulze, V. Orientation Dependent Fatigue Performance and Mechanisms of Selective Laser Melted Maraging Steel X3NiCoMoTi18-9-5. *Int. J. Fatigue* **2019**, *127*, 395–402, doi:10.1016/j.ijfatigue.2019.06.025.

140. Croccolo, D.; De Agostinis, M.; Fini, S.; Olmi, G.; Vranic, A.; Ciric-Kostic, S. Influence of the build orientation on the fatigue strength of EOS maraging steel produced by additive metal machine. *Fatigue Fract. Eng. Mater. Struct.* **2016**, *39*, 637–647, doi:10.1111/ffe.12395.

141. Everhart, W.; Sawyer, E.; Neidt, T.; Dinardo, J.; Brown, B. The effect of surface finish on tensile behavior of additively manufactured tensile bars. *J. Mater. Sci.* **2016**, *51*, 3836–3845, doi:10.1007/s10853-015-9702-9.

142. Addaero *Effect of Roughness on Tensile Properties*; 2017;

143. Schijve, J.; Yarema, S.Y. Fatigue of structures and materials in the 20th century and the state of the art. *Mater. Sci.* **2003**, *39*, 307–333, doi:10.1023/B:MASC.0000010738.91907.a9.

144. Nezhadfar, P.D.; Shrestha, R.; Phan, N.; Shamsaei, N. Fatigue behavior of additively manufactured 17-4 PH stainless steel: Synergistic effects of surface roughness and heat treatment. *Int. J. Fatigue* **2019**, *124*, 188–204, doi:10.1016/j.ijfatigue.2019.02.039.

145. Denti, L.; Bassoli, E.; Gatto, A.; Santecchia, E.; Mengucci, P. Fatigue life and microstructure of additive manufactured Ti6Al4V after different finishing processes. *Mater. Sci. Eng. A* **2019**, *755*, 1–9, doi:10.1016/j.msea.2019.03.119.

146. Wycisk, E.; Emmelmann, C.; Siddique, S.; Walther, F. High Cycle Fatigue (HCF) Performance of Ti-6Al-4V Alloy Processed by Selective Laser Melting. *Adv. Mater. Res.* **2013**, *816–817*, 134–139, doi:10.4028/www.scientific.net/amr.816-817.134.

147. Uzan, N.E.; Ramati, S.; Shneck, R.; Frage, N.; Yeheskel, O. On the effect of shot-peening on fatigue resistance of AlSi10Mg specimens fabricated by additive manufacturing using selective laser melting (AM-SLM). *Addit. Manuf.* **2018**, *21*, 458–464, doi:10.1016/j.addma.2018.03.030.

148. Hackel, L.; Fuhr, J.; Sharma, M.; Rankin, J.; Sherman, V.; Davami, K. Test Results for Wrought and AM In718 Treated by Shot Peening and Laser Peening Plus Thermal Microstructure Engineering. *Procedia Struct. Integr.* **2019**, *19*, 452–462, doi:10.1016/j.prostr.2019.12.049.

149. Denti, L.; Bassoli, E.; Gatto, A.; Santecchia, E.; Mengucci, P. Fatigue life and microstructure of additive manufactured Ti6Al4V after different finishing processes. *Mater. Sci. Eng. A* **2019**, *755*, 1–9, doi:10.1016/j.msea.2019.03.119.

150. Wang, M.; Song, B.; Wei, Q.; Zhang, Y.; Shi, Y. Effects of annealing on the microstructure and mechanical properties of selective laser melted AlSi7Mg alloy. *Mater. Sci. Eng. A* **2019**, *739*, 463–472, doi:10.1016/j.msea.2018.10.047.

151. T.H. Becker, M.B.& C.S. MICROSTRUCTURE AND MECHANICAL PROPERTIES OF DIRECT METAL LASER SINTERED TI- 6AL-4V. **2015**, *3*, 54–67.

152. Qiu, C.; Adkins, N.J.E.; Attallah, M.M. Microstructure and tensile properties of selectively laser-melted and of HIPed laser-melted Ti-6Al-4V. *Mater. Sci. Eng. A* **2013**, *578*, 230–239, doi:10.1016/j.msea.2013.04.099.

153. Brandl, E.; Heckenberger, U.; Holzinger, V.; Buchbinder, D. Additive manufactured AlSi10Mg samples using Selective Laser Melting (SLM): Microstructure, high cycle fatigue, and fracture behavior. *Mater. Des.* **2012**, *34*, 159–169, doi:10.1016/j.matdes.2011.07.067.

154. Aversa, A.; Lorusso, M.; Trevisan, F.; Ambrosio, E.; Calignano, F.; Manfredi, D.; Biamino, S.; Fino, P.; Lombardi, M.; Pavese, M. Effect of Process and Post-Process Conditions on the Mechanical Properties of an A357 Alloy Produced via Laser Powder Bed Fusion. *Metals (Basel).* **2017**, *7*, 68, doi:10.3390/met7020068.

155. EOS GmbH EOS M400 Specifications Available online: https://www.eos.info/systems_solutions/metal/systems_equipment/eos_m_400.

156. Bourne, R.B.; Oh, I.; Harris, W.H. Femoral cement pressurization during total hip arthroplasty. The role of different femoral stems with reference to stem size and shape. **1984**.

157. International Organization for Standardization ISO 7206-4:2010(E) - Determination of endurance properties and performance of stemmed femoral components. **2010**.

158. International Organization for Standardization ISO 7206-6:2013(E) - Endurance properties testing and performance requirements of neck region of stemmed femoral components. **2013**.

159. EOS GmbH EOS M290 specifications Available online: https://www.eos.info/eos-m290.

160. ISO Metallic materials - Tensile testing - Part 1: Method of test at room temperature (ISO 6892-1:2009) Matériaux 2009.

161. Fatigue Available online: https://en.wikipedia.org/wiki/Fatigue_(material).

162. Comsol Multiphysics Material Fatigue Available online: https://www.comsol.com/multiphysics/material-fatigue.

163. ISO Metallic materials — Fatigue testing — Statistical planning and analysis of data - ISO 12107 2006, *2006*, 13.

164. European Committee for Standardization *UNI EN 3987:2009 (E) - Constant amplitude force-controlled high cycle fatigue testing*; 2009;

165. Dixon, W.J.; Mood, A.M. A Method for Obtaining and Analyzing Sensitivity Data. *J. Am. Stat. Assoc.* **1948**, *43*, 109, doi:10.2307/2280071.

166. Ransom, J.T.; Mehl, R.F. The Statistical Nature of the Endurance Limit. **1950**.

167. Nicholas, T. *High Cycle Fatigue*; Elsevier, 2006; ISBN 9780080446912.

168. Lieberman, G.J. Tables for one-sided statistical tolerance limits. **1957**.

169. Resnikoff, G.J.; Lieberman, G.J. *Tables of the non-central t-distribution*; 1957;

170. Johnson, N.L.; Owen, D.B. Factors for One-Sided Tolerance Limits and for Variables Sampling Plans. *Biometrika* 1964, *51*, 293.

171. Link, C.L. An Equation for One-Sided Tolerance Limits for Normal Distributions. Res. Pap. FPL 458. *Statistician* **1985**, 1–4.

172. Lumen Physics Archimedes’ Principle Available online: https://courses.lumenlearning.com/physics/chapter/11-7-archimedes-principle/.

173. Maidment, D.R. *Handbook of Hydrology*; 1993;

174. Baird, C.S. Why does ice form on the top of a lake? Available online: https://wtamu.edu/~cbaird/sq/2013/12/05/why-does-ice-form-on-the-top-of-a-lake/.

175. International Organization for Standardization ISO 4287:1997/Amd.1:2009(E) - Surface texture: Profile method - Terms, definitions and surface texture parameters 2009.

176. Pike-Wilson, E.A.; Karayiannis, T.G. Flow boiling of R245fa in 1.1 mm diameter stainless steel, brass and copper tubes. *Exp. Therm. Fluid Sci.* **2014**, *59*, 166–183, doi:10.1016/j.expthermflusci.2014.02.024.

177. Gadelmawla, E.S.; Koura, M.M.; Maksoud, T.M.A.; Elewa, I.M.; Soliman, H.H. Roughness parameters. *J. Mater. Process. Technol.* **2002**, *123*, 133–145, doi:10.1016/S0924-0136(02)00060-2.

178. International Organization for Standardization ISO 25178-2:2012 - Terms, definitions and surface texture parameters 2012.

179. Digital Surf Areal Field Parameters Available online: https://guide.digitalsurf.com/en/guide-areal-field-parameters.html.

180. Confocal Microscopy Available online: https://en.wikipedia.org/wiki/Confocal_microscopy.

181. Rao, H.; Giet, S.; Yang, K.; Wu, X.; Davies, C.H.J. The influence of processing parameters on aluminium alloy A357 manufactured by Selective Laser Melting. *Mater. Des.* **2016**, *109*, 334–346,

doi:10.1016/j.matdes.2016.07.009.

182. EOS AlSi10Mg Datasheet. **2014**, *49*, 1–5.

183. Aboulkhair, N.T.; Maskery, I.; Tuck, C.; Ashcroft, I.; Everitt, N.M. Improving the fatigue behaviour of a selectively laser melted aluminium alloy: Influence of heat treatment and surface quality. *Mater. Des.* **2016**, *104*, 174–182, doi:10.1016/j.matdes.2016.05.041.

184. Spierings, A.B.; Schneider, M.; Eggenberger, R. Comparison of density measurement techniques for additive manufactured metallic parts. *Rapid Prototyp. J.* **2011**, *17*, 380–386, doi:10.1108/13552541111156504.

185. Rao, J.H.; Rometsch, P.; Wu, X.; Davies, C.H.J. The processing and heat treatment of selective laser melted Al-7Si-0.6Mg alloy. In *Additive Manufacturing for the Aerospace Industry*; Elsevier, 2019; pp. 143–161.

186. Maschietto Mario Eredi s.r.l. Verniciatura a polvere Available online: https://www.maschietto.it/verniciatura-a-polvere.

187. Todd, G. Stress concentrations at holes Available online: https://www.fracturemechanics.org/hole.html.

List of images

List of tables